Large-scale Biomass-fired Power Plant integrated with solvent-based Post-combustion Carbon Capture: Simulation, Techno-economic Analysis, Optimisation and Life cycle Assessment

By:
Jiayi Ren
Supervisor: Prof. Meihong Wang

A thesis submitted in partial fulfilment of the requirements for the degree of Doctor of Philosophy

School of Chemical, Materials and Biological Engineering
Faculty of Engineering
The University of Sheffield

February 2025

Acknowledgement

Firstly, I would like to thank the University of Sheffield for providing an excellent research environment and facilities that made my work possible. The support and resources offered by the university were necessary to complete this thesis successfully.

I am profoundly grateful to my supervisor, Professor Meihong Wang, for his constructive guidance, insightful advice and support throughout my PhD journey. Prof. Wang's critical feedback continually pushed me to improve the quality of this work continuously. I also wish to express my great thankfulness to Dr. Olajide Otitoju, our postdoctoral fellow, for his extensive knowledge and dedicated support. His help in proposing critical questions, answering my questions and providing practical advice was vital in facing challenges during my research. Additionally, I would like to thank Prof. Gao and Prof. Liang from the University of Hunan for their help and advice on my first paper.

I am also thankful to the EU RISE project OPTIMAL (Grant Agreement No: 101007963) for supporting my six-month study at Hunan University. This experience was valuable and contributed significantly to my research.

Many thanks to my friends, roommates, the members of the D10 office and the Process and Energy System Engineering Research Group for their encouragement and support throughout this journey.

Finally, I would like to thank my family, especially my parents, for their massive support, encouragement, and belief in me. A special thanks to my mother for her emotional support every time I was frustrated, which encouraged me to complete this journey.

Abstract

Bioenergy with carbon capture and storage (BECCS) is a key negative emission technology (NET) for reducing atmospheric CO_2 levels. Solvent-based post-combustion carbon capture (PCC) is the widely used method of capturing CO_2 emissions from power plants, but its high energy and cost demands limit commercial application.

This PhD study aims to investigate a cost-effective, energy-efficient and environmentally sustainable supercritical biomass-fired power plant (BFPP) integrated with a solvent-based PCC process. The models of the large-scale BFPP and the pilot-scale PCC process using monoethanolamine (MEA) and piperazine (PZ) solvents were developed and validated in Aspen Plus® V11. The validated pilot-scale models of both the MEA-based and PZ-based PCC processes were scaled up to process flue gas from a 550 MWe BFPP. Different configurations of the solvent-based PCC process were simulated, including the standard PCC, PCC with absorber intercooling (AIC) and advanced flash stripper (AFS), additionally, the combination of AIC and AFS with side stream extraction (SSE). Furthermore, a model for CO_2 compression utilising a heat pump (HP) and a supercritical CO_2 cycle (sCO_2) was developed.

The energy analysis revealed that the PCC process, which uses 40wt% PZ and process configuration consisting of AIC-AFS-SSE-sCO_2, achieved the lowest energy consumption of 2.78 GJ/t_{CO2}. This configuration reduced the specific heat duty by 1.01 GJ/t_{CO2} compared to the standard PCC process using 30wt% MEA which serves as the benchmark in this study. The economic performance of the various PCC processes was evaluated using the Aspen Process Economic Analyzer® (APEA). The results indicated that the AIC-AFS-SSE-sCO_2 configuration with 40wt% PZ as solvent achieved the lowest CO_2 capture costs (CCC) of 57.5\$/t_{CO2}. This represents a 17% cost reduction compared to the standard 40wt% PZ process, which has a cost of 69.2 \$/t_{CO2}.

Furthermore, the optimisation of the PZ-based PCC process was conducted to determine the solvent concentration and stripper pressure that would minimise the CCC. The recommended PZ concentrations were found to be 37.5wt% for the standard configuration and 32.5wt%, for the AIC-AFS configuration. Additionally, a stripper pressure of 7 bar was recommended for AIC-AFS configuration, which

demonstrated a reduction in specific heat duty and CCC by 41.6% and 32.4% respectively, compared to the standard PCC process (with 40wt% PZ) without optimisation.

The exergy analysis of three cases was carried out, including Case 1: 550 MWe BFPP integrated with standard PCC process using 30wt% MEA, Case 2: 550 MWe BFPP integrated with standard PCC process using 40wt% PZ, and Case 3: 550 MWe BFPP integrated with optimised PCC process using AIC-AFS configuration and 32.5wt% PZ. The results showed that Case 3 can decrease the exergy destruction of the PCC subsystem by 71.8 MW corresponding to a 37.8% reduction, performing the best thermodynamic performance. Furthermore, the Life Cycle Assessment (LCA) of the three integration cases were conducted. On a basis of generating 1MWh net electricity, Case 1 with standard PCC process using 30wt% MEA achieved the highest CO_2 sequestration of -1724 kg_{CO2}/MWh and net-negative emissions of -1330 kg_{CO2}/MWh, although it has the highest energy demand for carbon capture. This is because it has the lowest power output and thus has the highest CO_2 sequestration per unit of electricity generated. On the basis of consuming one-tonne biomass, Case 3 with the optimised PCC process achieved the highest net-negative CO_2 emissions of -1493 kg_{CO2}/t, the lowest biomass requirement of 0.72 t/MWh, and the minimum supply chain emissions of 458 kg_{CO2}/t. The results indicate that using BFPP integrated with the optimised PCC showed the highest net-negative CO_2 emissions both per MWh of net electricity generated and per tonne of biomass consumed.

Keywords: *Post-combustion carbon capture, Chemical absorption, Bioenergy with carbon capture and storage, Process simulation, Techno-economic analysis, Optimisation, Exergy analysis, Life cycle assessment.*

List of peer-reviewed publications and presentations

Peer-reviewed journal:

Sections 3.3, 3.4 and Chapter 4 of this thesis have been published as follows:

Ren, J., Otitoju, O., Gao, H., Liang, Z. and Wang, M. (2025) 'Techno-economic analysis and optimisation of Piperazine-based post-combustion carbon capture and CO_2 compression process for large-scale biomass-fired power plants through simulation', *Fuel*, 381, 133340.

Section 3.2, Chapters 5 and 6 of this thesis are being prepared for the following publication:

Ren, J., Otitoju, O. and Wang, M. (2025) 'Energy, exergy and life cycle assessment of biomass-fired supercritical power plant integrated with Piperazine-based post-combustion carbon capture through simulation', *Fuel*, under preparation.

Conference presentation:

Ren, J., Otitoju, O., Gao, H., Liang, Z. and Wang, M. (2023). Techno-economic analysis and optimisation of Piperazine-based post-combustion carbon capture and CO_2 compression process for large-scale biomass-fired power plants through simulation. 2nd European Conference on Fuel and Energy Research and its Applications (FERIA), Sheffield UK. 4th to 6th September 2023.

Table of Contents

List of Figures

List of Tables

Nomenclatures

Symbol	Quantity	Unit
a_i	Stoichiometric of species i	-
C_i	Concentration of species i	mol/L
$c_{p,cw}$	Heat capacity of the cooling water	J/kg·K
E	Activation energy	cal/mol
$\dot{E}x_{Chem}$	Chemical exergy	MW
$\dot{E}x_{D,n}$	Exergy destruction for component n	MW
$\dot{E}x_i$	Exergy flow rate of species i	MW
$\dot{E}x_{in,n}$	Exergy rate of the inlet flow for component n	MW
$\dot{E}x_{out,n}$	Exergy rate of the outlet flow for component n	MW
$\dot{E}x_{Phy}$	Physical exergy	MW
$\dot{E}x_{Q,n}$	Exergy rate for heating or cooling	MW
$\dot{E}x_{W,n}$	Exergy rate for work	MW
G^*_W	Gas mass flow rate per unit cross-sectional area	kg/s·m^2
ex_{Chem}	Specific chemical exergy	J/kg
ex_i	Specific exergy of species i	J/kg
ex_{Phy}	Specific physical exergy	J/kg
$F_{CO_2,OUT}$	Annual CO_2 production rate	t/h
F_{LV}	Flow parameter	-
F_P	Packing factor of the packed column	m^{-1}
$G_{\dot{W}}$	Flue gas mass flow rate	kg/s
h_0	Enthalpy at the reference state	J/kg
I	Interest rate	-
K_4	Modified load	-

K_{eq}	Equilibrium constant	-
K	Pre-exponent factor	-
L_W	Designed lean solvent mass flow rate	kg/s
m_i	Mass flow rate of species i	kg/s
P	Pressure of the gas	Pa
Q_{cool}	Total cooling duty of CO_2 capture and compression	MW
Q_{reb}	Reboiler duty	kJ/mol_{CO2}
Q_{steam}	Heat of the extracted steam	MW
R	Universal gas constant	J/mol·K
R	Reaction rate	mol/L·s
s_0	Entropy at the reference state	J/kg·K
T	Absolute temperature of the gas	K
$T_{Eva,Sat}$	Refrigerant saturation temperature	K
T_{reb}	Reboiler temperature	K
T_{sink}	Sink temperature	K
T_{steam}	Steam temperature	K
T	Lifetime	yr
v	Molar volume	m^3/mol
W_{comp,CO_2}	Compression work of the standard compression train	kJ/mol_{CO2}
$W_{comp,HP}$	Compression work of the HP compressor	kJ/mol_{CO2}
W_{comp}	Total compression work	kJ/mol_{CO2}
W_{eq}	Total equivalent work	kJ/mol_{CO2}
W_{heat}	Equivalent work of heat duty	kJ/mol_{CO2}
W_n	Work of component n	MW
$W_{net,cycle}$	Net power output of the sCO_2 cycle	kJ/mol_{CO2}

W_{pump}	Pump work	kJ/mol_{CO2}
Greek letters		
ΔT_{cw}	Temperature increase of the cooling water	K
μ_L	Viscosity of liquid stream	Ns/m^2
ρ_L	Density of liquid	kg/m^3
ρ_G	Density of gas	kg/m^3
φ_{cw}	Specific auxiliary power duty	MJ/kg_{CO2}
ε	Exergy efficiency	-

Abbreviations

ACC	Annualized capital cost
AFS	Advanced flash stripper
AIC	Absorber intercooling
AMP	2-amino-2-methyl-1-propanol
APEA	Aspen Process Economic Analyzer®
AR	Afforestation and reforestation
BEC	Bare erected cost
BECCS	Bioenergy with carbon capture and storage
BFBC	Bubbling fluidized-bed combustion
BFPP	Biomass-fired power plant
BIGCC	Biomass-based integrated gasification combined cycle
BIGFC	Biomass-fuelled integrated gasification fuel cell
CAPEX	Capital expenditure
CCC	CO_2 capture cost
CCS	Carbon capture and storage
CFBC	Circulating fluidized-bed combustion
CFPP	Coal-fired power plant
CHP	Combined heat and power
CV	Calorific value
DAC	Direct air capture
DEA	Diethanolamine
DEEA	Diethylethanolamine
DEGMEE	Diethylene glycol monoethyl ether
DIPA	Diisopropanolamine

DWHX	Drain water heat exchanger
EC	Engineering and contractor
EDA	Ethylenediamine
EG	Ethylene glycol
EGR	Exhaust gas recirculation
ELECNRTL	Electrolyte Non-Random Two-Liquid
EoS	Equation of state
EPC	Engineering Procurement and Construction
EW	Enhanced weathering
FBC	Fluidized bed combustion
FD	Forced draft
FGD	Flue Gas Desulfurization
FHR	Flue gas heat recovery
FPUMPTB	Boiler feed pump turbine
FWHX	Feedwater heat exchanger
GHG	Greenhouse gas
GPDC	Generalised pressure drop correlation
GWP	Global Warming Potential
HP	Heat pump
HP	High-pressure
ID	Induced draft
IGCC	Integrated gasification combined cycle
IHS	Inter-heated stripper
L/G	Liquid-to-gas
LCA	Life cycle assessment

LCOE	Levelized cost of electricity
LP	Low-pressure
LVR	Lean vapour recompression
MAPA	N-methyl-1,3-propane diamine
MDEA	Methyldiethanolamine
MEA	Monoethanolamine
MNPZ	N-nitrosopiperazine
MPS	Multi-pressure stripper
NET	Negative emission technology
NGCC	Natural gas combined cycle
NMF	N-methylformamide
NSGA-II	Non-dominated sorting genetic algorithm
O&M	Operation and maintenance
OC	Owner's cost
PA	Primary air
PC	Process contingency
PCB	Pulverised coal boilers
PCC	Post-combustion carbon capture
PE	2-piperidineethanol
PJC	Project contingency
PR-BM	Peng-Robinson with Boston-Mathias modifications
PZ	Piperazine
R290	Propane
RITE	Research Institute of Innovative Technology for the Earth
RK	Redlich-Kwong

RSP	Rich solvent preheating
RSR	Rich solvent recycles
RSS	Rich solvent split-flow
sCO_2	Supercritical CO_2 cycle
SCR	Selective Catalytic Reduction
SHA	Sterically hindered amine
SQP	Sequential quadratic programming
SRP	Separation Research Program
SSE	Side stream extraction
TDC	Total direct cost
TETA	Triethylenetetramine
TIC	Total indirect cost
TPC	Total plant cost

Chapter 1 Introduction

1.1 Background

1.1.1 CO_2 emissions and climate change

To address climate change driven by greenhouse gas (GHG) emissions, the Paris Agreement introduced the goal of limiting the rise in global average temperature to no more than 2°C above pre-industrial levels (UNFCCC, 2015).

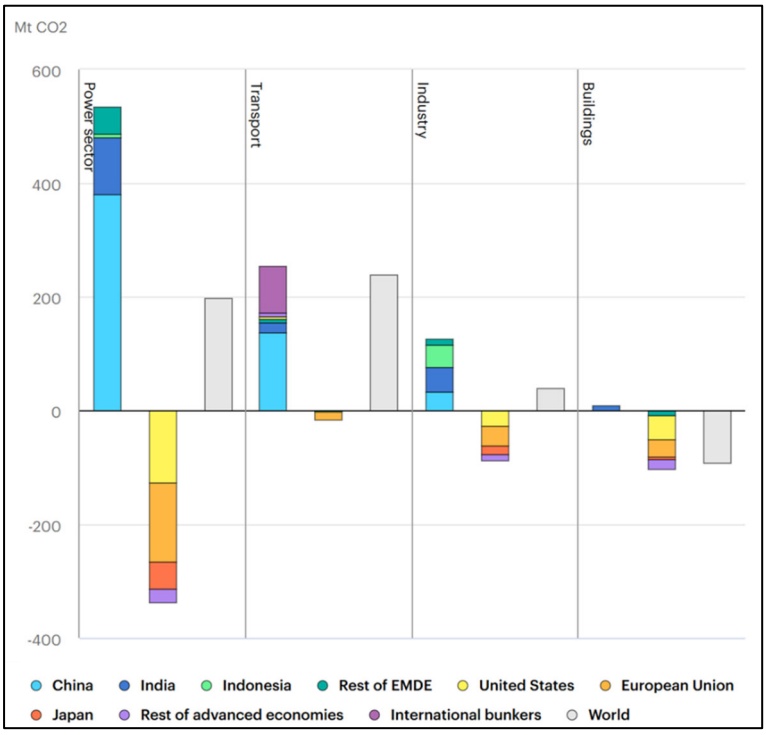

Figure 1.1 CO_2 emissions increase from combustion by sector and region from 2022 to 2023 (IEA, 2024a)

The power sector is one of the significant sources of carbon emissions globally. As presented in Figure 1.1, in 2023, power generation shows the second-largest CO_2 emission increase among different industrial processes (IEA, 2024a). The increase in emissions in the power sector mainly comes from emerging markets and developing economies, e.g., China and India. In these developing countries, coal is the dominant energy source. Additionally, coal accounts for around 70% of the global emissions increase from power generation in 2023 (IEA, 2024a). Therefore, to reduce the CO_2 emission from power generation, it is crucial to prioritise finding

a solution to the coal issue. The feasible approaches include transitioning to clean energy, increasing energy efficiency, and deploying carbon capture technologies for power plants.

1.1.2 Biomass-fired power generation

Bioenergy is a form of renewable energy that can produce electricity, biofuel, and other energy types using biomass feedstock. Unlike other renewables such as solar and wind power, bioenergy is less influenced by environmental conditions, offering a more stable and consistent energy supply. Furthermore, it is considered the only renewable source that can replace fossil fuels in applications like heat production, electricity generation, and transportation fuel (Kemper, 2015). So, it is regarded as one of the most promising renewable energy options for the future. According to the IEA (2024c) report, biomass power generation reached 17.2 EJ in 2023, an increase of 3.2 EJ compared with 2022, and it is expected to reach 20.4 EJ in 2030.

Although biomass is a potential alternative to coal, due to its higher moisture and ash content, it has a lower energy density than coal. This limitation can reduce net power efficiency and contribute to issues like slagging and corrosion. Thus, some pre-treatment approaches are applied to enhance the quality of the biomass feedstock.

At present, torrefaction and steam explosion are two widely used pre-treatment methods for biomass (Livingston et al., 2016). Torrefaction heats and dries biomass at 250–350°C in an oxygen-free environment, effectively lowering its moisture and volatile content. Steam explosion breaks down wood fibres through an explosive decompression process with the presence of steam at 180–220°C. Both techniques can help improve the biomass's bulk density and calorific value (CV).

Three main approaches for using biomass in fuel-fired steam-cycle power plants are presented as follows (Livingston et al., 2016):

- Co-firing biomass with coal in pulverised coal boilers (PCB).
- Converting existing coal-fired power plants (CFPPs) into dedicated biomass-fired power plants (BFPPs).
- Constructing new BFPPs equipped with grate-fired or fluidised bed combustion (FBC) systems.

Most existing biomass plants generate electricity through direct combustion of biomass to heat the feedwater to high-temperature, high-pressure steam to drive turbines (Lam et al., 2019). This can be achieved through converting the CFPPs to biomass co-firing or biomass-only power plants.

The commonly used biomass co-firing methods are (Lempp, 2013):

- Direct co-firing, where biomass is sent and burnt directly in an existing PCB.
- Indirect co-firing, where the syngas generated from biomass gasification are burnt in the PCB.
- Parallel co-firing, where biomass is combusted in a separate furnace using the heat generated by another PCB.

An increasing number of CFPPs have been retrofitted to co-firing plants. Roni et al. (2017) reviewed various co-firing power plants in the US and Europe and compared the different co-firing and combustion technologies applied. Cutz et al. (2019) pointed out that Europe has most of these co-firing plants. By 2019, over 150 co-firing facilities were located in this area, with Finland having 78 and Germany having 27 co-firing plants.

Currently, more co-firing plants have converted to biomass-only power plants. For example, the DRAX power station in the UK (Livingston et al., 2016) and Avedøre Power Station in Denmark (Orsted, 2024). This has been achieved through the support of government policies and incentives in the UK and Denmark (Cross et al., 2021).

To implement biomass more efficiently, it was proposed that FBC technology be applied to the biomass boiler. FBC can improve the fuel-oxidant mixing and thus optimise heat transfer processes (Yin, 2013)Two mainly used FBC techniques are bubbling fluidized-bed combustion (BFBC) and circulating fluidized-bed combustion (CFBC).

1.1.3 Carbon capture technologies

Carbon capture is a technique to prevent CO_2 from being emitted into the atmosphere. As shown in Figure 1.2, the global capture capacity has exceeded 50 Mt CO_2 annually (IEA, 2024c). While the planned capacity for 2030 has grown to over 1000 Mt/yr, the operating and planning projects achieve only around 40% of the capacity needed to meet the Net Zero Scenario target

for 2030.

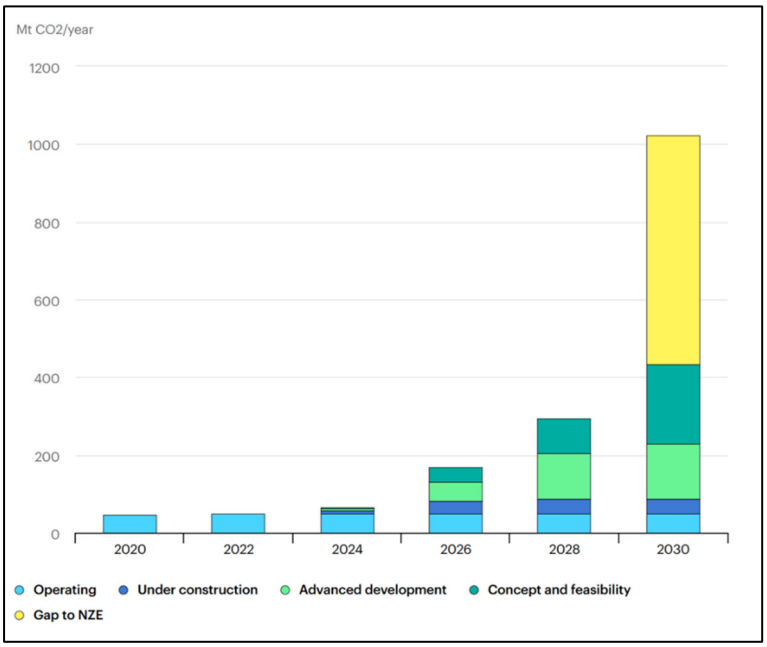

Figure 1.2 Capacity of existing and planned large-scale CO_2 capture projects compared to the net zero scenario, 2020-2030 (IEA, 2024c)

Carbon capture methods include the post-combustion, pre-combustion and oxyfuel process (Wang et al., 2011).

The pre-combustion carbon capture process involves gasifying fuels with the presence of air or oxygen to produce syngas (a mixture of CO and H_2), the water-gas shift reaction to convert the CO to CO_2, and CO_2 separation units before combustion. This method benefits from smaller reaction equipment, reducing facility costs, but it also faces efficiency losses and high resource demands for cooling the syngas.

Oxyfuel combustion burns fuel in a pure oxygen environment, resulting in flue gases with a high CO_2 concentration that simplifies capture. Oxyfuel separation requires substantial energy, leading to high capital and energy expenses.

PCC is a technique for absorbing CO_2 from the flue gases of power plants or other industrial processes. Compared with other methods, post-combustion carbon capture (PCC) can be applied to industrial facilities without significant modifications to the original process.

The methods for PCC include chemical absorption with solvents, physical adsorption,

membrane separation, and cryogenic separation. Chemical absorption using solvents is the most common technology and has been applied commercially (Wu et al., 2020). Figure 1.3 illustrates a standard flowsheet for PCC process using chemical absorption.

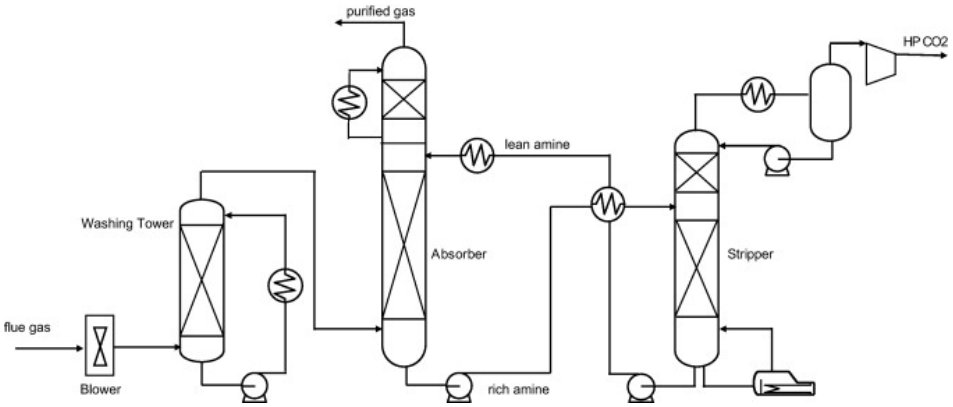

Figure 1.3 Process flowsheet of a standard PCC process using chemical absorption (Raynal et al., 2011)

Firstly, flue gas from power plants undergoes a pre-treatment process to remove the NO_X, SO_X and fly ash. Following this, the treated flue gas enters the bottom of the absorber, where it reacts with the solvent sprayed from the top at approximately 40–45°C. The solvent, after absorbing CO_2 in the flue gas, becomes the rich solvent. The rich solvent is then pumped to the heat exchanger to be heated and transferred to the stripper for regeneration at approximately 110°C. After the regeneration process, the concentrated CO_2 exits the top of the stripper and is condensed in a condenser. Simultaneously, the regenerated lean solvent leaves the stripper from the bottom, goes through a heat exchanger to be cooled down to 40^{o}C and returned to the absorber (Wang et al., 2011).

1.1.4 Bioenergy with carbon capture and storage (BECCS)

To meet the 2°C or 1.5°C climate targets, negative emission technologies (NETs) play a crucial role in reducing CO_2 levels in the atmosphere. According to Emenike et al. (2020)The main NET approaches include:

1) Afforestation and reforestation (AR): Planting trees or restoring forests for sequestering CO_2 through natural photosynthesis.
2) BECCS: Capturing CO_2 emissions generated by biomass-based industries.
3) Direct air capture (DAC): Extracting CO_2 directly from the atmosphere through chemical

absorption.

4) Enhanced weathering (EW): Utilizing crushed minerals for CO_2 sequestration forming stable carbonates.
5) Ocean-based methods: Increasing the ocean alkalinity or stimulating the plankton growth to enhance CO_2 absorption by the ocean.
6) Soil carbon sequestration: Boosting the soil's capacity to store carbon through improving land management.

Smith et al. (2016) assessed the future development and challenges associated with different NET technologies. Their analysis highlighted that BECCS is more energy-efficient and cost-effective compared to DAC while also offering more significant CO_2 removal potential than EW and AR. Despite these advantages, the development of applying BECCS with lower costs and energy consumption remains a challenge. Additionally, when using BECCS, some environmental factors, including the sustainability of biomass, as well as impacts on land and water resources, should be assessed.

BECCS achieves negative emissions by sequestering CO_2 during biomass growth and capturing the CO_2 released during its utilisation. Beyond capturing carbon during electricity or heat generation, BECCS can also be applied to other biomass-based processes, such as biofuel production, hydrogen manufacturing, and various industrial applications using biomass as a feedstock (Schakel et al., 2014).

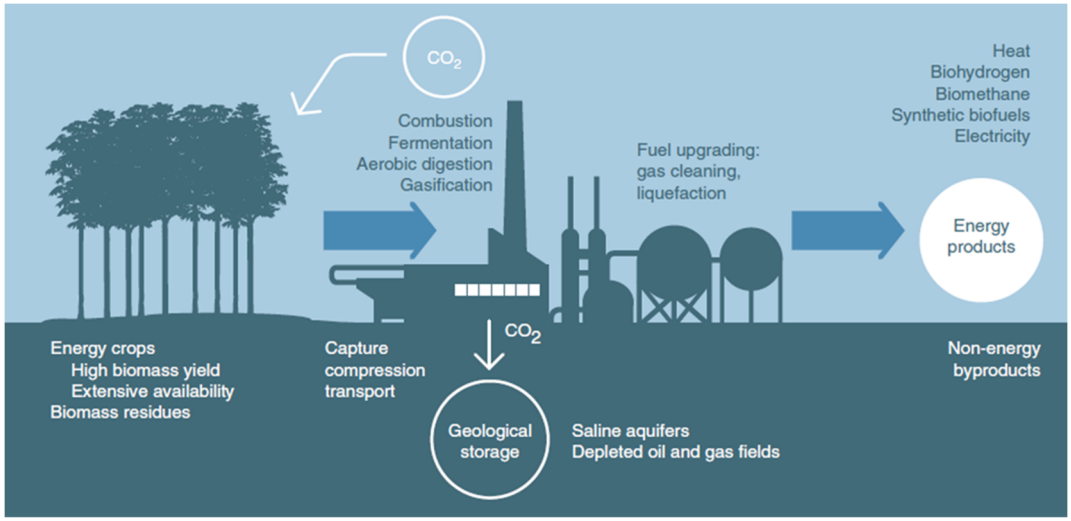

Figure 1.4 The flowsheet of the BECCS process (Canadell and Schulze, 2014)

Figure 1.4 illustrates the typical BECCS process. Energy crops and biomass residues are the most common feedstocks for this technology. As biomass grows, it absorbs CO_2 from the atmosphere, resulting in lower atmospheric CO_2 levels. These biomass feedstocks are then used to generate energy products through processes such as combustion, gasification, fermentation, or aerobic digestion. The CO_2 emitted during these processes is captured using carbon capture technologies, compressed, and sent to geological storage sites.

IEAGHG (2014) summarised various BECCS approaches, including (a) biomass-only or co-firing plants with carbon capture and storage (CCS), (b) biomass-fired CFBC power plants with CCS, (c) biomass co-firing integrated gasification combined cycle (IGCC) power plants with CCS, (d) biomass-based integrated gasification combined cycle (BIGCC) power plants with CCS, (e) advanced biofuel production based on biomass gasification, and (f) Fischer-Tropsch synthesis. This study will focus on BECCS approaches based on BFPP, which are further introduced in Chapter 2.

1.2 Motivations

With the rising need to mitigate climate change, there is a growing focus on decarbonising power generation systems. BECCS is recognised as an effective negative emission technology. Biomass growth is a natural CO_2 sequestration process, making using biomass as a feedstock widely regarded as a carbon-neutral technology.

Amine-based PCC has proved to be a mature decarbonisation technology and has been fulfilled commercially. However, the high energy consumption and high capital and operating costs have limited its wide application at a large scale. Implementing new solvents is a popular strategy for enhancing the energy and economic performance of the PCC process. Piperazine (PZ), a cyclic diamine which can theoretically absorb two moles of CO_2 per mole of amine, has been used. Its high absorption capacity reduces the solvent rate, thereby lowering the energy consumption for solvent regeneration (Plaza, 2011). Another approach to improving energy efficiency is using advanced process configurations. Pilot plant experiments conducted at the University of Texas in the USA showed that the advanced flash stripper (AFS) configuration demonstrated higher energy efficiency compared to the conventional process (Lin et al., 2016). Nevertheless, in addition to the energy performance, the economic and environmental impacts of using complex process configurations also need to be evaluated.

1.3 Aim and Objectives

This study aims to conduct a techno-economic analysis, optimization and life cycle assessment (LCA) to evaluate the energy efficiency, cost-effectiveness and decarbonization potential of a 550 MW supercritical BFPP integrated with different configurations of the PCC process, utilizing monoethanolamine (MEA) and PZ as solvents. This aim will be achieved through the following objectives:

- Literature review on BECCS, BFPP and solvent-based PCC process.
- Model development, validation and scale-up of the solvent-based PCC processes using MEA and PZ
- Model development and sensitivity analysis of different configurations of large-scale PZ-based PCC process for a 550 MWe BFPP.
- Techno-economic analysis and process optimisation of different solvent-based PCC processes.
- Simulation and model comparison of a 550 MWe supercritical BFPP and integration with different solvent-based PCC processes.
- Energy and exergy of different integration designs.
- LCA of BFPP integrated with different solvent-based PCC processes.

1.4 Novel contributions

The novel contributions of this PhD research are as follows:

(1) Integration of supercritical BFPP with PZ-based PCC at large scale: Previous studies have explored the modelling and simulation of solvent-based PCC processes for large-scale power plants using MEA as the solvent (Ali et al., 2017; Liu et al., 2015; Nawaz and Ali, 2020; Olaleye et al., 2015; Olaleye and Wang, 2017). Several studies (Gaspar and Fosbøl, 2016; Otitoju et al., 2021; Pérez-Calvo and Mazzotti, 2022; Plaza and Rochelle, 2011) have focused on the use of PZ for large-scale PCC in power plants, demonstrating that it can reduce energy consumption compared to MEA. This energy saving is attributed to the advantage of PZ, including higher CO_2 absorption capacity and greater resistance to both oxidative and thermal degradation (Dugas, 2009; Freeman et al., 2009, 2010). These studies mainly focused on PCC applications for CFPP or natural gas combined cycle (NGCC) plants. To the best of the author's knowledge,

no modelling and simulation studies of BFPP integrated with PZ-based PCC have been reported. This work presents the development of a 550 MWe supercritical BFPP integrated with a PZ-based PCC model using Aspen Plus® V11.

(2) Techno-economic analysis of large-scale PZ-based PCC process for a supercritical BFPP: This study presents the first techno-economic analysis of a solvent-based PCC process using PZ for a BFPP. To reduce the energy consumption of the PCC process, different process configurations were evaluated. In addition, to study the energy and efficiency penalty caused by the implication of PCC to the BFPP, an energy analysis was carried out. As cost is a critical factor in large-scale PCC deployment, the economic analysis of the PCC process using different solvents (MEA and PZ) and different process configurations was conducted using the Aspen Process Economic Analyzer® (APEA). The capital expenditure (CAPEX) and operation and maintenance (O&M) expenditure of each configuration were computed and analysed.

(3) Optimisation of PZ-based PCC processes based on CO_2 capture cost: Solvent concentration is a sensitive factor in the CO_2 capacity of the solvent. Additionally, stripper pressure is one of the key factors that influence both the regeneration heat duty and the CO_2 compression work. There is a lack of studies focused on optimising the economic performance of the PCC process using PZ at different solvent concentrations and stripper pressures. Therefore, to analyse how PZ concentration and stripper pressure impact the CO_2 capture cost and to determine the optimal concentration and pressure, process optimisation was conducted.

(4) Exergy analysis of supercritical BFPP integrated with PCC process using PZ: Previous studies on improving the thermodynamic performance of BECCS processes focused on using different biomass feedstock and power generation approaches (Akrami et al., 2020; Chang et al., 2023; Parvez and Khan, 2020; Yan et al., 2021). In this work, the exergy analysis was carried out for BFPP integrated with different PCC processes to improve the thermodynamic performance of BECCS by optimising the carbon capture process. Additionally, compared with other biomass-based power generation approaches, BFPP can be converted from CFPP, which is the main source of CO_2 emission from the power sector. The feasibility of converting CFPP to BFPP has been demonstrated in DRAX (UK) and Avedøre (Denmark) power stations. This work is the first to carry out an exergy analysis of a supercritical BFPP integrated with the PCC

process using PZ, offering an approach to identifying thermodynamic inefficiencies within the BECCS system.

(5) **LCA of supercritical BFPP integrated with PCC process using PZ:** LCA is a vital approach to assessing the environmental impact of negative emission technologies like BECCS. Existing LCA studies for biomass-related power generation integrated with PCC often use MEA as the solvent. This study carried out the LCA for BFPP integrated with an optimised PCC process using PZ solvent.

1.5 Scope of this study

This work mainly focuses on the simulation, analysis and optimisation of the BFPP and solvent-based PCC process.

- For the solvent-based PCC process, the study only considers using MEA and PZ as the solvent.
- The modelling and simulation of the carbon storage and utilisation processes are not included in this work.
- In Chapters 3 to 5, the PCC and BFPP processes are modelled at steady state using Aspen Plus® V11.
- In Chapter 6, the LCA follows a cradle-to-grave approach, assuming that CO_2 is ultimately stored in saline aquifers. CO_2 utilization methods are not considered in this study.

1.6 Research methodology

The research methodology involves conducting a literature review to identify research gaps, model development and validation of PCC and BFPP units, model integration and performance through sensitivity, techno-economic analysis and LCA. More details on the research methodology of this study are presented in Figure 1.5.

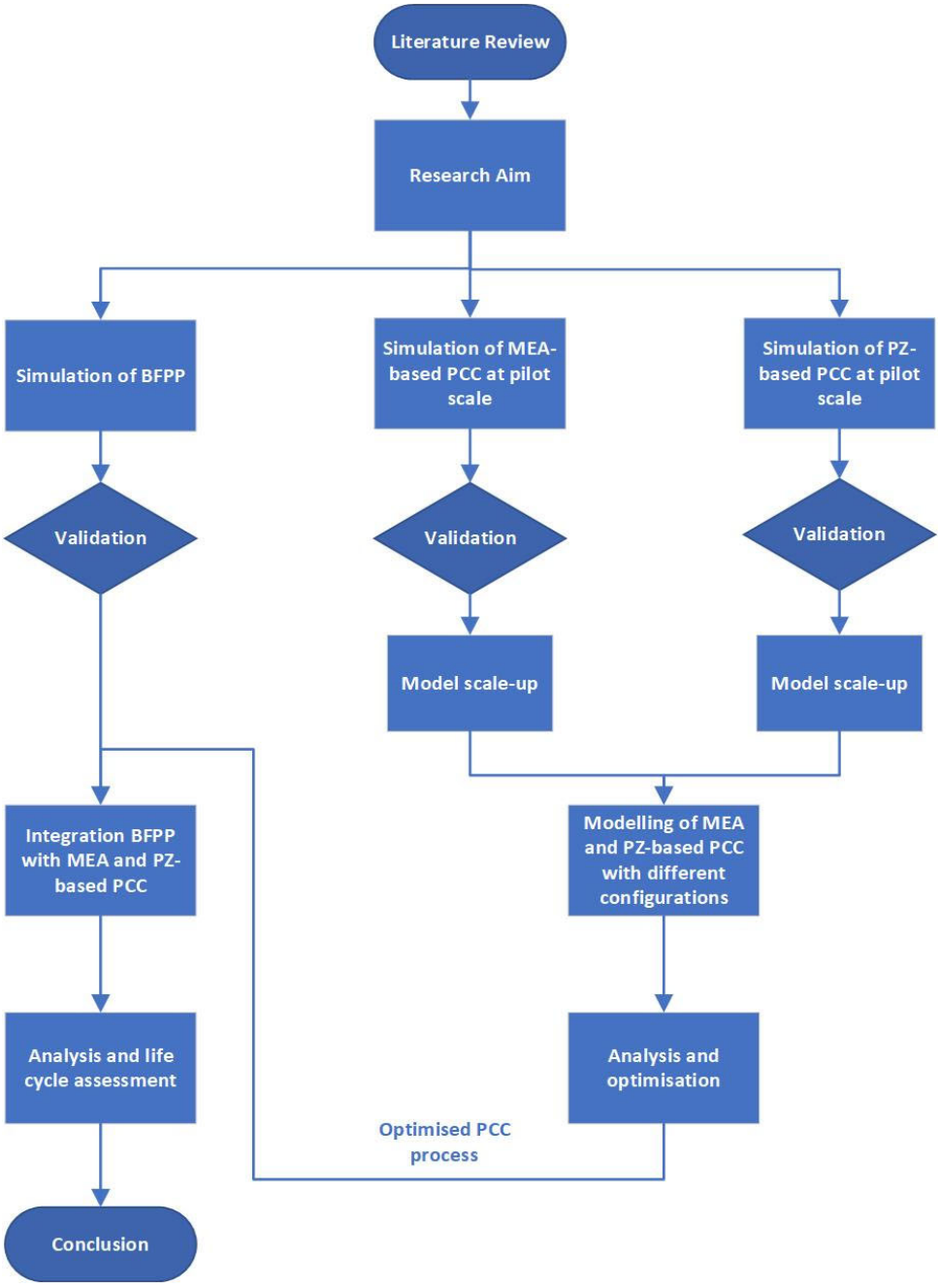

Figure 1.5 Flowsheet of research methodology

1.7 Software used for this study

1.7.1 Aspen Plus®

The BFPP and PCC units will be simulated using Aspen Plus® V11, a process simulation software developed by AspenTech. This software is used in chemical engineering to design, simulate, and optimise a wide range of industrial processes. Aspen Plus® has a comprehensive database containing numerous physical and thermodynamic properties of pure substances,

allowing it to model chemical processes involving electrolytes, gas, solids, and other components (Aspentech, 2024a).

1.7.2 Aspen Economic Process Analyzer®

APEA is a tool designed for economic evaluation. It can provide the estimation of the system's CAPEX and O&M expenditure (Aspentech, 2024b). APEA can be used to calculate the costs for the model developed by Aspen HYSYS® and Aspen Plus®.

1.7.3 SimaPro®

SimaPro® is a powerful LCA software designed to deliver high-quality analyses while keeping up with the latest data (SimaPro, 2024). It allows users to carry out sensitivity analysis of different parameters and use Monte Carlo analyses to address data uncertainty. Some important environmental databases are available in SimaPro®, such as Ecoinvent and Agri-footprint. In addition, it also includes advanced impact assessment methods such as ReCiPe and IPCC. Moreover, it is a reliable tool for tracking the footprint of carbon and water and conducting Environmental Product Declarations and Product Environmental Footprints studies.

1.8 Outline of the thesis

This thesis is divided into seven chapters, with the remaining chapters outlined as follows:

In Chapter 2, the current development of experimental and modelling studies related to BFPP, PCC, and BECCS were critically reviewed. For BFPP, the existing commercial deployments and large-scale model development were presented. For PCC, the commonly used amine-based solvents were evaluated. Additionally, the experiments carried out in pilot-scale and large-scale PCC plants were presented. The steady-state modelling and simulation studies for the PCC process using different solvents and configurations were also reviewed. Additionally, different analysis studies based on the BECCS-related modelling and simulation were assessed.

In Chapter 3, the model development and comparison of the 550 MWe BFPP were proposed. Furthermore, the PCC processes using MEA and PZ solvents were simulated at a pilot scale

through Aspen Plus® V11. The pilot-scale models were then validated using the pilot test data from the University of Kaiserslautern for MEA and the University of Texas at Austin for PZ. Subsequently, the pilot-scale PCC models were scaled up for the removal of CO_2 in the flue gas from the 550 MWe BFPP. Furthermore, to find a cost-effective and energy-efficient large-scale PCC process for the BFPP, different process configurations were simulated using Aspen Plus® V11.

In Chapter 4, sensitivity analysis was conducted to investigate the impacts of key parameters on the heat duty of the carbon capture and compression process. Additionally, the PCC with different process configurations and solvents were analysed and optimised in terms of the energy requirement and costs for carbon capture.

In Chapter 5, the integration of supercritical BFPP with different PCC processes was carried out. Then, the energy analysis was carried out for the different integration designs and compared with the results from Chapter 4. In addition, the exergy analysis was conducted to determine the location of exergy destruction and the potential to improve plant efficiency.

In Chapter 6, the LCA of the BFPP integrated with PCC processes assessed the environmental impacts of the supply chains. The goal and scope, along with the system boundary, were defined, and a life cycle inventory was developed to support the analysis. The impact assessment focused on key environmental indicators to evaluate system performance, including CO_2 sequestration by biomass, CO_2 emissions at each stage, net CO_2 emissions and fuel requirements.

Finally, the conclusions and recommendations of this study are provided in **Chapter 7**.

Chapter 2 Literature Review

2.1 Overview

Chapter 2 reviews the previous research on biomass power generation and amine-based PCC in terms of experimental and modelling studies. In section 2.2, some typical existing large-scale BFPPs around the world are presented. In section 2.3, the modelling and simulation studies on large-scale biomass-cofiring and biomass-only power plants are reviewed. In section 2.4, the details of amine-based PCC technology are assessed, including the review of the amine-based solvents for CO_2 capture, the pilot plant tests using different solvents and the commercial-scale amine-based PCC plants. Section 2.5 reviewed the previous modelling and simulation studies on amine-based PCC, including the modelling principles and modelling studies on the PCC process using different solvents and process configurations. In section 2.6, the energy, exergy, economic, life cycle assessments and optimisation of BFPP and PCC processes are presented. Finally, section 2.7 briefly summarises the findings from the literature review.

2.2 Large-scale biomass-fired power plants worldwide

2.2.1 Avedøre Power Station, Denmark

As one of the most efficient power plants globally, the Denmark Avedøre Power Station can achieve up to 89% energy efficiency in combined heat and power (CHP) production (Orsted, 2024). Avedøre 1, initially a coal-fired CHP plant, has been transitioning to biomass-fired. It now operates on biomass during winter and switches to coal in summer. When using biomass, it achieves a power generation capacity of 254 MWe for electricity and 359 MWth for heat (MHI, 2024).

Avedøre 2 was initially designed to burn biomass. Its total capacity is 575 MWe for electricity and 545 MWth for heat, with a power generation capacity of 394 MWe and 497 MWth specifically for CHP production (SOG, 2024). The main steam operates at a pressure of 300 bar with a temperature of 580°C, while the reheated steam reaches 600°C (Ziebik et al., 2010).

Figure 2.1 Avedøre power station, Denmark (Orsted, 2024)

2.2.2 DRAX Power Station, UK

The DRAX Power Station, situated in North Yorkshire, England, is recognised as the world's largest BFPP (Fajardy et al., 2021). Initially constructed as a CFPP, Drax began its transition to biomass-based energy generation in 2013 (Harris, 2021). The power station has six 645 MWe units, all of which were converted to biomass-fired by 2023 (Drax, 2023). Currently, Drax has a total capacity of 3,906 MW from biomass energy generated using compressed wood pellets.

Figure 2.2 Drax Power Station, UK (YorkPress, 2014)

2.2.3 Polaniec Biomass Power Plant, Poland

Połaniec in Poland is one of the largest BFPPs around the world. It applies a 205 MW CFB boiler with a plant efficiency of 36%. The biomass unit primarily uses wood chips and agricultural residues as feedstock, consuming over one million tons of these materials annually (PowerTech, 2014). The CFB boiler produces the main steam at a flow rate of 570 t/h, with a pressure of 127.2 bar and a temperature of 565 ^{o}C. The reheated steam operates at a pressure

of 20 bar and a temperature of 565 °C.

Figure 2.3 Polaniec Biomass Power Plant, Poland (PowerTech, 2014)

2.2.4 Alholmens Kraft Power Station, Finland

The Alholmens Kraft Power Station in Finland is the largest biomass cogeneration facility worldwide. The plant has a capacity of 265 MW for electricity generation and 60 MW for district heating. It also supplies 100 MW of process steam and heat to a paper mill (Alholmens, 2001).

The biomass units use wood-based fuels sourced from paper mills and the forestry sector. The station is equipped with a 500 MW_{th} CFB boiler, the largest biomass-fired boiler. The boiler generates steam with a pressure of 165 bar and a temperature of 545°C.

Figure 2.4 Alholmens Kraft power station, Finland (Alholmens, 2001)

2.3 Modelling and simulation of large-scale biomass-fired power plants

Before sending the biomass to the boiler, pretreatments such as torrefaction or steam

explosion were applied to improve the quality of bio-feed further. Li et al. (2014) conducted the simulation of a 220 MW subcritical CFPP with biomass co-firing integrated with biomass torrefaction in Aspen Plus®. The torrefaction process, illustrated in Figure 2.5, used palm kernel shells as the feedstock. Additionally, it investigated the impacts of varying torrefaction temperatures from 200 to 300 °C on both the plant efficiency and the energy consumption for the torrefaction process. Results showed that increasing the torrefaction temperature reduced the energy consumption for milling biomass. However, excessive torrefaction would lead to an increase in torrefaction energy demand and negatively impact the plant's electrical efficiency.

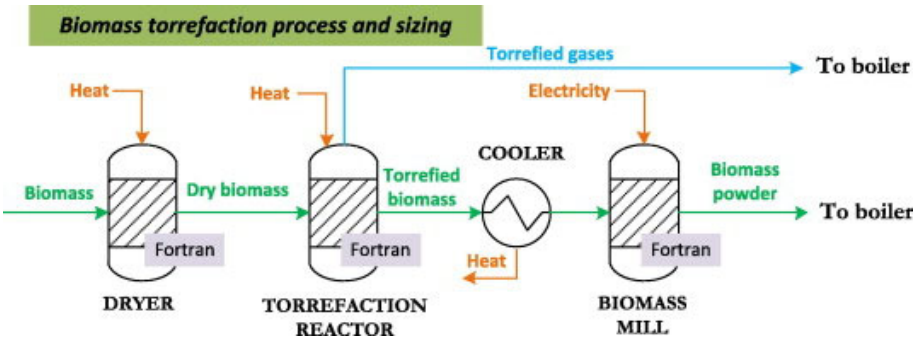

Figure 2.5 The process of torrefying biomass (Li et al., 2014)

In previous studies, the feasibility of cofiring biomass to the large-scale CFPP is investigated through modelling and simulation. Nawaz and Ali (2020) simulated a 580 MW SCPP in Aspen Plus® and validated based on the NETL (2015) Report. Then, three biomass co-firing scenarios were analysed: constant heat input, constant fuel input, and constant Reynolds number. The study evaluated CO_2 emissions, net plant efficiency, and power output for varying biomass co-firing ratios. The results demonstrated that blending biomass with coal significantly reduces carbon dioxide emissions despite increasing fuel consumption and reducing plant efficiency compared to coal-only power plants.

Cebrucean et al. (2020) simulated the 550 MWe subcritical and supercritical with biomass co-fired CFPP in Aspen Plus® to evaluate the energy and environmental performance. The subcritical plant was modelled with a conventional steam cycle, while the supercritical plant utilised an advanced steam cycle configuration. The study compared key indices, including net plant efficiency, specific fuel consumption, and CO_2 emissions, for both systems. The results

demonstrated that the efficiency of the supercritical plant is 2.4% higher than the subcritical plant, resulting in reduced required fuel and lower emissions of CO_2, NO_X, and sulphur derivatives.

Furthermore, the performance of biomass-only power plants was compared with different types of power plants. Ali et al. (2017) conducted the simulation of an 800 MWe SC CFPP based on NETL (2010) report using Aspen Plus®, which was converted to BFPP burning biomass pellets. Then, the BFPP and CFPP were integrated with MEA-based PCC. Additionally, NGCC with or without exhaust gas recirculation (EGR) were both integrated with PCC. Subsequently, the different power plants integrated with PCC were compared in terms of energy and economic performance. The result was that the NGCC with EGR integrated with PCC showed the highest net efficiency and the lowest efficiency penalty. The BFPP-PCC system has the highest specific CO_2 capture flow rate. This is attributed to the lower flow rate and higher CO_2 concentration of flue gas. Additionally, among these power plants integrated with PCC processes, BFPP-PCC is the only process that can achieve negative CO_2 emissions.

Yan et al. (2021) simulated three biomass-based power generation systems: BFPP-CCS, BIGCC-CCS, and biomass-fuelled integrated gasification fuel cell (BIGFC) using Aspen Plus®. The net electric efficiency, levelized cost of electricity (LCOE), and CO_2 removal were used as the index to evaluate their energy, economic, and environmental performance. The results showed that the BIGFC system achieved the highest efficiency (50.5%) and lowest LCOE ($0.0493/kWh), while BFPP demonstrated the highest CO_2 removal (−0.923 kg CO_2/kWh). Although BFPP has lower efficiency (30.7%) and a slightly higher LCOE ($0.0584/kWh) than the other systems, its technological simplicity, lower capital costs, and greater accessibility make it easier to implement and operate, providing a practical solution for immediate deployment.

Additionally, the BFPP was modified to integrate with power generation processes using different types of renewable energy. Chen et al. (2021) analysed a hybrid solar-aided biomass-fired CHP system based on a Rankine cycle. Two operation modes were evaluated: cogeneration mode during the heating season and power generation mode during the non-heating season. Energy and economic analyses were conducted using EBSILON Professional. The results showed that integrating solar energy into a biomass-fired CHP system can reduce biomass consumption by 4.9% to 7.2%,

depending on the operational mode. The cogeneration mode achieved a solar-to-electricity efficiency of 19.38%, with an additional power output of 1.64 MW, while the power generation mode achieved 16.92% efficiency and an additional 1.51 MW output. However, the LCOE of the hybrid CHP is 6–9% higher than that of a biomass-only system due to the additional capital costs of the solar-aided system.

2.4 Solvent-based PCC technology

2.4.1 Amine-based Solvents for PCC

2.4.1.1 Aqueous alkanolamines

Aqueous alkanolamine solvents are widely utilised for CO_2 absorption and are categorised based on the degree of substitution at the nitrogen atom in the amine molecule. These include: primary amines, such as MEA; secondary amines, including diethanolamine (DEA) and diisopropanolamine (DIPA); and tertiary amines, such as methyldiethanolamine (MDEA) (Peu et al., 2023).

Primary and secondary alkanolamines exhibit a faster reaction rate compared to tertiary amines. However, their reactions require significant heat input and produce stable carbamate compounds, leading to high regeneration costs and limiting their practical application (Peu et al., 2023). Additionally, MEA and DEA are more prone to thermal degradation at high temperatures, further increasing the overall solvent costs.

In contrast, tertiary alkanolamines, such as MDEA, have a slower reaction rate because they are prone to form bicarbonates in CO_2 hydrolysis reactions than carbamates. Despite the lower reaction rate, they offer advantages, including lower thermal degradation and reduced regeneration heat requirements. These properties make tertiary amines suitable for blending with primary or secondary amines, such as MEA or DEA, to reduce solvent penalty (Loachamin et al., 2024).

2.4.1.2 Sterically hindered amines (SHAs)

SHAs are a typical type of amine-based solvents for CO_2 absorption, classified into primary and secondary SHAs. Primary SHAs, like 2-amino-2-methyl-1-propanol (AMP), have an amino group attached to a tertiary carbon. Secondary SHAs, such as 2-piperidineethanol (PE), have

an amino group connected to a secondary or tertiary carbon. The nitrogen in SHAs is surrounded by bulky groups. This makes the carbamates they form less stable. Compared to other amines, SHAs have higher CO_2 absorption capacity, faster reaction rates, and lower degradation rates (Bougie and Iliuta, 2012).

2.4.1.3 Cyclic amine

Another type of amine solvent is cyclic amine, which can be secondary or tertiary amine (Gautam and Mondal, 2023). They are mostly used as activators to enhance solvent performance, for example, adding to solvents like MDEA to boost their reaction rates (Closmann et al., 2009). The commonly used cyclic amine is PZ. PZ, a cyclic diamine, can also be used alone as a CO_2 absorbent due to its lower energy consumption and faster reaction rate (Freeman et al., 2010). It resists thermal degradation up to 165 °C (Davis, 2009), enabling operation at higher stripper temperatures and pressures (Rochelle et al., 2018). However, PZ still has some limitations. At temperatures below 20 °C and low CO_2 loading, it can precipitate as piperazine hydrate ($PZ{\cdot}6H_2O$) (Freeman et al., 2009, 2010). High CO_2 loading may also cause the formation of protonated piperazine carbamate ($H^+PZCOO^-{\cdot}H_2O$). Therefore, to prevent solidification, typical operating conditions for 40wt% PZ are between 40 °C and 150 °C, with CO_2 loadings of 0.2–0.4 mol CO_2/mol alkalinity (Ma et al., 2024; Rabensteiner et al., 2015a). Another drawback is its reaction with nitrite to form N-nitrosopiperazine (MNPZ), a stable and carcinogenic nitrosamine (Nielsen et al., 2013).

2.4.1.4 Biphasic amine solvents

Biphasic solvents include aqueous and non-aqueous types (Zhang et al., 2024). The CO_2 absorption process in biphasic solvents involves the mechanism where the solvent separates into two phases after CO_2 capture: a CO_2-rich phase and a CO_2-lean phase (shown in Figure 2.6). During absorption, reactive amines in the solvent chemically bind with CO_2, forming stable carbamates or bicarbonates. This reaction occurs primarily in the CO_2-rich phase, which concentrates the absorbed CO_2. The CO_2-lean phase remains relatively unaffected and requires less energy during regeneration, making the process more energy-efficient. For example, polyamine biphasic systems like triethylenetetramine (TETA)- diethylethanolamine (DEEA)-sulfolane can achieve a 54.6% reduction (Wang et al., 2020). The main challenge of applying biphasic solvent is the high viscosity of the CO_2-rich phase. Therefore, the balance of

CO_2 absorption capacity and phase viscosity should be considered.

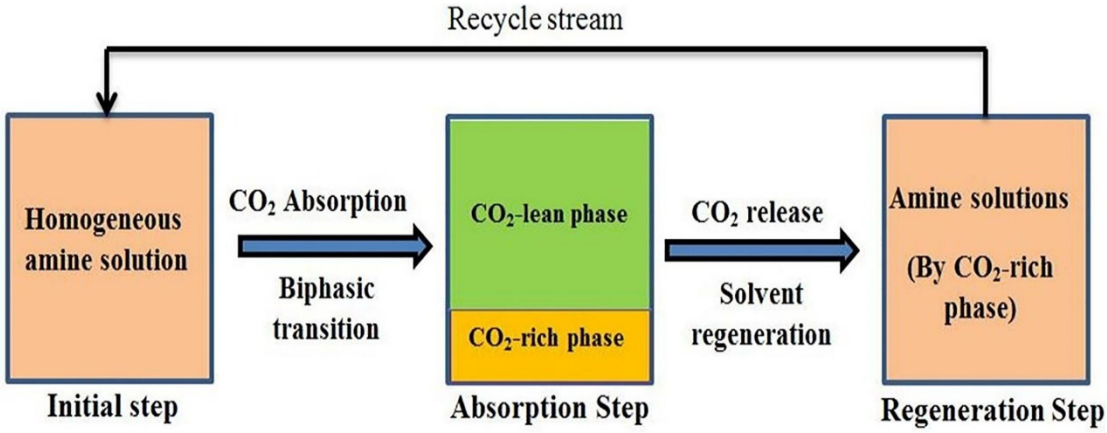

Figure 2.6 Mechanism of CO_2 absorption process in biphasic solvents (Gautam and Mondal, 2023)

2.4.1.5 Non-aqueous amine solvents

In aqueous amine solvents, water is used as the solvent for amine, leading to a massive energy loss associated with the vaporisation of water in solvent regeneration. Therefore, non-aqueous solvents were investigated to replace the water with some organic solvents with lower heat capacity and boiling point (Aghel et al., 2020). These solvents include alcohols (e.g., methanol, ethanol), ethers and glycols (Zhang et al., 2024). Bougie et al. (2019) compared 30wt% MEA in non-aqueous solvents, including diethylene glycol monoethyl ether (DEGMEE), N-methylformamide (NMF), and a mixture of ethylene glycol (EG) and 1-propanol, for CO_2 capture through experiments. Among the solvents, DEGMEE showed the best performance, achieving 78% lower regeneration energy consumption compared to 30wt% aqueous MEA while maintaining efficient absorption/desorption rates. When using non-aqueous amine-based solvents, viscosity is important because high viscosity can hinder mass transfer and liquid transfer.

2.4.2 Pilot plants of solvent-based PCC technology

2.4.2.1 The University of Texas at Austin, USA

The Separation Research Program (SRP) pilot plant is located at the J.J. Pickle Research Center, affiliated with the University of Texas at Austin. This facility can handle flue gas flows ranging from 600 to 1500 m^3/h, with a CO_2 capture capacity of 3 to 6 tons per day. The SRP facility has

conducted several tests on solvent-based PCC, providing reliable experimental data using different solvents. Dugas (2006) presented the experiments involving the standard PCC process using 32.5wt% MEA solvent. Using this standard process configuration of the PCC process, additional pilot tests with other solvents were conducted. For instance, Chen (2007) tested the experiment with potassium carbonate (K_2CO_3) promoted PZ (5m K^+/2.5m PZ), while Plaza (2011) investigated the performance of 8m concentrated PZ. Moreover, experiments were also carried out to evaluate different configurations. Plaza (2011) presented the tests of absorber intercooling and a two-stage flash stripper. Then, Lin (2016) reported the improved configuration, namely AFS, which can achieve the heat duty of 2.1-2.5 GJ/t_{CO2}. Lin (2016) indicated that AFS can reduce the heat duty by 25% compared to the two-stage flash configuration.

2.4.2.2 CSIRO-Tarong power station pilot, Australia

The Tarong pilot plant treats flue gas from a CFPP with a CO_2 concentration of 11.0–13.5 vol% and is designed to process 100 kg/h of flue gas. The plant has a CO_2 capture capacity of 100 kg/h and has been used to test various solvents and process configurations to improve energy performance. Cousins et al. (2012) reported the tests carried out in Tarong using 30wt% MEA as the solvent. Both the standard configuration and the rich-split process modification were evaluated. In the rich-split configuration, a part of the rich solvent is bypassed before entering the heat exchanger and entering the top of the stripper. The results indicated that by using rich-split, the reboiler duty decreased by approximately 7% for split fractions below 15wt%. Cousins et al. (2015) evaluated the performance of the PCC process using 8m PZ (40wt%) as the solvent. The configuration of absorber intercooling was also tested, and up to 10% energy saving was observed.

2.4.2.3 Dürnrohr CO_2 Separation Plant (CO_2 SEPPL), Austria

The CO_2 SEPPL at Dürnrohr in Austria uses the flue gas from CFPP (with 11 vol% CO_2 dry) and NGCC (with 7 vol% CO_2 dry) plants (Rabensteiner et al., 2014b). This facility operates with a flue gas flow rate ranging from 50 to 120 m³/h. Experimental tests with various solvents have been conducted at CO_2 SEPPL. Based on the standard configuration, Rabensteiner et al. (2014) presented the tests of a baseline case using 30wt% MEA. In the same year, experiments with 32wt% ethylenediamine (EDA) were conducted (Rabensteiner et al., 2014a). Subsequently,

Rabensteiner et al. (2015a, 2015b) investigated PCC with 37.6wt% PZ. In 2016, tests using a blend of AMP/PZ (28/17wt%) were carried out (Rabensteiner et al., 2016).

2.4.2.4 CSIRO- AGL Loy Yang, Australia

The Loy Yang pilot plant processes flue gas from a CFPP with a CO_2 concentration of approximately 11–12 vol% and a flow rate of 250 m^3/h, achieving a CO_2 capture capacity of 0.3 tons per day. This pilot consists of two absorbers operating in series for CO_2 capture and a single stripper for solvent regeneration (Artanto et al., 2012). Artanto et al. (2012) reported the tests in the Loy Yang pilot using different solvents, including 30wt% MEA, 20wt% MEA blended with 10wt% AMP and a proprietary solvent from the Research Institute of Innovative Technology for the Earth (RITE). In 2014, another blended solvent, 25wt% AMP+5wt% PZ, was also tested (Artanto et al., 2014).

2.4.2.5 University of Kaiserslautern, Germany

This pilot plant utilises flue gas from a natural gas burner, which can supply flue gas with either 3.8 vol% CO_2 or 6 vol% CO_2 on a dry basis. The flue gas flow rate varies between 30 and 110 kg/h, with a CO_2 capture capacity ranging from 0.1 to 0.5 tons per day. The baseline cases using 30wt% MEA were presented by Mangalapally and Hasse (2011a) and Notz et al. (2012). Different solvents were also tested in this facility. Mangalapally and Hasse (2011b) reported tests with two innovative solvents, CESAR1 and CESAR2. The former is a blended solvent of 28 wt% AMP and 17wt% PZ, while the latter is 32wt% EDA. Von Harbou et al. (2013) further explored CESAR3, a blended solvent containing 27wt% AMP and 19wt% EDA. In addition, Mangalapally et al. (2012) conducted experiments with two other blended solvents :25wt% MDEA combined with 15wt% N-methyl-1,3-propanediamine (MAPA) and 25wt% AMP mixed with 15wt% MAPA.

2.4.3 Commercial-scale amine-based PCC plants

Currently, more commercial deployments on solvent-based PCC have been conducted. In 2024, the number of operational commercial-scale CCS facilities has increased to 50, with over 600 projects in construction, marking a 60% growth compared with 2023 (GCCSI, 2024). CCS technologies have been significantly developed in regions like North America, Europe, and China. Chemical absorption using amine-based solvents has been widely applied for large-

scale PCC plants. These amine-based PCC plants can be classified based on their CO_2 sources, for example, CFPP (Boundary Dam, Petra Nova), steel industry (AL-Reyadah), natural gas processing (Uthmaniyah) and petrochemical refinery (Sinopec Qilu-Shengli). More details on the commercial deployments of PCC are presented in Table 2.1.

Table 2.1 Worldwide amine-based PCC plants at a commercial scale (GCCSI, 2024; SCCS, 2024)

Plant	**SaskPower Boundary Dam**	**Petra Nova**	**AL-Reyadah**	**Uthmaniyah**	**Sinopec Qilu-Shengli**
Location	Saskatchewan, Canada	Texas, USA	Abu Dhabi, UAE	Uthmaniyah, Saudi Arabia	Shandong, China
Operator	SaskPower	NRG Energy, JX Nippon Oil	ADNOC	Saudi Aramco	Sinopec
Solvent	Amine (Cansolv)	Amine (KS-1)	Amine-based	Amine-based	Amine-based
Capture capacity	1 Mt/yr	1.4 Mt/yr	0.8 Mt/yr	0.8 Mt/yr	0.5 Mt/yr
Facility type	CFPP	CFPP	Steel production	Natural gas processing	Petrochemical refinery
CO_2 utilisation	EOR	EOR	EOR	EOR	EOR
Start of operation	2014	2017	2016	2015	2021

2.5 Steady-state model development of the solvent-based PCC process

2.5.1 Model complexity level

When simulating the heat and mass transfer of gas-liquid reactions, the levels of model complexity should be considered. Two widely used methods for describing gas-liquid reactions are the equilibrium-based method and the rate-based method. Kenig et al. (2001) identified five different levels of vapour-liquid reaction models as presented in Figure 2.7.

The basic equilibrium model describes the condition with an equilibrium reaction in a single stage. Based on the basic equilibrium model, the bulk-phase reaction kinetics were considered, which can improve the accuracy to some extent. However, reaction equilibrium is rarely achieved in reality, which would affect the model's reliability.

The rate-based model describes the equilibrium condition. However, it is unable to effectively predict reactions with low rates. Therefore, the enhancement factor is introduced to model pseudo-first-order reactions. Finally, the most detailed model considers the two-film theory, reaction kinetics, and electrolyte effects. This comprehensive model offers reliable modelling of gas-liquid reactions and is widely adopted for simulating CO_2 absorption processes using solvents.

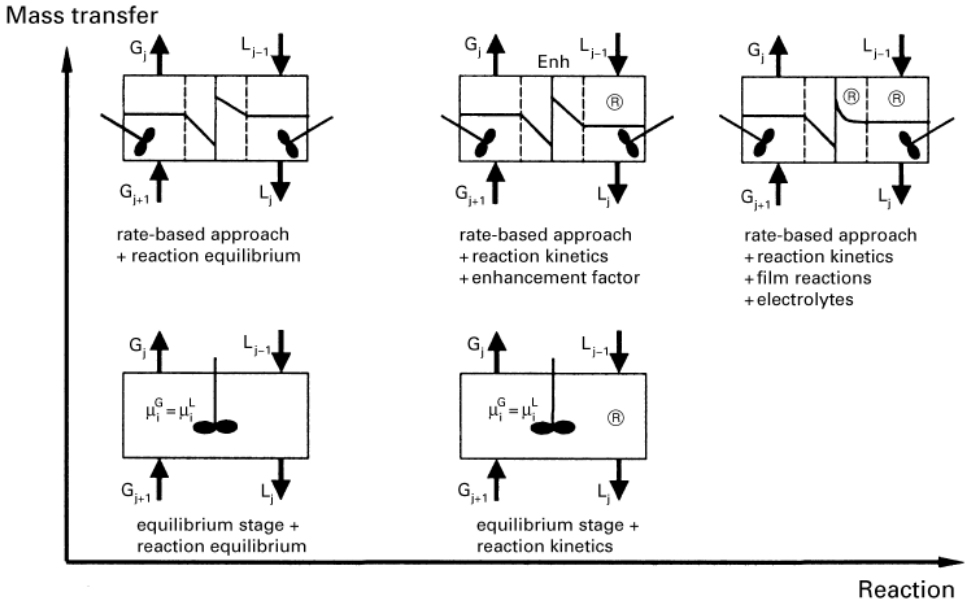

Figure 2.7 Different levels of model complexity gas-liquid reactions (Kenig et al., 2001)

2.5.2 Steady-state modelling and simulation studies of PCC

In previous studies, the PCC process using different solvents was modelled at a steady state. MEA is the most used solvent in these modelling and simulation studies and is widely applied to the large-scale CFPPs or NGCC power plants (Ali et al., 2017; Canepa et al., 2013; Liu et al., 2015; Olaleye and Wang, 2017). The integration of the PCC process was reported to result in an efficiency penalty ranging from 6% to 12% and an energy penalty between 7% and 22%, based on the type of power plant (Canepa et al., 2013; Hassiba and Linke, 2017). Therefore, to find the most efficient integration design, Liu et al. (2015) examined three integration designs based on the steady-state model of a 600 MWe SCPP integrated with MEA-based PCC developed in Aspen Plus®. The designs involve different sources of steam extraction to supply heat for regeneration: (i) from the low-pressure (LP) turbine, (ii) from the crossover between the intermediate-pressure (IP) and LP turbines, and (iii) from an auxiliary turbine. The impact of different designs on net power output, plant efficiency, and CO_2 emissions was analysed. The results indicated that extracting steam from the auxiliary turbine showed a minimum efficiency penalty of 9.75%.

Additionally, to reduce the heat duty for solvent regeneration, different configurations were modelled and simulated. Amrollahi et al. (2012) simulated an NGCC power plant integrated with MEA-based PCC in Aspen Plus®. Additionally, different configurations, including absorber intercooling (AIC), rich solvent split-flow (RSS), and lean vapour recompression (LVR), were simulated. Le Moullec et al. (2014) simulated PCC process using 30wt% MEA in Aspen Plus®. It evaluated process configurations, including rich solvent recycles (RSR), rich solvent preheating (RSP), inter-heated strippers (IHS) and multi-pressure strippers (MPS). To better utilise the heat, the combination of more than two configurations was investigated, for example, AIC-RSS, LVR-RSS and MPS-RSS (Amrollahi et al., 2012; Le Moullec and Kanniche, 2011). From the results, using optimised configurations can decrease the energy penalty by up to 37.2%.

The model of PCC process using different solvents was also developed. Zhang et al. (2017) developed a rate-based steady-state model for PCC process using a 28 wt% AMP and 17 wt% PZ blend solvent, implemented in Aspen Plus®. The model was validated against pilot plant data from Mangalapally and Hasse (2011b). The sensitivity analysis was carried out to

investigate the impact of key factors on the reboiler duty, including CO_2 capture rate, solvent concentration, liquid-to-gas (L/G) ratio, and stripper pressure. Borhani et al. (2022) developed a rate-based non-equilibrium model to simulate CO_2 absorption using PZ and K_2CO_3 solvent in the packed column using MATLAB®. The model incorporated mass and heat transfer, chemical reactions, and phase equilibria, assuming chemical equilibrium in the liquid phase bulk and physical equilibrium at the gas-liquid interface. Thermodynamic properties were calculated using the Extended-UNIQUAC model for the liquid phase and the Soave-Redlich-Kwong equation of state (EoS) for the gas phase. The study showed the good absorption performance of the PZ-K_2CO_3 solvent.

2.6 Analysis and optimisation studies on CCS and BECCS

2.6.1 Energy, exergy and economic analysis

PCC is a highly energy-consuming process. Integrating PCC into power plants would cause high energy and efficiency penalties. Therefore, energy analysis is carried out to investigate its impact on the power plant's energy performance. Additionally, to implement PCC at a large scale, it is essential to evaluate its cost-effectiveness. Otitoju et al. (2021) simulated and validated the pilot-scale PZ-based PCC process in Aspen Plus®. Subsequently, the scale-up of the pilot-scale model was conducted to process the flue gas from a 250 MWe NGCC power plant. The energy analysis was carried out to compare the large-scale models with different configurations (standard, AIC, and AFS) and different PZ concentrations (30, 35, and 40wt%). Additionally, APEA® was used to evaluate the costs of these processes. The results showed that a 40wt% PZ solvent offered better CO_2 absorption efficiency and lower energy demand. Furthermore, using the AFS configuration showed a superior performance in reducing the energy and cost requirements.

Ma et al. (2024) simulated PCC process using 40wt% PZ for capturing CO_2 from a large-scale ethylene plant with 60kton CO_2 emissions annually. The study modelled different configurations, including standard PCC, flue gas heat recovery (FHR), AIC, and AFS using Aspen Plus®. The energy and economic analysis were conducted. Consequently, compared with MEA, PZ can reduce energy use by 22.95% and capture costs by 27.93%. Integrating FHR, AIC and AFS achieved the best results, with energy consumption of 2.28 GJ/ton CO_2 (37.71% reduction)

and a capture cost of 47.27$/ton (36.76% reduction).

Exergy refers to the maximum useful work a system can deliver when it undergoes a reversible process to achieve thermodynamic equilibrium with its environment. Exergy analysis, based on the second law of thermodynamics, is a method used to identify and quantify the sources and types of thermodynamic losses within a system by computing the exergy destruction of each component (Zang et al., 2018). It provides insights into inefficiency and offers recommendations for optimising the system's thermodynamic performance. Lak Kamari et al. (2023) developed a model of a biomass-assisted multigeneration system integrating a biomass combustor, Rankine cycle, ammonia-water absorption refrigeration system and biofuel production unit using Aspen Plus®. Fifteen biomass feedstocks were evaluated. The results of exergy analysis showed that the biomass burner was the largest source of exergy destruction (up to 52.8%) due to combustion irreversibility. The energy efficiencies of the system varied from 62.72% (rice husk) to 68.30% (rice straw), while the exergy efficiencies ranged from 42.86% (larch wood) to 45.29% (rice straw).

Advanced exergy analysis considers the interactions between system components and assesses the possibilities of lowering exergy destruction across individual components and the entire system. It categorises exergy destruction into endogenous/exogenous sources and avoidable/unavoidable portions. Olaleye and Wang (2017) modelled a 580 MW supercritical CFPP integrated with MEA-based PCC through Aspen Plus®. The advanced exergy analysis was conducted. The results showed that 30% of the system’s exergy destruction is avoidable, with most avoidable losses in each component being endogenous. This indicates that optimising the components themselves could significantly reduce system exergy destruction. Hence, seven configurations were evaluated, and the configuration using AIC and LVR showed the best performance, lowering the energy consumption by 7% compared to the standard PCC.

2.6.2 Process optimisation

Hosseini-Ardali et al. (2020) developed a model of rate-based PCC process using PZ and MDEA blended solvent in Aspen HYSYS®. The multi-objective optimisation was carried out based on the non-dominated sorting genetic algorithm (NSGA-II) method. The program is written in MATLAB code and linked to Aspen HYSYS® to optimise the key variables for the objective

functions. The objectives are maximising CO_2 capture and minimising reboiler duty with the constraints of solvent (PZ/MDEA) concentration at 30 and 40wt%. The decision variables include solvent flow rate, PZ concentration and MDEA concentration. The optimisation results showed that reboiler heat duties were 2.69–2.82 GJ/t_{CO2} corresponding to the CO_2 capture level of 90–94%. This indicated a 19–23% energy saving compared to MEA-based PCC.

Luo and Wang (2016) developed a steady-state model of an NGCC power plant integrated with a PCC process using MEA solvent in Aspen Plus®. The optimisation process aimed to minimise the LCOE as the objective function by adjusting operational variables, including lean loading and CO_2 capture level. The process was subject to equality and inequality constraints. The equality constraints include the mass and energy balances calculated by the steady-state model. The inequality constraints involve the reboiler duty, column flooding capacity, capture level, lean loading, L/G ratio and solvent concentration limits. Additionally, sensitivity analysis was conducted to assess the impact of external factors such as carbon pricing, natural gas prices, and CO_2 transport and storage costs on LCOE. As a result, the optimal lean solvent loading was found to range between 0.26 and 0.30 mol CO_2/mol MEA, depending on the desired capture level, with higher lean loading associated with improved energy efficiency.

2.6.3 Life cycle assessment

LCA is a method used to evaluate the comprehensive environmental impacts of a product, process or system across its entire life cycle systematically. It quantifies all the interactions between the product and the environment, including inputs such as resources, energy, materials, and land use and outputs like emissions to air, water, and soil (JRCEC, 2012). The environmental impacts are categorised into climate change, land use, acidification, ecotoxicity, etc. These impacts can be presented individually for each category or combined into a single indicator by applying weighting factors, as indicated in Figure 2.8.

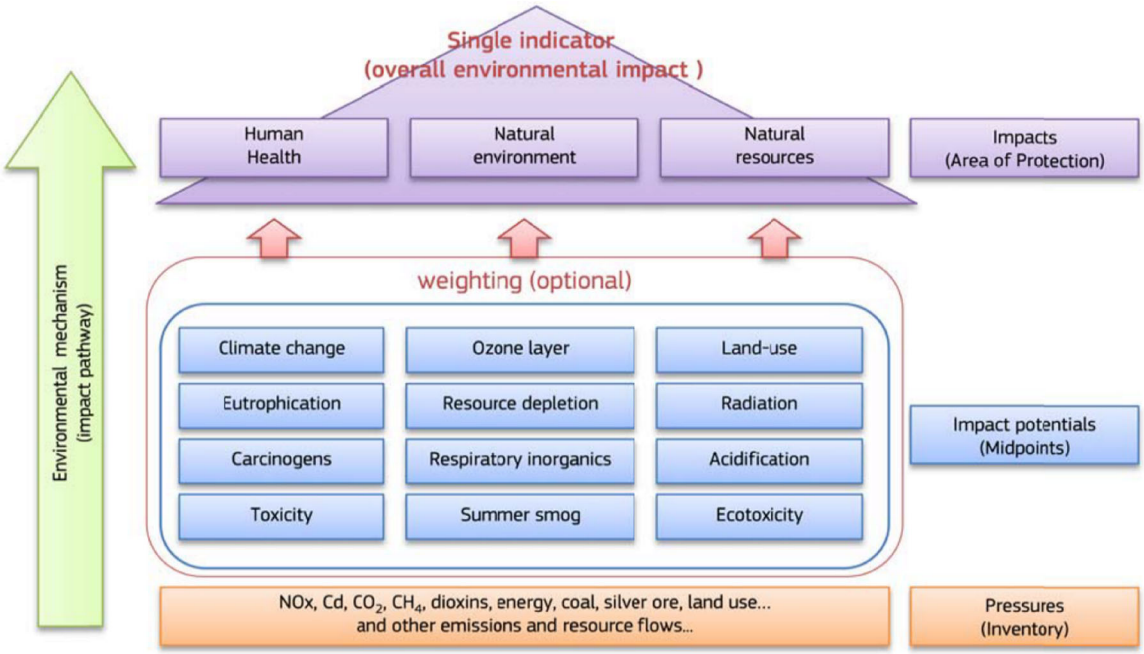

Figure 2.8 Environmental impact categories for LCA (JRCEC, 2012)

Terlouw et al. (2021) proposed additional recommendations for LCA of carbon dioxide removal technologies based on general ISO guidelines, as presented in Figure 2.9. When evaluating the CO_2 removal potential of the system, the functional unit per tonne of CO_2 removed was suggested to use. Moreover, the cradle-to-grave approach is suggested when determining the system boundaries. Additionally, it is necessary to distinguish between avoided emissions (reductions relative to a baseline) and negative emissions (permanent CO_2 removal from the atmosphere). In addition, the side effects within the system boundaries, such as water, energy, and food security interdependencies, should also be considered.

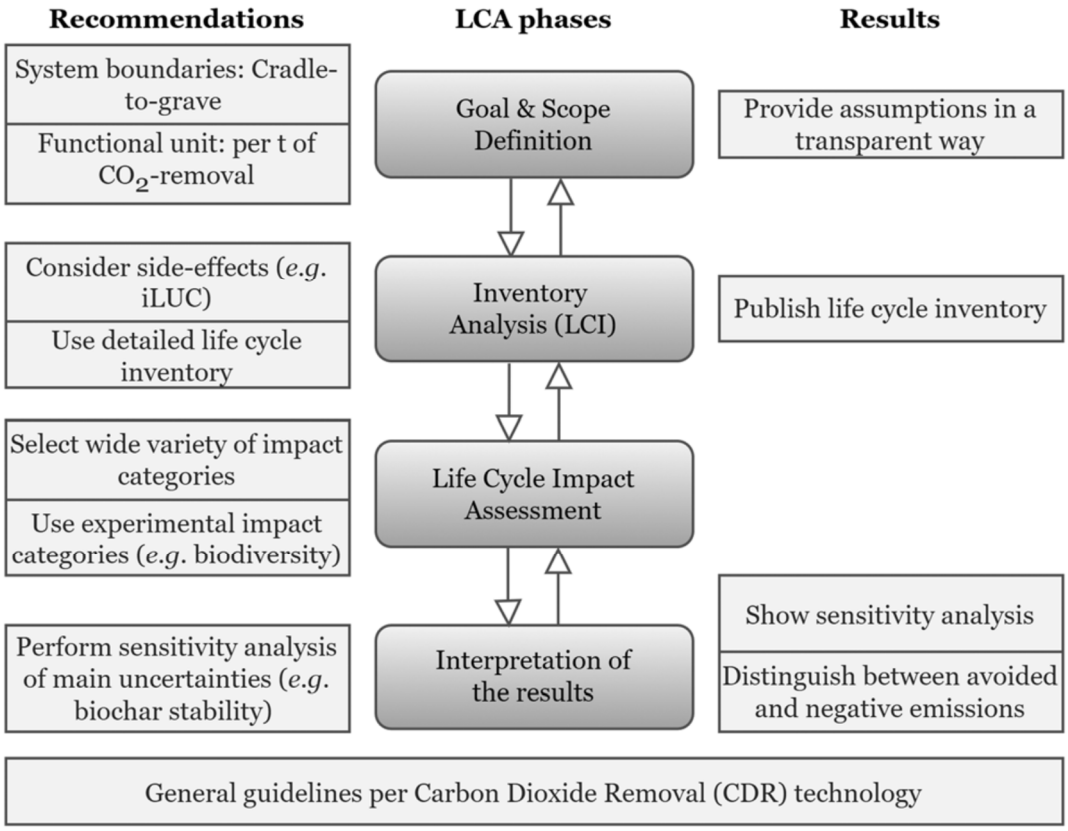

Figure 2.9 Recommendations for LCA on carbon dioxide removal technologies based on the ISO guidelines (Terlouw et al., 2021)

BECCS is a negative emission process, and LCA is an essential approach to assessing its carbon removal potential. Schakel et al. (2014) conducted LCA of biomass co-firing CFPP and IGCC plants with carbon capture using the SimaPro®. The ReCiPe Midpoint methodology and Ecoinvent database were applied to predict the environmental impacts. The analysis involves upstream (biomass production, transportation), operational (power generation, CO_2 capture), and downstream (CO_2 transport and storage) stages. The key parameters, including power plant efficiency, CO_2 emissions, water consumption and the environmental impacts of pollutant emissions (e.g., SO_2, NOx, and Hg), were assessed. The results demonstrated that 30% biomass-cofiring and CCS can result in net negative CO_2 emissions of 67–85 g/kWh. The sensitivity analysis indicated that the parameters that determine the fuel required strongly influence the environmental performance, such as plant efficiency and land use allocation.

García-Freites et al. (2021) developed the models of three processes using Aspen Plus®, including sawmill residues-fired power plants with CCS (440 MWe), Miscanthus-fired CHP with

CCS (20MW_e and 70MW_{th}) and Willow-based BIGCC with CCS (232MWe). LCA was carried out to analyse the GHG removal potential of different BECCS processes in terms of net negative CO_2 emissions per unit of power output, biomass and land area required to meet the UK GHG removal target. As a result, the Miscanthus-CHP showed the highest net-negative CO_2 emissions at 1131 kg CO_2/MWh, but it required the most biomass (0.98 t/MWh) and land area (819 m²/MWh). Willow-BIGCC had lower net-negative CO_2 emissions (693 kg CO_2/MWh), but it also had lower biomass requirements (0.54 t/MWh) and lower land use (595 m²/MWh). In the sawmill residues case, with the lowest net-negative CO_2 emissions (647 kgCO2/MWh), the advantage is lower resource requirements, needing only 0.74 t/MWh of biomass and 431 m²/MWh of land.

2.7 Summary

From the comprehensive literature review on biomass power generation and solvent-based PCC technologies, the findings are as follows:

- BFPP is a promising power generation technology that can reduce CO_2 emissions from power stations. Many coal-fired or biomass and coal co-firing plants, such as the DRAX in the UK and Avedøre in Denmark, have been converted to biomass-only power plants with the support of government policies and incentives in the European countries. Furthermore, BFPP integrated with PCC is a negative emission process.
- Although implemented commercially in some countries, the high energy and investment demands are the main limitations for widely applying PCC at a large scale. Research on PZ has demonstrated its advantages compared to MEA, including higher CO_2 absorption capacity and better thermal and oxidative stability, resulting in reduced energy consumption. And no reported work on BFPP integrated with PZ-based PCC was found.
- Energy consumption and total costs (which include both capital and operating expenses) are two key indicators for the effective application of the PCC process on a large scale. Comprehensive techno-economic analyses for PZ-based PCC with different configurations for BFPP at a large scale, are lacking.
- Previous studies have identified solvent concentration as an important factor influencing the energy and economic performance of the PCC process. There is a lack

of focused research on optimising PZ concentration to decrease CO_2 capture costs.

- Existing research on improving the thermodynamic performance of BECCS systems has primarily focused on different biomass feedstocks and power generation methods. The exergy analysis of BFPP integrated with different PCC processes was not performed.
- LCA is critical for evaluating the environmental impact of CO_2 removal technologies. Existing LCA studies for power plants integrated with solvent-based PCC often use MEA as the solvent. However, it lacks an analysis of the environmental performance of BFPP integrated with optimised PCC processes using other solvents.

Chapter 3 Model development and validation of BFPP and solvent-based PCC at large scale

3.1 Overview

This chapter describes the model development and validation of the BFPP and PCC processes. In Section 3.2, the steady-state modelling of a 550 MWe supercritical BFPP was carried out in Aspen Plus® V11. The simulation results were compared with the NETL (2012) report. In Section 3.3, the pilot-scale models of MEA and PZ-based PCC processes were developed in Aspen Plus® at a steady state. The MEA-based model was validated using the experimental data of Notz et al. (2012). For the PZ-based model, the absorber and stripper were validated using Plaza and Rochelle (2011) and Van Wagener (2011), respectively. The pilot-scale PCC models were then scaled up to absorb the CO_2 of the flue gas from the 550 MWe BFPP. In Section 3.4, different configurations of the solvent-based PCC process were simulated using Aspen Plus®. The findings of this chapter are provided in Section 3.5.

3.2 Model development and comparison of BFPP

3.2.1 Model development of BFPP

The steady-state model of a 550 MWe supercritical BFPP is developed using Aspen Plus® V11 based on the NETL (2012) report. The process flowsheet of the biomass power plant is shown in Figure 3.1.

The primary air is injected into the furnace through the primary air (PA) fans. It is used to carry the biomass pellets to the combustion area and partially dry the fuel. The secondary air, after being preheated by the recovery heat from the flue gas, is fed to the furnace through the forced draft (FD) fan to provide the air for combustion. The combustion occurring in the furnace will provide heat for converting the preheated feedwater to the superheated steam (24.1 MPa/ 593 ^{o}C). This main steam will be fed to the steam turbine for power generation. To increase the turbine efficiency, the steam from the HP turbine will be reheated to 593 ^{o}C by the reheater and sent back to the IP turbine. After expansion in the turbine units, the last-stage steam will be condensed by the condenser and then preheated by the feedwater system. At the same time, the flue gas generated after combustion will go through the Selective

Catalytic Reduction (SCR) reactor, baghouse, and Flue Gas Desulfurization (FGD) system to NO_X, fly ash and SO_X, respectively, known as the pollution control system. After passing through the pollution control system, the flue gas will be emitted into the atmosphere through the stack. The details of the modelling of each subsystem are shown in Section 3.2.1.1 to Section 3.2.1.3.

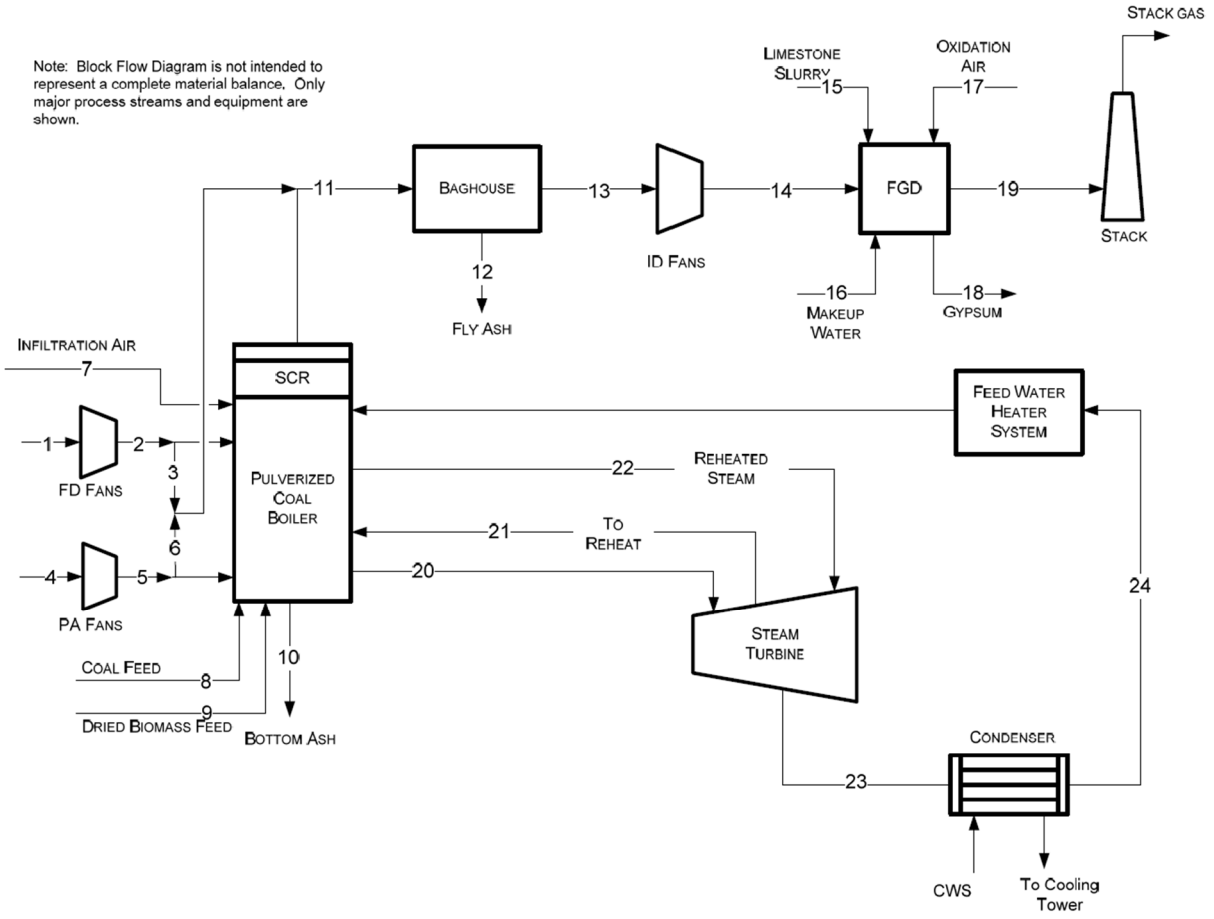

Figure 3.1 The process flowsheet diagram of a 550 MWe BFPP (NETL, 2012)

3.2.1.1 Simulation of the boiler subsystem

The steady-state model of a supercritical once-through boiler is developed in Aspen Plus® (Figure 3.2). In the boiler model, the physical property is predicted using Peng-Robinson with Boston-Mathias modifications (PR-BM). Compared with the original Peng-Robinson EoS, PR-BM performs better in predicting vapour-liquid equilibrium in mixtures and non-ideal systems (Boston et al., 1980). It is widely used for the simulation and optimisation of industries like oil and gas, chemical processing, and power generation.

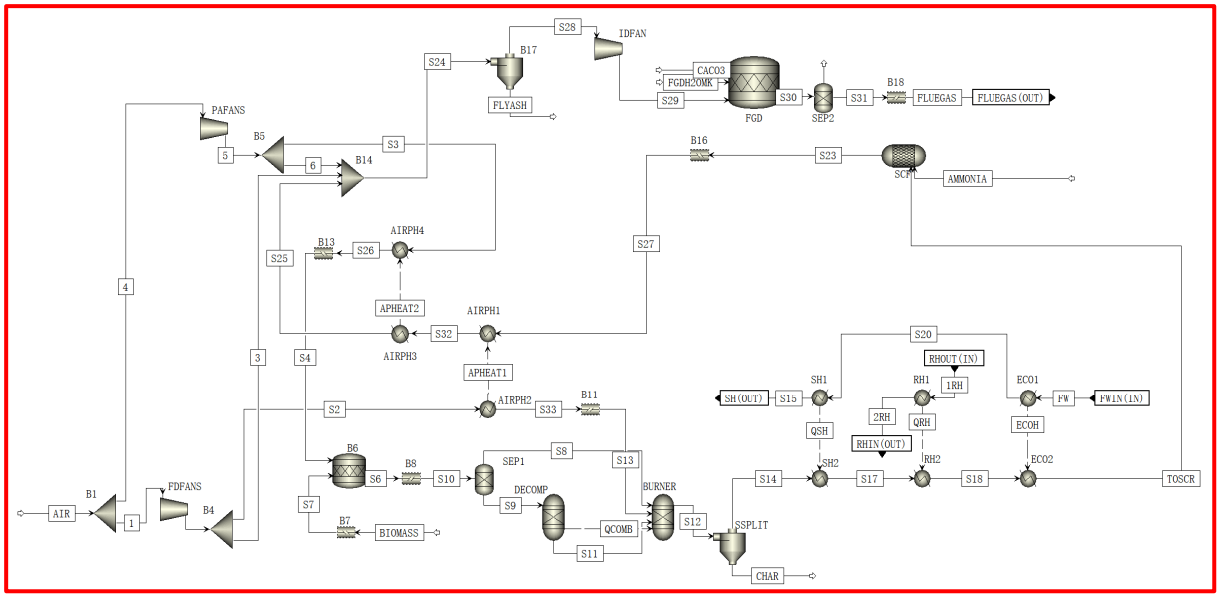

Figure 3.2 The flowsheet of the boiler of a 550 MWe BFPP in Aspen Plus®

This work uses hybrid poplar as the biomass feedstock. It is adaptable and grows rapidly. Moreover, hybrid poplar is not a food source, so using it as fuel can avoid competition with food markets (NETL, 2012). Table 3.1 and Table 3.2 provide the ultimate proximate analysis of hybrid poplar as received and on a dry basis. The biomass and ash are defined as the non-conventional components, and their enthalpy and density are predicted by the HCOALGEN and DCOALIGT models (Aspen, 2009).

Table 3.1 Ultimate analysis of hybrid poplar (NETL, 2012)

Contents	As received	Dry basis
Carbon (wt %)	26.18	52.36
Hydrogen (wt %)	2.80	5.60
Oxygen (wt %)	20.08	40.16
Nitrogen (wt %)	0.19	0.37
Sulfur (wt %)	0.02	0.03
Chlorine (wt%)	0.00	0.00
Ash (wt %)	0.74	1.48
Moisture (wt %)	50.00	0.00
Higher heating value (HHV) (kJ/kg)	9813	19627

Lower heating value (LHV) (kJ/kg)	9232	18464

Table 3.2 Proximate analysis of hybrid poplar (BFL, 2013; NETL, 2012)

Contents	As received	Dry basis
Moisture (wt %)	50.00	0.00
Ash (wt %)	0.74	1.48
Volatile (wt %)	42.94	85.87
Fixed Carbon (wt %)	6.33	12.65

As shown in Figure 3.2, the model is divided into various components, including a PA fan, FD fan, air-preheater, decomposer, combustor, superheater, reheater, economiser, induced draft (ID) fans, pollution control system, and auxiliary equipment. The inlet stream information is summarised in Table 3.3.

Table 3.3 Inlet stream information (NETL, 2012)

Parameters	Value
Biomass mass flow rate (t/h)	313.4
Inlet air mass flow rate (t/h)	1987.2
Infiltration air mass flow rate (t/h)	35.0
Inlet air temperature (°C)	15
Air composition (mole fraction)	
Ar	0.92%
CO_2	0.03%
H_2O	0.99%
N_2	77.32%
O_2	20.74%

The primary and secondary air is fed using a PA fan and an FD fan, respectively. The air is preheated using the recovered heat from the combustion flue gas in the air preheater. An overall 15% excess air is supplied to the boiler, including 2% infiltration air (NETL, 2012). Then, the decomposer breaks down the fuel components, feeding into the combustion chamber.

The combustor is modelled using RGibbs, which is calculated based on minimising Gibbs free energy to achieve chemical equilibrium. Since Aspen Plus® is unable to estimate the Gibbs free energy of a non-conventional component, the biomass feedstock needs to be decomposed before entering the combustor. In the SCR reactor, ammonia is injected and mixed with a flue gas flow at a temperature of 300–400°C. The NO_X removal efficiency is assumed to be 86% (NETL, 2012). The main reactions in the SCR reactors are (He et al., 2017):

$$4NO + 4NH_3 + O_2 \rightarrow 4N_2 + 6H_2O \quad \text{(R 3.1)}$$

$$6NO_2 + 8NH_3 \rightarrow 7N_2 + 12H_2O \quad \text{(R 3.2)}$$

The limestone wet scrubber is used to remove SO_2 with an efficiency of 98%. The limestone, air and make-up water are supplied to the FGD scrubber and generate calcium sulphate ($CaSO_4 \cdot 2H_2O$), also known as gypsum. The reaction is as follows (Córdoba, 2015):

$$CaCO_3 + SO_2 + 2H_2O \rightarrow CaCO_3 \cdot 2H_2O + CO_2 \quad \text{(R 3.3)}$$

$$CaSO_3 \cdot 2H_2O + \frac{1}{2}O_2 \rightarrow CaSO_4 \cdot 2H_2O \quad \text{(R 3.4)}$$

Additionally, the fabric filter is utilised for fly ash removal with an efficiency of 99.8%.

3.2.1.2 Simulation of the turbine subsystem

The thermodynamic properties of the turbine subsystem are predicted using the IAPWS-95 formulation. It mainly consists of the high-pressure (HP) turbine, the IP turbine, the LP pressure, the boiler feed pump turbine (FPUMPTB), the condenser and the condenser pump. In the turbine system, the superheated steam from the boiler is first fed to the HP turbine. Subsequently, outlet steam from the HP turbine is partially sent to the reheater at 593°C. The reheated steam is then sent to the IP turbine together with the remaining steam from the HP turbine. This steam drives the IP and LP turbines for power output. Furthermore, a boiler feed pump turbine is utilised to supply power for the feedwater pumps. The outlet steam from the turbine units is mixed with the makeup water, condensed in the condenser and finally sent to the feedwater heating system. Moreover, a part of the hot steam in the turbines is extracted to provide heat for the feedwater heaters, which will be introduced in Section 3.2.1.3. As shown in Figure 3.3, this model applied turbine trains—such as HP1 and HP2 for the HP

turbine, IP1 and IP2 for the IP turbine, and LP1 to LP5 for the LP turbine—to simulate the steam extraction process within the regenerative cycle. The key thermodynamic parameters used for steam cycle modelling, including pressures and temperatures at various turbine stages, are summarised in Table 3.4.

Table 3.4 Key thermodynamic parameters for steam cycle modelling (NETL, 2012)

Stream	Pressure (MPa)	Temperature (°C)
Main steam from boiler	24.23	593
HP extraction steam to FWHX7	4.75	351
HP extraction steam to FWHX8	7.48	411
HP turbine outlet to RH	4.9	354
Reheated steam inlet to IP	4.52	593
IP extraction steam to FWHX6	2.07	476
IP extraction steam to deaerator	0.92	369
IP turbine outlet	0.93	364
LP turbine inlet	0.93	364
LP extraction steam to FWHX4	0.48	285
LP extraction steam to FWHX3	0.13	145
LP extraction steam to FWHX2	0.06	98
LP extraction steam to FWHX4	0.02	64
LP turbine outlet (to condenser)	0.93	475

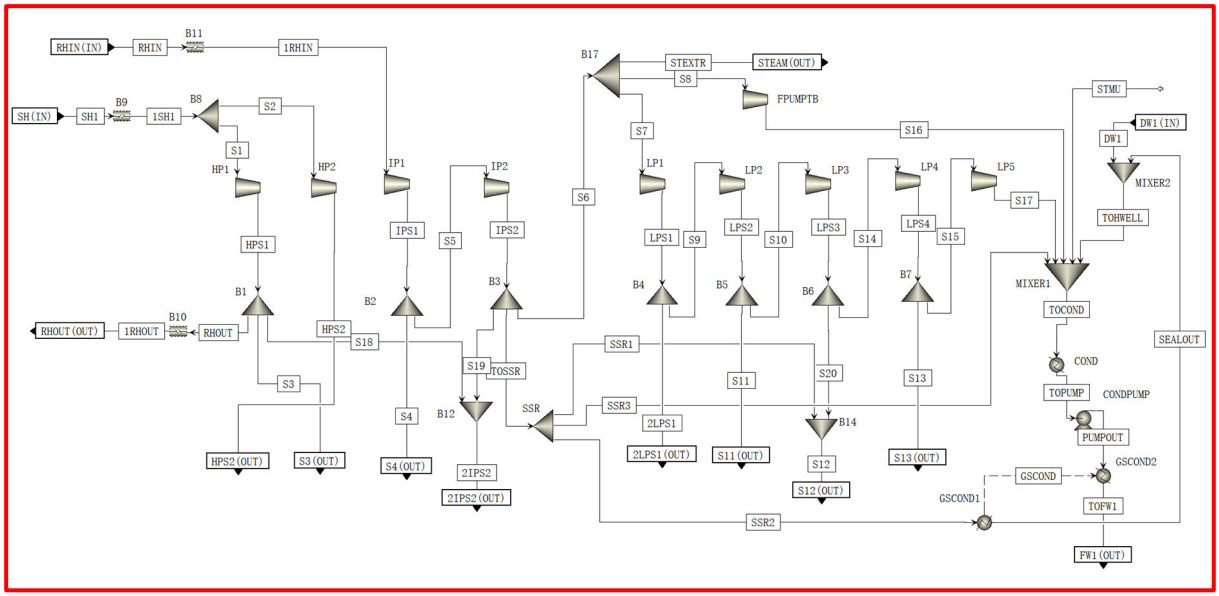

Figure 3.3 The flowsheet of the turbine of a 550 MWe BFPP in Aspen Plus®

3.2.1.3 Simulation of the feedwater subsystem

The feedwater subsystem is also simulated based on the IAPWS-95 formulation. It consists of a series of heat exchangers: four high-pressure and four low-pressure closed feedwater heaters, along with one open feedwater heater (deaerator). As a part of the regenerative cycle, feedwater heaters were heated by steam extracted from the turbine to preheat feedwater, thus reducing the energy demand in the boiler. To present the heat transfer within the feedwater heater clearly, each stage of the closed feedwater heater was simulated using a drain water heat exchanger (DWHX) to condense the extracted hot steam to drain water and a feedwater heat exchanger (FWHX) to heat the feedwater using the heat provided by DWHX. After the feedwater heater train, the feedwater is preheated to 291.4°C. In this study, the deaerator was simplified and modelled as a heat exchanger, following the approach adopted by Olaleye (2015), to represent its primary thermal function—preheating feedwater through the condensation of extraction steam. The mass transfer associated with the removal of dissolved gases was not explicitly considered. Under this simplification, the system is assumed to operate at saturation conditions, corresponding to full removal of the gas. In this process reported by NETL (2012), the deaerator operates under near-saturation conditions, with steam extracted from the IP turbine at 0.4 MPa and 291 °C. Therefore, it is considered to have a negligible impact on the overall performance of the steam cycle.

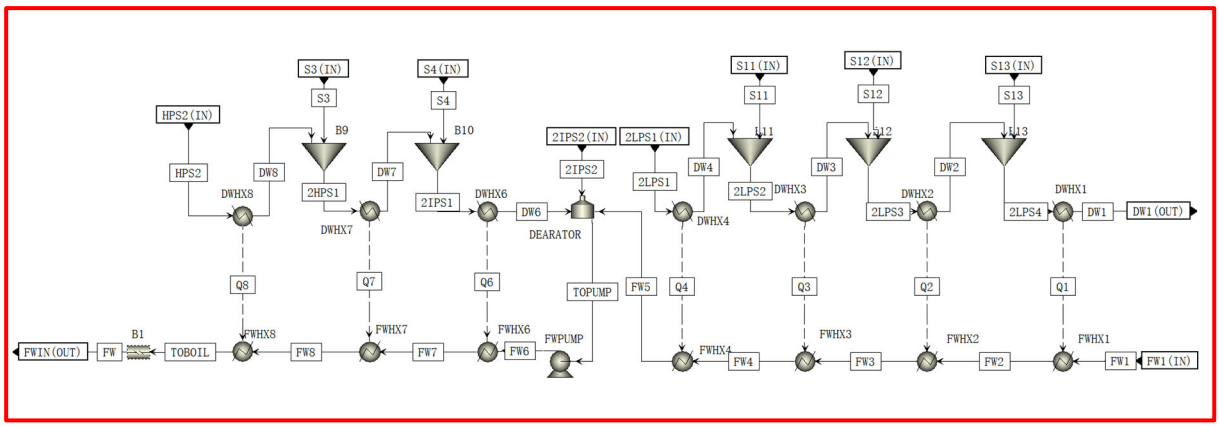

Figure 3.4 The flowsheet of the feedwater train of a 550 MWe BFPP in Aspen Plus®

3.2.2 Model comparison

In the model of BFPP, the boiler, turbine and feedwater subsystems were combined, as presented in

Figure 3.5 according to the process described in Section 3.2.1. Each subsystem was saved in the hierarchies.

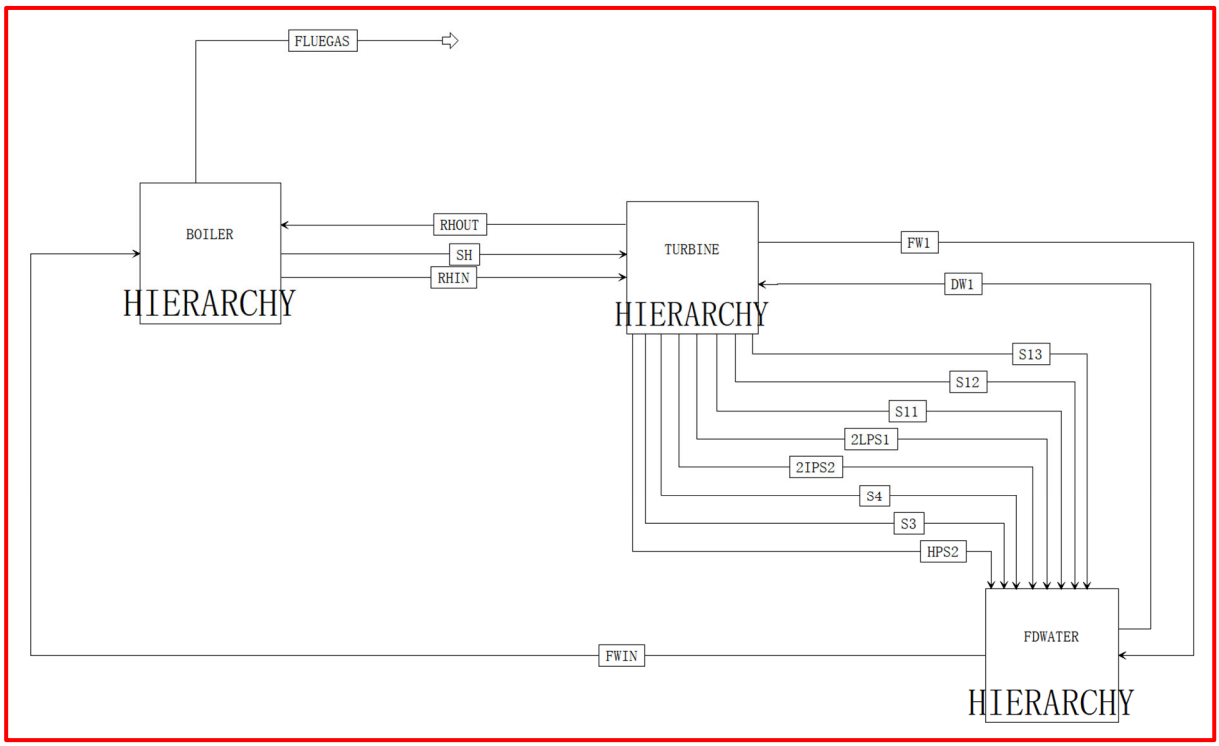

Figure 3.5 The model hierarchy showing the complete BFPP simulation in Aspen Plus®

The model was validated based on the data of the 550 MWe supercritical BFPP reported by

NETL (2012). The key indicators of the power plant, including the power output and plant efficiency, were compared with the reference. Additionally, to prepare for the integration of the PCC process, the composition of the flue gas is also an important index to validate the accuracy of the model as presented in Table 3.5.

Moreover, the parameters (temperature, pressure and mass flow rate) of the main streams were compared with the NETL (2012) report (Table 3.6). The main streams include the outlet stream of the superheater (SH), the inlet (RHIN) and outlet stream (RHOUT) of the reheater, the flue gas from the boiler (FLUEGAS), the stream from the condenser to the feedwater heater train (FW1) and the stream from the feedwater heater train to the boiler (FWIN).

Table 3.5 Model comparison of performance indicators of the BFPP against NETL (2012)

Performance parameters	NETL (2012)	Simulation	Relative error
Gross plant power output (MWe)	616.0	615.6	0.06%
Auxiliary power (MWe)	66.0	64.8	1.77%
Net plant power output (MWe)	550.0	550.8	0.14%
Net plant efficiency (%)	35.8%	34.9%	2.42%
Flue gas mole fraction (mol%)			
Ar	0.82	0.81	1.81%
CO_2	15.53	15.61	0.54%
H_2O	12.94	13.24	2.35%
N_2	68.36	67.95	0.60%
O_2	2.34	2.39	2.17%

From the model comparison results shown in Table 3.5, the gross and net plant power output and net plant efficiency had small relative errors of 0.06%, 0.14% and 2.42%, respectively. Flue gas composition, which is a vital factor for PCC integration, showed relative errors within 5% across all components. Additionally, as illustrated in Table 3.6. The mainstream parameters (temperature, pressure, and mass flow rate) also showed good agreement with the reference data, with all relative errors within 5%. The results of the model comparison confirmed that this model can provide a good prediction for simulating the performance of the BFPP.

Table 3.6 Results of model comparison on the main streams of BFPP

	Temperature (°C)			Pressure (MPa)			Mass flow (t/hr)		
	Ref.	**Sim.**	**Rel. error**	**Ref.**	**Sim.**	**Rel. error**	**Ref.**	**Sim.**	**Rel. error**
SH	593.0	593.33	0.06%	24.2	24.23	0.01%	1766.1	1766.14	0.002%
RHOUT	354.0	353.35	0.18%	4.9	4.90	0.02%	1465.0	1464.98	0.001%
RHIN	593.0	593.33	0.06%	4.5	4.52	0.03%	1465.0	1464.98	0.001%
FW1	39.0	38.64	0.93%	1.7	1.69	0.05%	1336.0	1336.03	0.002%
FWIN	291.4	290.57	0.29%	28.8	28.85	0.19%	1766.1	1766.14	0.002%
FLUE GAS	176.0	176.00	0.00%	0.1	0.102	2.04%	2331.4	2311.80	0.841%

3.3 Model development, validation and scale-up of MEA and PZ-based PCC

3.3.1 Model development of solvent-based PCC process using MEA and PZ

The rate-based models of MEA and PZ-based PCC were developed at steady state using Aspen Plus® V11. In this work, both the absorber and the stripper columns were modelled using the Radfrac block in Aspen Plus®. Radfrac allows column simulations using either the equilibrium stage approach or the rate-based approach. The equilibrium stage method assumes that the vapour and liquid on each theoretical stage are well mixed and in thermodynamic equilibrium. This simplifies calculations, but it does not reflect the actual mass transfer in real systems. According to Lawal et al. (2009), the rate-based method can provide more accurate predictions for the simulation of the CO_2 absorption process using MEA than the equilibrium method. It assumes equilibrium only at the vapour–liquid interface and takes the film reaction and reaction kinetics into consideration when calculating the mass transfer rate between gas and liquid phases.

The flowsheet of the standard PCC models using MEA and PZ is presented in Figure 3.6.

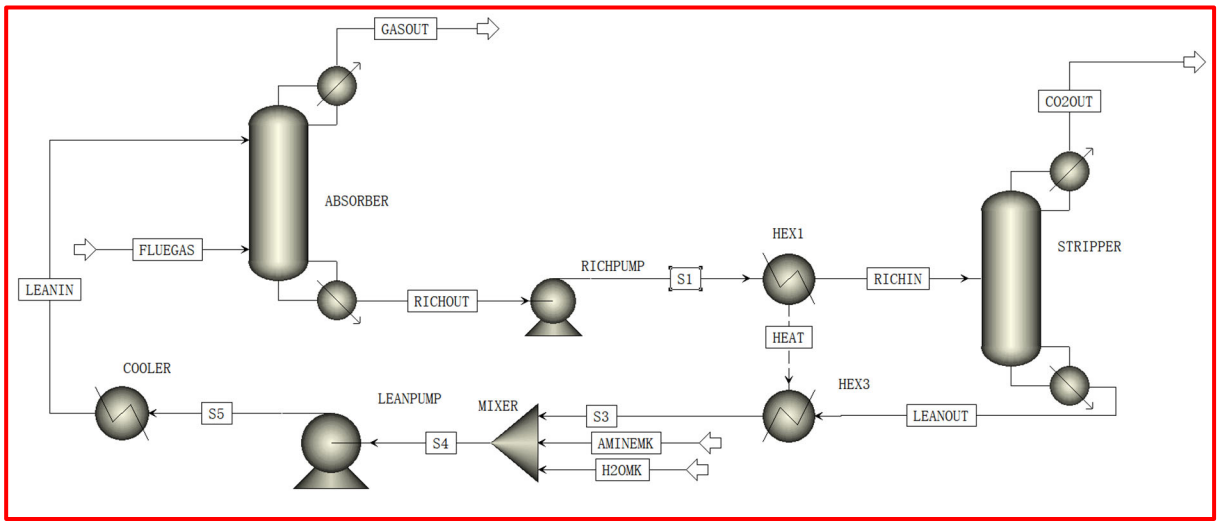

Figure 3.6 The flowsheet of the standard PCC process in Aspen Plus®

The liquid phase properties were computed by the Electrolyte Non-Random Two-Liquid (ELECNRTL) method, while the vapour phase properties were determined through the Redlich-Kwong (RK) EoS, as described by Soave (1972):

$$p = \frac{RT}{v - b} - \frac{a/T^{0.5}}{v(v + b)} \quad (3.1)$$

Where p is the pressure of the gas (Pa), T is the absolute temperature of the gas (K), v is the molar volume (m^3/mol), R is the universal gas constant (8.314 J/mol·K), a is an attraction parameter related to intermolecular forces and b is a repulsion parameter related to finite molecular size.

The RK EoS was selected in Aspen Plus® to estimate vapour-phase properties due to its simplicity and satisfactory performance in gas-phase systems involving non-polar and slightly polar species (Horvath, 1974).Li and Yan (2009) reported that RK EoS can provide satisfactory results for the pure CO_2 system at low pressures. The RK EoS has been widely applied in PCC modelling with MEA and PZ solvents, as demonstrated in studies by Lawal et al. (2009) and Otitoju et al. (2021).

The CO_2 absorption process using amine-based solvents involves both equilibrium and kinetic reactions. The temperature-dependent equilibrium constants (K_{eq}) were determined using the following formula:

$$\ln K_{eq} = A + \frac{B}{T} + C\ln T + DT \quad (3.2)$$

The equilibrium reactions of CO_2 absorption using MEA are detailed:

$$2H_2O \leftrightarrow H_3O^+ + OH^- \quad (R\ 3.5)$$

$$CO_2 + 2H_2O \leftrightarrow HCO_3^- + H_3O^+ \quad (R\ 3.6)$$

$$HCO_3^- + H_2O \leftrightarrow CO_3^{2-} + H_3O^+ \quad (R\ 3.7)$$

$$MEAH^+ + H_2O \leftrightarrow MEA + H_3O^+ \quad (R\ 3.8)$$

$$MEACOO^- + H_2O \leftrightarrow MEA + HCO_3^- \quad (R\ 3.9)$$

For the MEA-based CO_2 absorption process, the coefficients for computing the K_{eq} for reactions (R 3.5) - (3.7) were sourced from Posey and Rochelle (1997). The coefficients for reactions (R 3.8) and (3.9) were derived from the work of Austgen et al. (1989).

The equilibrium reactions of CO_2 absorption using PZ are as follows:

$$2H_2O \leftrightarrow H_3O^+ + OH^- \quad \text{(R 3.10)}$$

$$CO_2 + 2H_2O \leftrightarrow HCO_3^- + H_3O^+ \quad \text{(R 3.11)}$$

$$HCO_3^- + H_2O \leftrightarrow CO_3^{2-} + H_3O^+ \quad \text{(R 3.12)}$$

$$PZH^+ + H_2O \leftrightarrow PZ + H_3O^+ \quad \text{(R 3.13)}$$

$$PZ + HCO_3^- \leftrightarrow PZCOO^- + H_2O \quad \text{(R 3.14)}$$

$$HPZCOO + H_2O \leftrightarrow PZCOO^- + H_3O^+ \quad \text{(R 3.15)}$$

$$PZCOO^- + HCO_3^- \leftrightarrow PZ(COO^-)_2 + H_2O \quad \text{(R 3.16)}$$

For the PZ-based CO_2 absorption process, the coefficients for computing the K_{eq} for reactions (R 3.10) - (R 3.12) were found in Posey and Rochelle (1997). The coefficients for reaction (R 3.13) were derived from Hetzer et al. (1963), and the coefficients for reactions (R 3.14)-(R 3.16) were obtained from Ermatchkov et al. (2003).

The reaction kinetics were expressed using the following power law expressions (Aspentech, 2010a):

$$r = kT^n \exp\left(-\frac{E}{RT}\right) \prod_{i=1}^{n} C_i^{a_i} \quad (3.3)$$

Where r is the reaction rate, k is the pre-exponent factor, E is the activation energy, n is the number of substances in the reaction, C_i is the concentration of species i, a_i is the stoichiometric of species i. The values of k and E for the rate-controlled reactions for MEA and PZ for CO_2 capture are shown in Table 3.7 and Table 3.8.

Table 3.7 Kinetics for PCC process using MEA solvent

Kinetic reactions	k	E, kJ/mol	Reference
$CO_2 + OH^- \rightarrow HCO_3^-$	4.3e+13	55.4	Pinsent et al. (1956)
$HCO_3^- \rightarrow CO_2 + OH^-$	2.4e+17	123.2	Aspentech (2010a)
$MEA + CO_2 + H_2O \rightarrow MEACOO^- + H_3O^+$	9.8e+10	41.2	Hikita et al. (1977)
$MEACOO^- + H_3O^+ \rightarrow MEA + CO_2 + H_2O$	3.2e+19	65.5	Hikita et al. (1977)

Table 3.8 Kinetics for PCC process using PZ solvent

Kinetic reactions	k	E, kJ/mol	Reference
$OH^- + CO_2 \rightarrow HCO_3^-$	4.3e+13	55.4	Pinsent et al. (1956)
$HCO_3^- \rightarrow OH^- + CO_2$	2.4e+17	123.2	Aspentech (2010a)
$H_2O + PZ + CO_2 \rightarrow H_3O^+ + PZCOO^-$	4.1e+10	33.6	Bishnoi and Rochelle (2000, 2002)
$H_3O^+ + PZCOO^- \rightarrow PZ + H_2O + CO_2$	9.5e+20	64.2	Aspentech (2010b)
$PZCOO^- + H_2O + CO_2 \rightarrow H_3O^+ + PZ(COO^-)_2$	3.6e+10	33.6	Bishnoi and Rochelle (2000, 2002)
$PZ(COO^-)_2 + H_3O^+ \rightarrow PZCOO^- + H_2O + CO_2$	3.5e+20	75.1	Aspentech (2010b)

For the rate-based models using MEA and PZ, the liquid mixture density was estimated using the Rackett model (Rackett, 1970). In contrast, the vapour phase properties were calculated via the RK EoS (Soave, 1972). The Chapman-Enskog-Brokaw model (Bird et al., 2001) was utilised to obtain the vapour-phase viscosity, while the liquid mixture viscosity was determined using the Jones-Dole electrolyte model (Horvath, 1985). The diffusivity of CO_2 in the solvent was estimated using the Wilke-Chang model with Vignes correction (Wilke and Chang, 1955). Surface tension for the liquid phase was determined using the Hakim-Steinberg-Stiel model combined with the Onsager-Samaras electrolyte correction (Horvath, 1985). Additionally, the thermal conductivity for the vapour and liquid phases was evaluated using the Wassiljewa-Mason-Saxena model and the Riedel correction, respectively (Poling et al.,

2001).

The built-in correlations in Aspen Plus® were utilised to estimate the mass and heat transfer processes occurring in the packed columns. For predicting the mass transfer coefficients and interfacial area, the correlation developed by Bravo et al. (1985) was applied. In the rate-based model implemented for both the absorber and the stripper, the correlations developed by Bravo et al. (1985) were used to estimate the gas and liquid film mass transfer coefficients. According to Stringle (1987), Bravo et al. (1985) can accurately describe the mass transfer characteristics of structured packings. The Chilton-Colburn method was used to calculate the heat transfer coefficients (Chilton and Colburn, 1934). Moreover, Bravo et al. (1992) correlations were used to compute the liquid holdup.

3.3.2 Validation of the PCC model at pilot scale using MEA and PZ

The pilot-scale PCC model using 30wt% MEA was validated using experimental data reported by Notz et al. (2012). Validation of the PZ-based PCC process model for the absorber and stripper was carried out using the experimental data from Plaza and Rochelle (2011) and Van Wagener (2011), respectively. Details of the packing specifications are provided in Table 3.9. The packing type of the absorber and stripper in the model is consistent with the experimental data. The packing information were obtained from Kister et al. (2019).

Table 3.9 Dimensions of absorber and stripper for the MEA and PZ cases

Experimental data	Notz et al. (2012)	Plaza and Rochelle (2011); Van Wagener (2011)
Solvent	MEA	PZ
Absorber diameter (m)	0.125	0.427
Stripper diameter (m)	0.125	0.427
Absorber packing height (m)	4.2	6.1
Stripper packing height (m)	2.52	6.1
Absorber packing type	Mellapak 250Y	Mellapak 2X
Stripper packing type	Mellapak 250Y	Mellapak 2X

The key parameters of the model were compared with the experimental data, such as the

carbon capture rate and the CO_2 loading. The carbon capture rate is calculated using the following equation:

$$\text{Carbon capture rate} = \frac{\text{CO}_{2\text{ in flue gas}} - \text{CO}_{2\text{ in outlet gas}}}{\text{CO}_{2\text{ in flue gas}}} \times 100\% \quad (3.4)$$

The CO_2 loadings in the MEA and PZ solvent are calculated using Eq. (3.5) and Eq. (3.6):

$$\text{CO}_2\text{ loading for MEA} = \frac{[\text{CO}_2] + [\text{HCO}_3^-] + [\text{CO}_3^{2-}] + [\text{MEACOO}^-]}{[\text{MEA}] + [\text{MEA}^+] + [\text{MEACOO}^-]} \quad (3.5)$$

$$C O_2\text{ loading for PZ} = \frac{[\text{CO}_2] + [\text{HCO}_3^-] + [\text{CO}_3^{2-}] + [\text{PZCOO}^-] + [\text{PZ(COO}^-)_2] + [\text{HPZCOO}]}{[\text{PZ}] + [\text{PZCOO}^-] + [\text{PZ(COO}^-)_2] + [\text{HPZCOO}] + [\text{PZH}^+]} \quad (3.6)$$

The relative errors between the experimental data and the simulation results are calculated using Eq. (3.7):

$$\text{Rel. error} = \frac{\text{Experimental data} - \text{Simulation results}}{\text{Experimental data}} \quad (3.7)$$

For the PCC model using 30wt% MEA, cases 2, 7, 8, 9, and 29 reported by Notz et al. (2012) were selected for model validation, all having the same CO_2 partial pressure of 0.11 bar. The experimental data is presented in Table 3.10. The validation results for the MEA-based models are illustrated in Figure 3.7 to Figure 3.10.

Table 3.10 Experimental data for validation of MEA-based PCC at pilot scale (Notz et al., 2012)

	Case 2	Case 7	Case 8	Case 9	Case 29
Flue gas temperature (°C)	48.15	47.98	48.13	47.88	47.45
Flue gas mass flow (kg/h)	72.4	72.1	72.3	72.3	76.0
CO_2 content of flue gas (wt%)	16.5	16.6	16.4	16.5	16.5
MEA concentration (wt%)	28.4	27.1	29.4	29.6	29.7
Lean temperature (°C)	40.21	39.96	40.06	40.03	41.46
Lean flow (kg/h)	200	200	200	200	200
Lean loading (mol_{CO2}/mol_{MEA})	0.308	0.356	0.228	0.147	0.306

Absorber pressure (bar)	0.983	0.987	0.985	0.984	0.987
Rich temperature (°C)	51.37	50.68	52.72	53.51	50.66
Rich flow (kg/h)	207.4	205.8	210.6	213.6	207.7
Stripper pressure (bar)	2.0	2.0	2.0	2.0	2.0
Reboiler duty (GJ/t_{CO2})	4.68	4.78	4.56	5.97	4.58
Reboiler temperature (°C)	119.11	115.55	122.66	124.03	119.66
Condenser temperature (°C)	19.42	20.69	17.15	19.05	15.79
CO_2 production (kg/h)	6.14	4.84	9.1	10.6	6.67

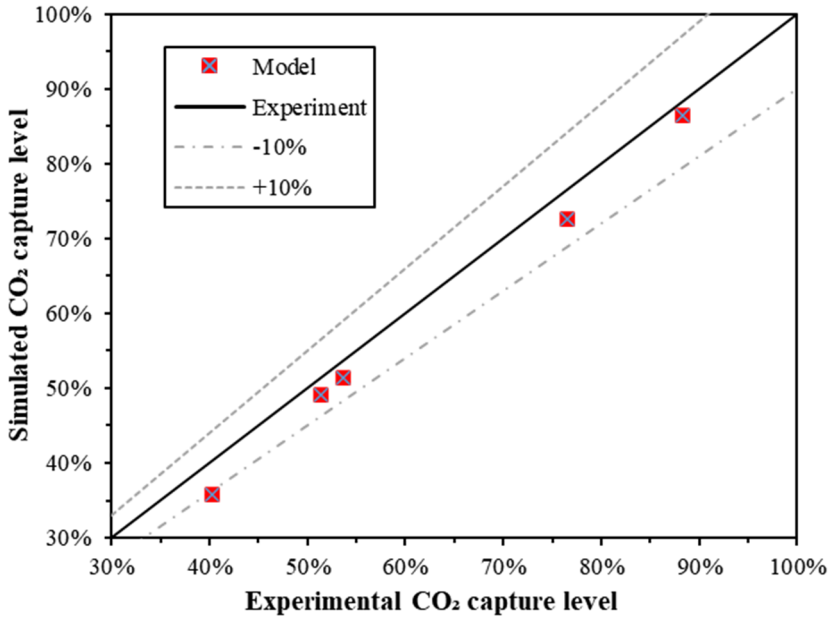

Figure 3.7 Validation results of carbon capture rate for standard PCC process using MEA

The CO_2 capture level is a key parameter to evaluate the CO_2 absorption ability of the process. As shown in Figure 3.7, the model showed a good agreement with the experimental data, especially at middle (50-60%) and high capture levels (80–90%). At a low capture level of 40%, the simulated points slightly underestimate the experimental results but still within the ±10% deviation boundaries.

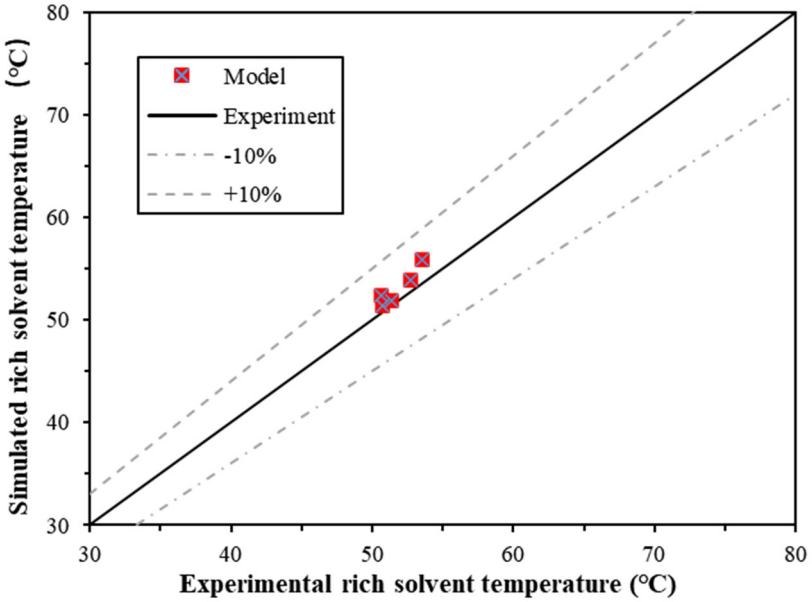

Figure 3.8 Validation results of rich solvent temperature for standard PCC process using MEA

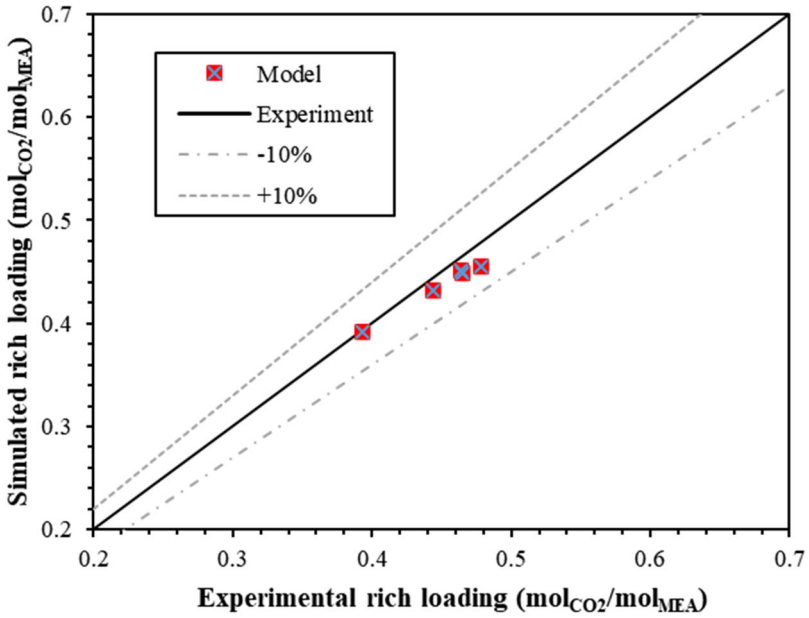

Figure 3.9 Validation results of rich loading for standard PCC process using MEA

The temperature and CO_2 loading of the rich solvent were validated against the experimental data (shown in Figure 3.8 and Figure 3.9). From the results, the simulation model performs accurate prediction for both rich solvent temperature and CO_2 loading predictions, with deviations within the ±10% limits.

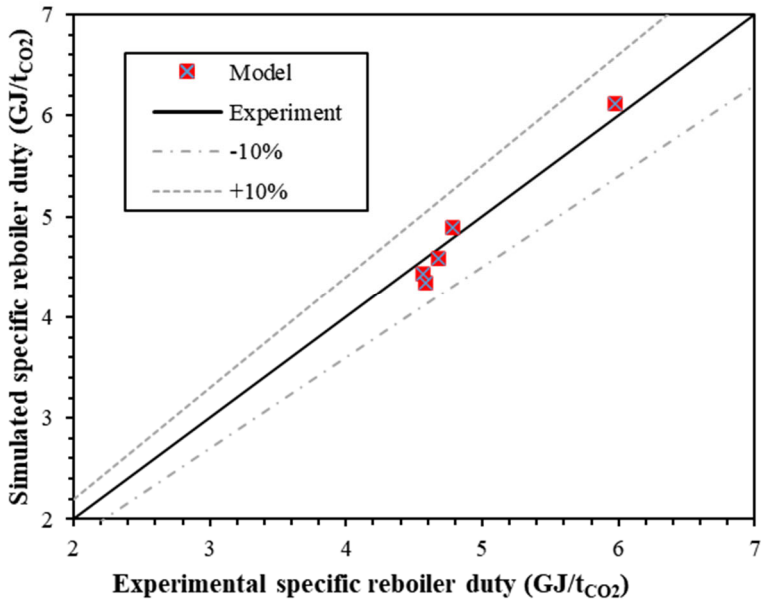

Figure 3.10 Validation results of specific reboiler duty for standard PCC process using MEA

The reboiler duty is the most important index to evaluate the energy performance of PCC. As illustrated in Figure 3.10, the simulation model demonstrates high accuracy in predicting specific reboiler duty, with deviations confined to a narrow ±10% range. These results confirm the reliability of the model for predicting the performance of PCC process using MEA.

The validation for the PZ-based model was carried out based on the data of cases 3, 5, 7, 9, and 13 from Plaza and Rochelle (2011) and Van Wagener (2011). The validation results are presented in Figure 3.11 to Figure 3.14.

Table 3.11 Experimental data for validation of PZ-based PCC at pilot scale (Plaza and Rochelle, 2011; Van Wagener, 2011)

	Case 3	Case 5	Case 7	Case 9	Case 13
Flue gas temperature (°C)	0	7	22	21	-9
Flue gas volume flow (m^3/s)	0.165	0.165	0.165	0.165	0.165
CO_2 content of flue gas (mol%)	12	12	12	12	12
PZ concentration (wt%)	43.87	39.97	40.69	40.06	29.44
Lean temperature (°C)	49.5	44.1	48.2	51.7	46.5
Lean flow (kg/h)	3780	3024	3852	4536	3636

Lean loading (mol_{CO2}/mol_{PZ})	0.25	0.28	0.31	0.27	0.26
Absorber pressure (bar)	1.01	1.01	1.01	1.01	1.01
Rich temperature (°C)	46.9	41.6	43.9	47.5	42.7
Rich flow (kg/h)	3996	3204	3996	4752	3816
Stripper pressure (bar)	1.379	1.379	4.136	3.156	3.446
Reboiler duty (GJ/t_{CO2})	4.32	3.97	4.33	4.42	4.16
Reboiler temperature (°C)	108.9	105.7	127.5	129	128.2
Condenser temperature (°C)	9.0	11.3	19.6	20.1	4.8
CO_2 production (kg/h)	129.6	100.8	93.6	115.2	111.6

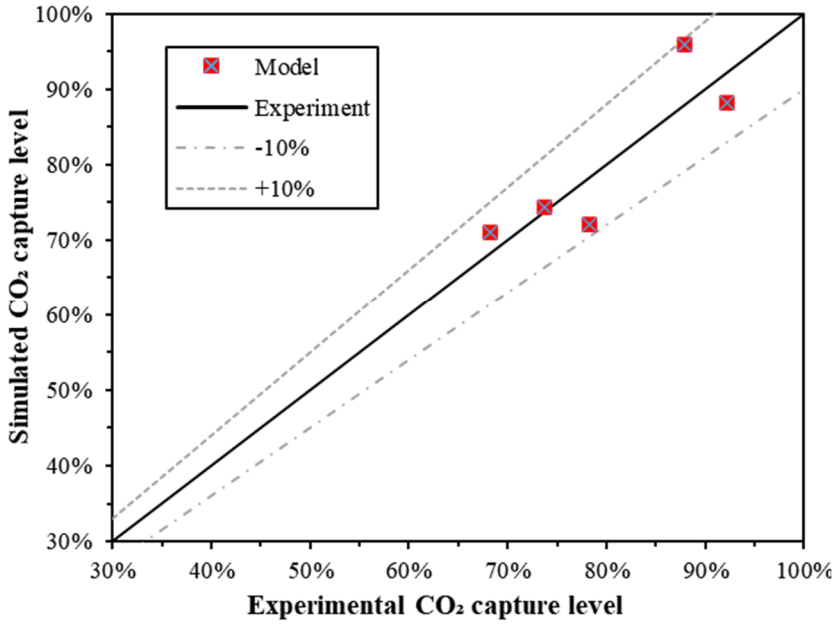

Figure 3.11 Validation results of carbon capture rate for standard PCC process using PZ

Figure 3.11 compared the simulated CO_2 capture levels with the experimental data. All points are within the ±10% deviation range. Cases 3 and 13 had a relatively higher deviation. This could be attributed to the low flue gas temperatures in these tests, specifically 0°C for Case 3 and -9°C for Case 13.

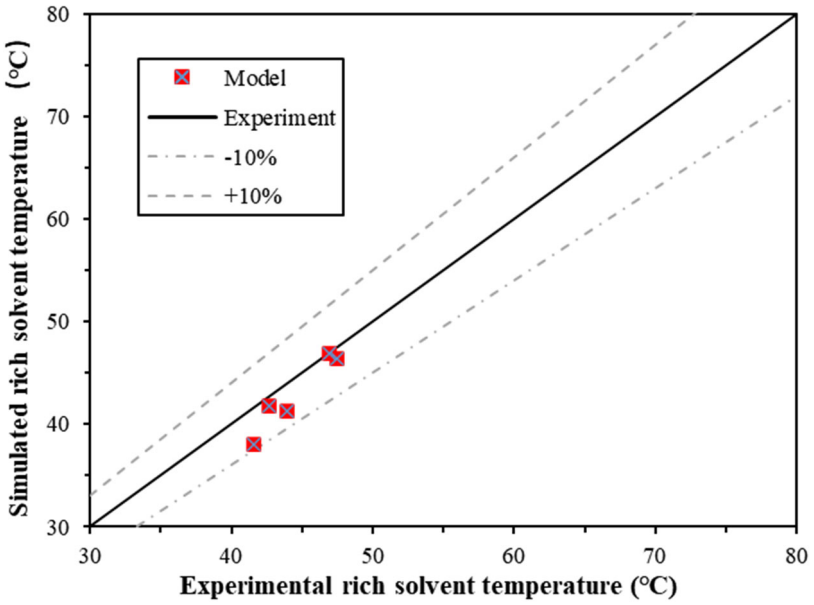

Figure 3.12 Validation results of rich solvent temperature for standard PCC process using PZ

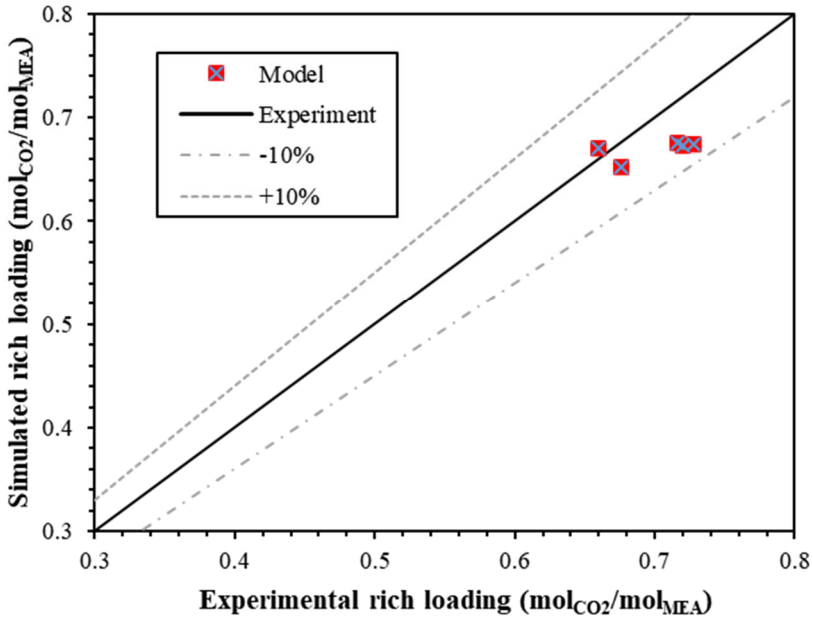

Figure 3.13 Validation results of rich loading for standard PCC process using PZ

As illustrated in Figure 3.12 and Figure 3.13, the simulation showed a good agreement with the experimental data for both rich solvent temperature and loading, with deviations consistently within ±10%.

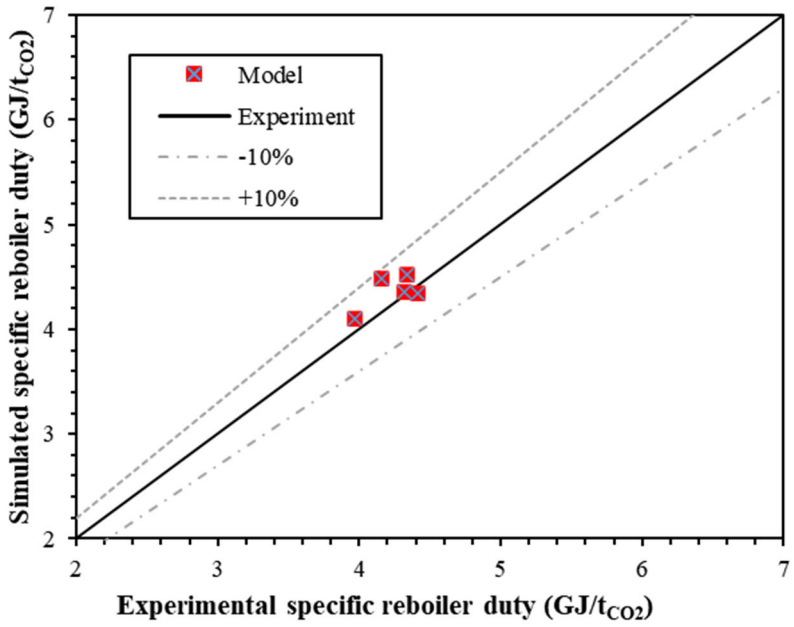

Figure 3.14 Validation results of specific reboiler duty for standard PCC process using PZ

Figure 3.14 validated the specific reboiler duty against the pilot plant data, and all data points fell within the ±10% deviation range. The validation results indicated that this simulation had a good level of accuracy in predicting the CO_2 absorption and energy performance of PCC process using PZ solvent.

3.3.3 Model scale-up of the solvent-based PCC for a 550 MWe BFPP

The pilot-scale models were scaled up to capture CO_2 from the flue gas of the 550 MWe supercritical BFPP reported by NETL (2012), Case PN1. The gas composition includes 68.5 vol% N_2, 15.5 vol% CO_2, 2.3 vol% O_2, 0.8 vol% Ar and 12.9 vol% H_2O. The flue gas mass flow rate is 647.6 kg/s, with an inlet temperature of 40 °C. A 90% CO_2 capture efficiency was assumed. The scale-up method utilised the generalised pressure drop correlation (GPDC), as detailed by Canepa et al. (2013).

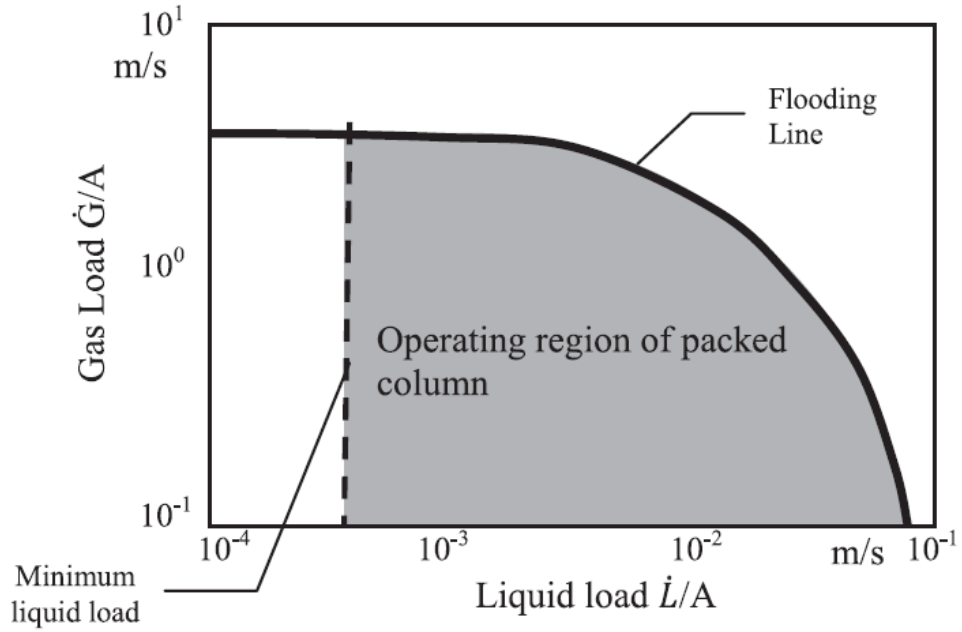

Figure 3.15 The operating condition of the packed column (Lawal et al., 2012)

As illustrated in Figure 3.15, the operational range of packed columns is primarily constrained by the flooding line and the minimum liquid load. Flooding arises when the gas flow causes a significant pressure drop, hindering the downward movement of the liquid. This phenomenon restricts the maximum capacity of both the absorber and the stripper. On the other hand, the minimum liquid load represents the lowest flow rate required to wet the entire surface of the packing adequately (Lawal et al., 2012). Therefore, to avoid flooding and achieve optimal liquid-gas distribution, a pressure drop of 15–50 mmH_2O per meter of packing in packed columns is recommended (Sinnott, 2005). Canepa et al. (2013) recommended to use of pressure drops of 21 or 42 mmH_2O per meter of packing when using the GPDC method for model scale-up. In this study, 21mmH_2O per meter of packing is used. A higher pressure drop increases gas velocity, potentially enhancing interfacial area and mass transfer. However, this results in a smaller calculated column diameter and increases the risk of flooding. In contrast, a lower pressure drop helps reduce flooding risk and improves operational reliability. Therefore, 21 mmH_2O was therefore adopted to ensure stable and energy-efficient operation.

The large-scale model utilises the same operating temperature and pressure for the absorber and stripper as those in the pilot-scale model. Both the MEA and PZ cases employ the same packing type, Mellapak 2X, for the absorber and stripper. This ensures that CO_2 absorption performance is not influenced by differences in packing type.

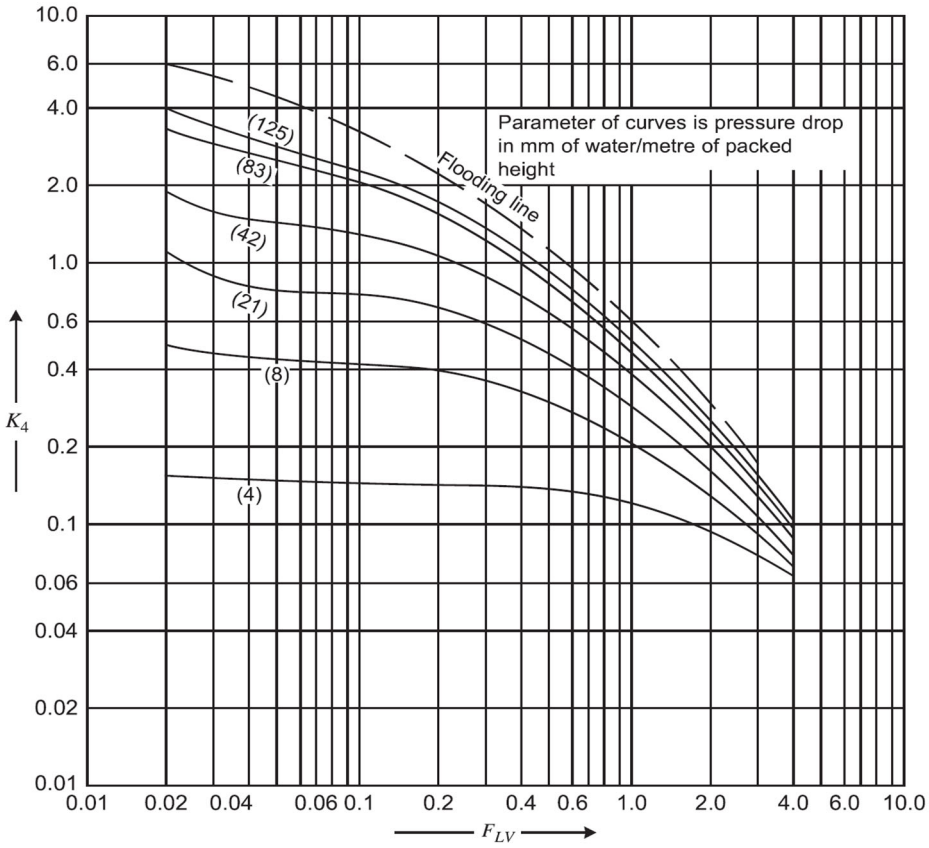

Figure 3.16 The GPDC chart (Sinnott, 2005)

Figure 3.16 presents the GPDC chart for determining the cross-sectional area of columns. The horizontal axis represents a flow parameter ($\mathrm{F_{LV}}$), which is related to the L/G ratio, calculated using the following equation (Canepa et al., 2013):

$$\mathrm{F_{LV}} = \frac{\mathrm{L_{\dot{W}}}}{\mathrm{G_{\dot{W}}}} \sqrt{\frac{\rho_G}{\rho_\mathrm{L}}} \tag{3.15}$$

Where $\mathrm{L_{\dot{W}}}$ is the designed lean solvent flow rate (kg/s), $\mathrm{G_{\dot{W}}}$ is the flue gas flow rate (kg/s), ρ_G is the density of gas (kg/m^3), $\rho_\mathrm{L}$is the density of liquid (kg/m^3).

The vertical axis represents the modified load ($\mathrm{K_4}$), which can be determined from Figure 3.16 based on the $\mathrm{F_{LV}}$ value. Eq. (3.16) describes the relationship between $\mathrm{K_4}$ and cross-sectional area factor ($\mathrm{G^*_W}$).

$$\mathrm{K_4} = \frac{13.1(\mathrm{G^*_W})^2 \mathrm{F_P} (\frac{\mu_\mathrm{L}}{\rho_\mathrm{L}})^{0.1}}{\rho_\mathrm{G}(\rho_\mathrm{L} - \rho_\mathrm{G})} \tag{3.15}$$

Where $\mu_\mathrm{L}$is the viscosity of liquid stream (Ns/m^2), $\mathrm{F_P}$ is the packing factor of the packed

column (m^{-1}), G^*_W is the gas mass flow rate per unit cross-sectional area ($kg/s \cdot m^2$).

Based on G^*_W and G_W, the estimated cross-sectional area of the absorber can be obtained. Also, based on the cross-sectional area, the diameter of the column can be calculated. The scale-up of the stripper followed the same GPDC method used for the absorber. The key design parameters—liquid and vapour flow rates, pressure drop, solvent properties, and packing factor—were used to estimate the required cross-sectional area. The liquid flow rate included both the rich solvent and the reflux stream, while the vapour flow rate was determined from the boil-up (Canepa et al., 2013). L_W represents the sum of the rich solvent flow rate and the reflux rate. G_W represents the boiled-up rate of the stripper. The calculated diameters are presented in Table 3.12.

Table 3.12 The first-guess design parameters of full-scale PCC for BFPP

Standard PCC process	30wt% MEA	40wt% PZ
Absorber		
Diameter (m)	15	14
Packing height (m)	25	25
Packing type	Mellapak 2X	Mellapak 2X
Flooding capacity	80.8%	79.1%
Stripper		
Diameter (m)	9	8
Packing height (m)	25	20
Packing type	Mellapak 2X	Mellapak 2X
Flooding capacity	79.9%	73.5%

Canepa and Wang (2015) pointed out that column diameters must remain within the structural limit of 12.2 m, so it is necessary to use multiple absorbers. Figure 3.17 illustrates the diameters required when utilising two, three, or four absorbers for using 30wt% MEA and 40wt% PZ. Moreover, using more absorbers would increase the CAPEX without significantly improving CO_2 absorption efficiency. Consequently, this study adopts two absorbers for both the MEA and PZ cases with a diameter of 10.6 m and 10 m, respectively. Meanwhile, a single stripper meets the structural limit, so the diameter of 9 m for MEA and 8m for PZ are applied.

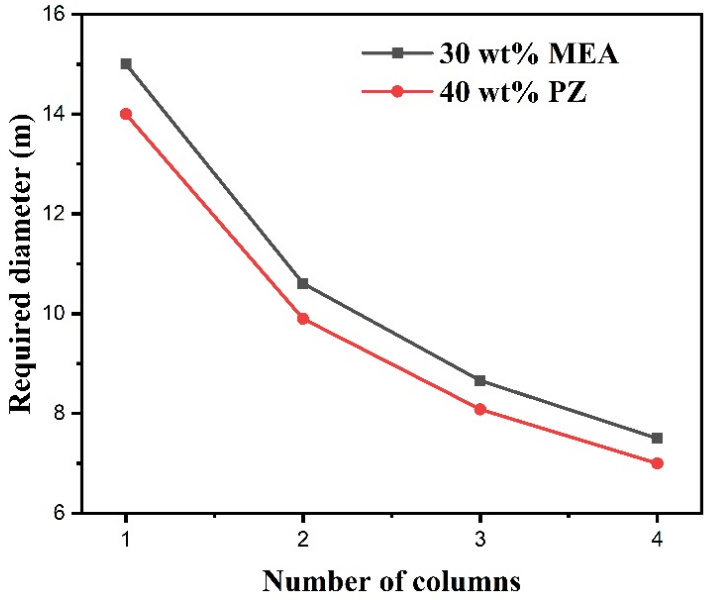

Figure 3.17 Required diameter varying column numbers (40wt% PZ)

3.4 Large-scale PCC processes with different configurations

3.4.1 Process description

3.4.1.1 Absorber intercooling

The three absorber configurations with intercooling are illustrated in Figure 3.18. Flue gas from a power plant is cooled to 40 °C in a direct contact cooler as recommended by Gao and Rochelle (2020). This temperature is chosen to align with the optimal range for CO_2 absorption reactions, which typically occurs between 40-60 °C (Wang et al., 2011). In the in-and-out AIC, part of the solvent from the bottom of the middle bed is extracted, cooled, and returned to the top of the bottom bed. In the pump-around AIC configuration, the rich solvent from the absorber's bottom is recycled, cooled, and reintroduced to the top of the bottom bed.

As CO_2 absorption is an exothermic reaction, the solvent temperature increases during the CO_2 absorption process in the absorber. However, research indicates that the optimal reaction temperature is between 40-60 °C, and elevated temperatures can hinder absorption efficiency (Wang et al., 2011). Intercooling helps mitigate temperature bulge and enhances CO_2 capture performance (Plaza, 2011).

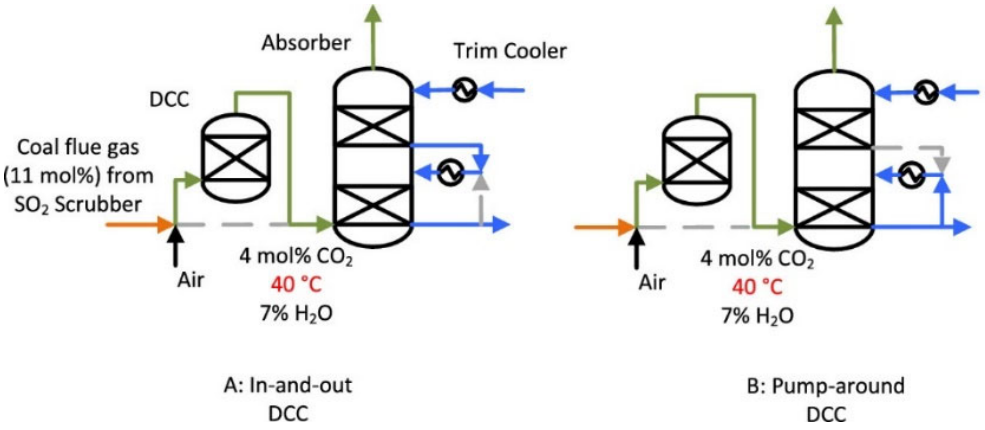

Figure 3.18 The configurations of in-and-out and pump-around absorber intercooling (Gao and Rochelle, 2020)

3.4.1.2 Advanced flash stripper

The AFS process configuration is illustrated in Figure 3.19. Following the absorber, the rich solvent will go through a pump to increase the pressure and then split into two streams: the cold-rich bypass and the primary stream. The primary stream is heated in the first-stage heat exchanger, while the hot overhead gas of the stripper heats the cold-rich bypass. Afterwards, the rich solvent exiting the first-stage exchanger is further split into a warm-rich bypass and another primary stream. This primary stream will go through the second-stage heat exchanger, which is preheated and then partially vaporised using a steam heater before being transported to the stripper. In the stripper, CO_2-rich hot gas is released from the top while the lean solvent leaves from the bottom. The warm rich bypass cools down the CO_2-rich hot gas. The lean solvent is cooled using two heat exchangers and a cooler before being recycled to the absorber. By using AFS, the latent heat of the stripper's CO_2-rich hot gas is reused to heat the bypass stream (Rochelle et al., 2018). Also, the cold-rich bypass helps cool the hot gas leaving the stripper and lower the PCC system's heat consumption.

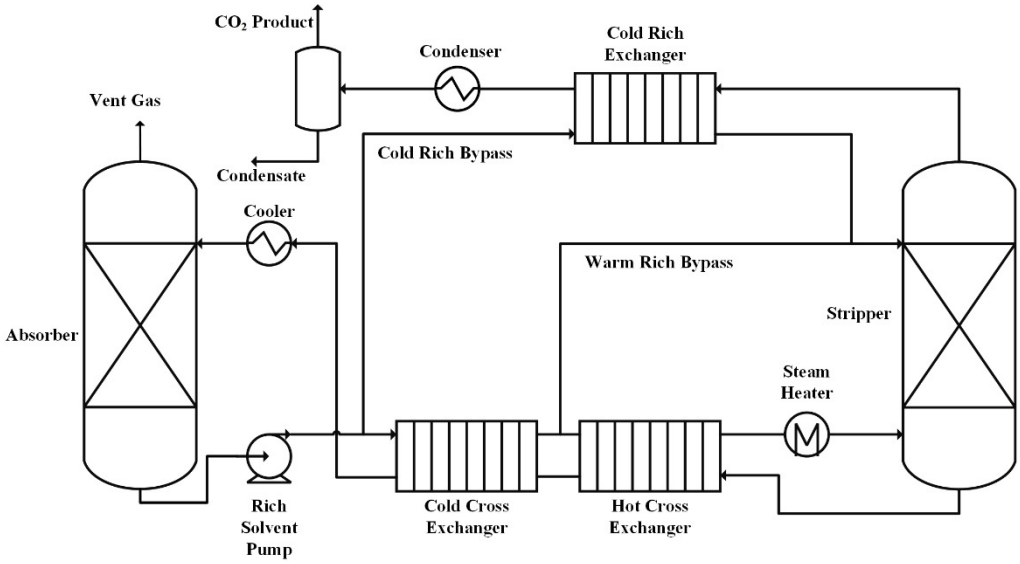

Figure 3.19 The flowsheet of the AFS process design

3.4.1.3 Side stream extraction (SSE)

Figure 3.20 illustrates the SSE process configuration. In this configuration, the semi-rich amine solvent is partially extracted from the middle section of the stripper, cooled and pumped to the middle section of the absorber. This semi-rich stream will help preheat the rich bypass stream.

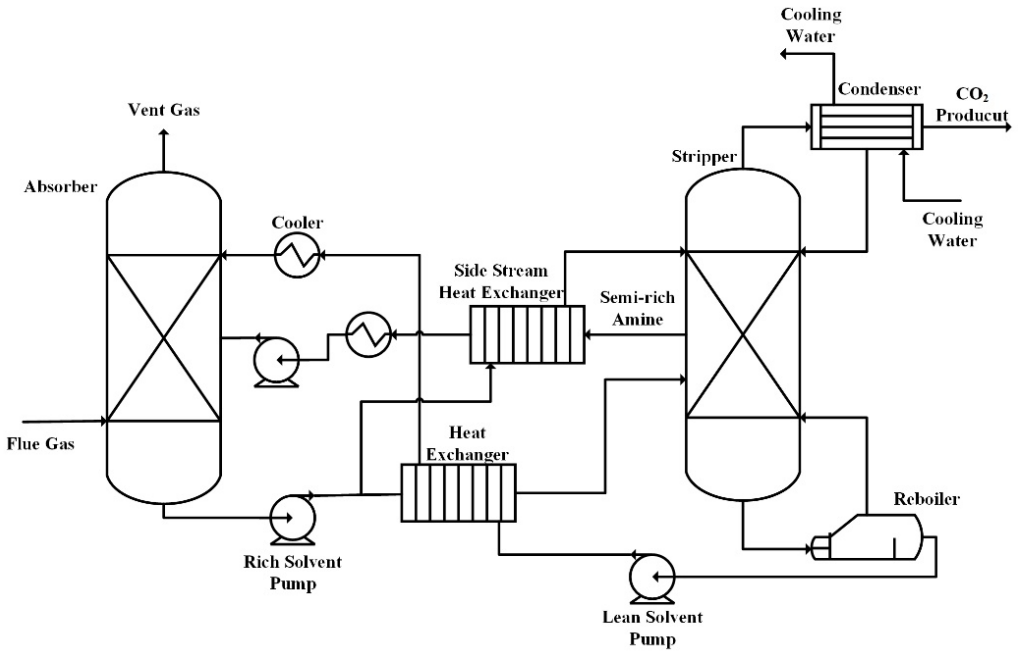

Figure 3.20 The flowsheet of solvent-based PCC with SSE configurations

3.4.1.4 CO_2 compression units with heat pump (HP) and supercritical CO_2 (sCO_2) cycle

As shown in Figure 3.21, the HP and sCO_2 cycles were added to the standard four-stage CO_2 compression units. In the fourth stage, the HP substitutes the conventional compressor to liquefy the high-pressure CO_2. Subsequently, the pressure of the CO_2 liquid is increased to 200 bar using a pump and split into three sub-streams. These sub-streams are used to absorb heat from the intercoolers and then get merged before sending to the sCO_2 turbine. Then, this heated sCO_2 will drive the sCO_2 turbine for power generation, cool down and be pressurised to 150 bar before storage.

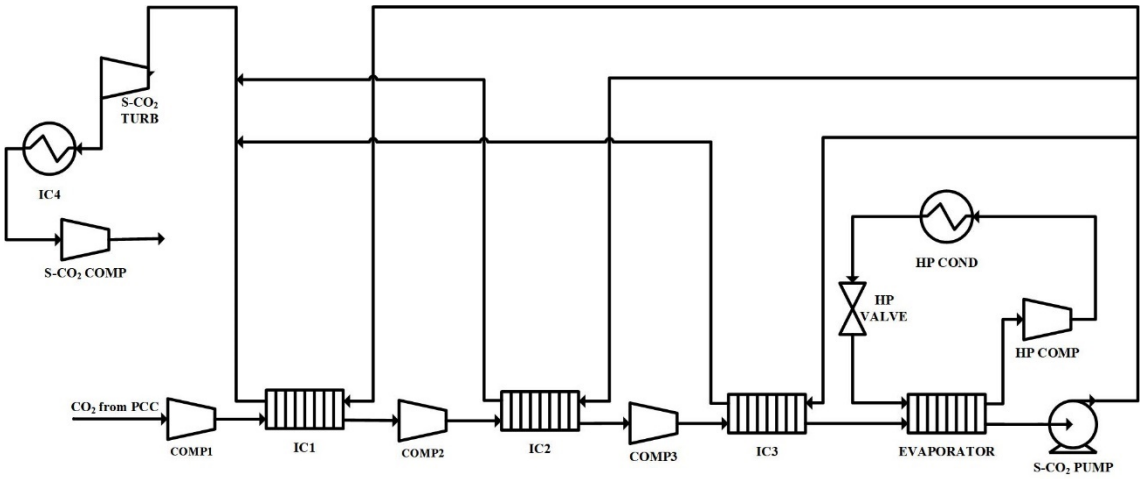

Figure 3.21 The flowsheet diagram of the CO_2 compression unit with HP and sCO_2

3.4.2 Simulation of different PCC process configurations

3.4.2.1 Simulation of PCC process with AIC and AFS

Different process configurations were investigated to improve the energy efficiency of the PCC process. As illustrated in Figure 3.22, full-scale PCC with pump-around AIC and AFS was simulated in Aspen Plus® V11 for BFPP. The pump-around AIC was simulated using the built-in Pumparounds block configuration in Aspen Plus®, and therefore, it is not displayed in the process flowsheet (Figure 3.22). The processes of in-and-out and pump-around AIC have been introduced in Section 3.4.1.1. Gao and Rochelle (2020) demonstrated that the pump-around type performs better in enhancing the CO_2 capacity of the lean solvent than the in-and-out type. Following the absorber with AIC, the AFS configuration described in Section 3.4.1.2 was applied. Through using the AFS configuration, the latent heat of the stripper overhead outlet

stream was utilised to preheat heat the rich solvent bypass. At the same time, the rich solvent bypass was also used to condense the stripper overhead vapour.

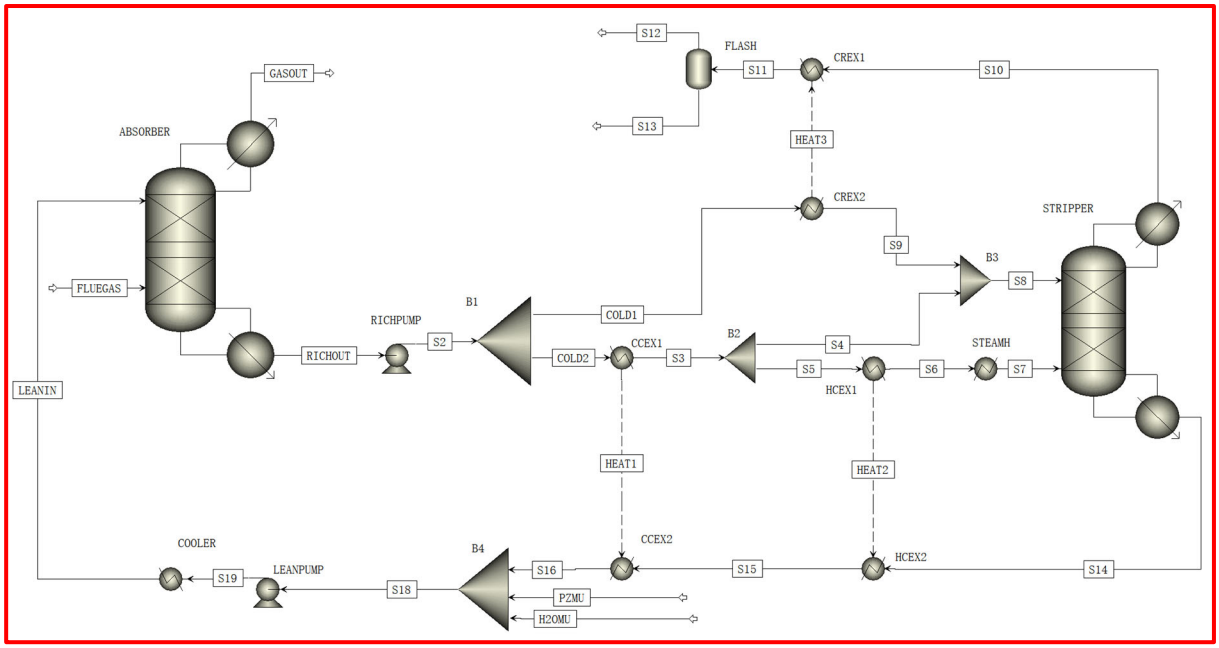

Figure 3.22 The flowsheet of the PCC process with pump-around AIC and AFS in Aspen Plus®

3.4.2.2 Simulation of PCC process with AIC, AFS and SSE

SSE is added to the AIC-AFS configuration, as illustrated in Figure 3.23. The semi-rich solvent is withdrawn from the stripper's middle stage to provide heat for the warm-rich bypass before being returned to the middle section of the absorber. This process decreases the amount of rich solvent requiring regeneration in the stripper, reducing the energy needed for regeneration. Furthermore, the side-stream heat exchanger is designed with a minimum temperature approach of 5 °C to increase heat recovery efficiency.

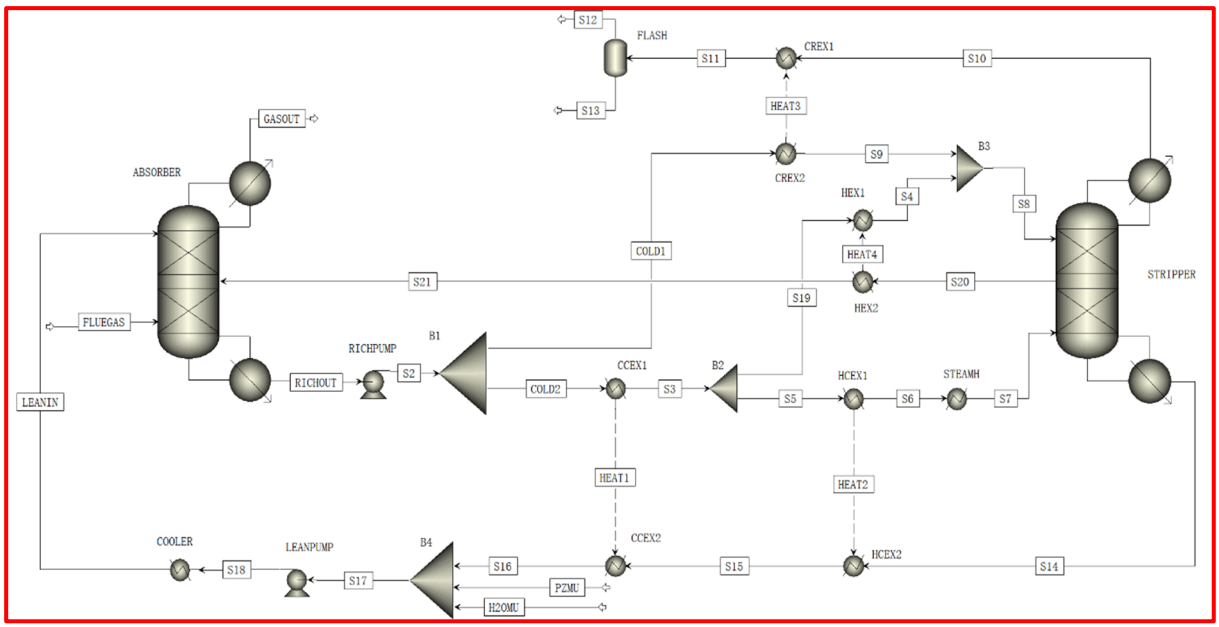

Figure 3.23 The flowsheet of the PCC process with pump-around AIC, AFS and SSE in Aspen Plus®

3.4.2.3 Simulation of different CO_2 compression configurations

Firstly, the simulation of a standard four-stage compressor was carried out. The compression system pressurized the concentrated CO_2 to 150 bar as indicated in Figure 3.24. To regulate the temperature, an intercooler is installed between each stage, ensuring the gas is cooled to 30°C.

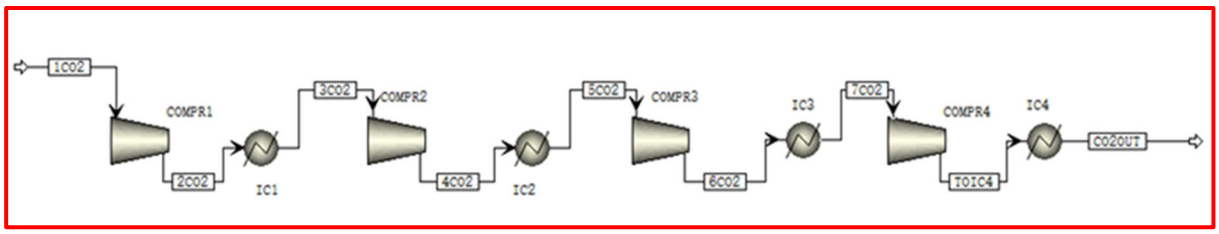

Figure 3.24 The flowsheet of the standard four-stage compressor in Aspen Plus®

To lower the energy consumption for CO_2 compression, the configuration of the standard four-stage compressor is improved by integrating with HP and the sCO_2 cycle. As illustrated in Figure 3.25, an HP replaces the final stage of the four-stage CO_2 compression train to enable liquefaction of CO_2 using Propane (R290) as a refrigerant. The R290 cools down the concentrated CO_2, drives the HP, and releases the heat into the atmosphere. For liquefaction, the CO_2 pressure has to surpass its triple point pressure of 5.18 bar (Alabdulkarem et al., 2012).

In the four-stage compression, the pressure after the first-stage compressor reaches 10.15 bar, so the HP cycle liquefaction process can only be implemented from the second-stage compressor. The CO_2 is liquefied at its saturation temperature corresponding to the inlet pressure of the HP. In the evaporator, a pinch point temperature of 5°C is assumed, along with a 5°C superheat for the refrigerant. Moreover, in the HP compressor, it is assumed that the refrigerant goes through an isentropic compression process with an efficiency of 80%. Subsequently, the refrigerant is cooled to 30°C in the HP condenser before undergoing an isenthalpic expansion process and returning to the evaporator.

Following the HP unit, the captured CO_2 is in liquid form and is pressurised to 200 bar using a pump. The CO_2 is pumped to 200 bar based on the sCO_2 configuration proposed by Muhammad et al. (2020), where a pump is used to raise the CO_2 pressure to above 200 bar to ensure that the CO_2 can reach supercritical conditions and to meet the design requirements of the downstream sCO_2 cycle. The pressurised CO_2 is then split into three streams, each preheated using intercooling heat recovered from the multi-stage compression train. In conventional compression systems, intercoolers are used to reduce the outlet temperature of the compressors, resulting in high cooling demands. In this system, the intercooling heat is recovered to raise the temperature of the pressurised CO_2 to supercritical conditions. The sCO_2 is subsequently expanded in a turbine for power genenration. After expansion, the CO_2 is cooled to 30°C and recompressed to 150 bar for storage.

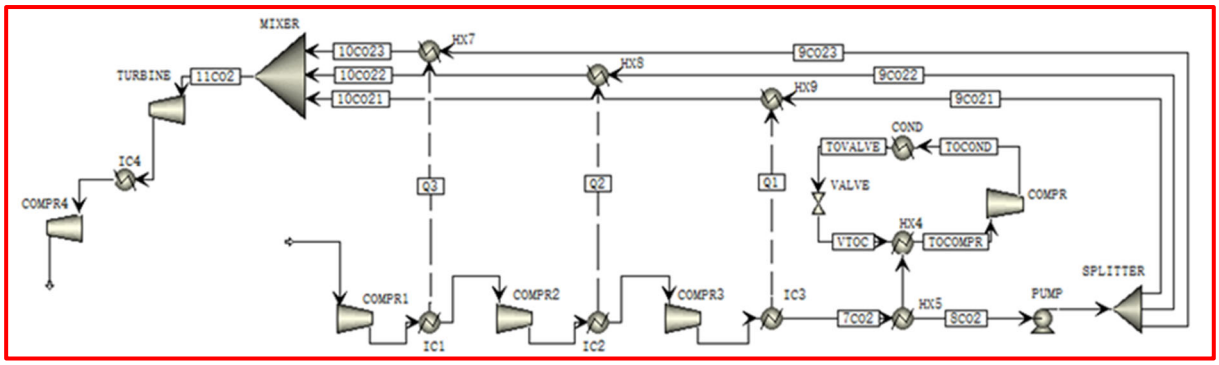

Figure 3.25 The flowsheet of CO_2 compression units with HP and sCO_2 cycle in Aspen Plus®

3.5 Conclusion

Chapter 3 presented the steady-state simulation of a 550 MWe BFPP and the steady-state simulation of both pilot and large-scale PCC processes using MEA and PZ in Aspen Plus®. The

model of BFPP was developed and validated based on the reference introduced in NETL (2012), which was divided into three subsystems: boiler, turbine and feedwater subsystems. The simulation results of key operating indicators, such as the power output and efficiency, as well as the stream data (temperature, pressure and mass flow rate), were compared with the reference data. Additionally, the models of the PCC process using MEA and PZ as the solvents are simulated and validated at a pilot scale based on the tests at the University of Kaiserslautern and the University of Texas at Austin, respectively. This pilot-scale PCC model was then scaled up for processing flue gas from the 550 MWe BFPP. Furthermore, different configurations of PCC processes were simulated in Aspen Plus®. The following are the key findings of this chapter:

- From the results of the model comparison of BFPP, the deviations of gross power output, net plant power output, and efficiency are 0.06%, 0.14% and 2.42%, respectively. The simulated stream data also showed a good agreement with the reference data.
- The validation results of the PCC process using MEA and PZ showed that all the relative errors against the pilot plant data are within the ±10% range. The results confirmed the reliability of this model to predict the CO_2 capture process using MEA and PZ.
- The scale-up results indicated that two absorbers were required for both the MEA and PZ cases, with diameters of 10.6 m and 10 m, respectively. Additionally, a single stripper with diameters of 9 m for MEA and 8 m for PZ was applied.

Chapter 4 Techno-economic analysis and optimisation of PZ-based PCC process for supercritical BFPP through simulation

4.1 Overview

This chapter mainly focuses on optimising the energy and economic performance of the large-scale PCC process using PZ as the solvent. Several key parameters influencing the energy performance of the PCC processes were discussed in Section 4.2. For the standard PCC process, the impact of lean solvent loading and absorber packing height on the regeneration heat duty was analysed. Additionally, using the AFS configuration, the heat duty was evaluated across different split ratios. Then, to determine the optimal pressure ratio for the sCO_2 turbine, the impact of the pressure ratio on the power output of the sCO_2 cycle was also explored. Sections 4.3 and 4.4 explore the energy and economic performance of various process configurations and solvent concentrations, respectively. Section 4.5 proposed optimisation of CO_2 capture costs varying CO_2 concentrations and stripper pressures. The conclusions of Chapter 4 are given in Section 4.6.

4.2 Sensitivity analysis

4.2.1 The effect of lean loading on the regeneration heat duty of solvent-based PCC process

The impact of lean loading on the energy efficiency of the PCC process was analysed using a model of the standard PCC process using 30wt% MEA, 30wt% PZ and 40wt% PZ. In all cases, the CO_2 removal rate was maintained at 90%. In this analysis, 30wt% MEA served as the benchmark solvent. The comprehensive impact of lean loading on the regeneration heat duty is presented in Figure 4.1.

The total regeneration energy is the combined effects of sensible heat (required to heat the CO_2-loaded solution), latent heat (mainly for the vaporisation of water), and the reaction heat associated with CO_2 desorption (Yang et al., 2023). According to Abu-Zahra et al. (2007), at low lean loadings, more stripping steam is needed for CO_2 desorption, which increases the desorption heat demand. At high lean loadings, the increased solvent circulation rate leads to

higher sensible and latent heat consumption. As a result, a minimum in total thermal energy requirement is observed at the turning point of the curves.

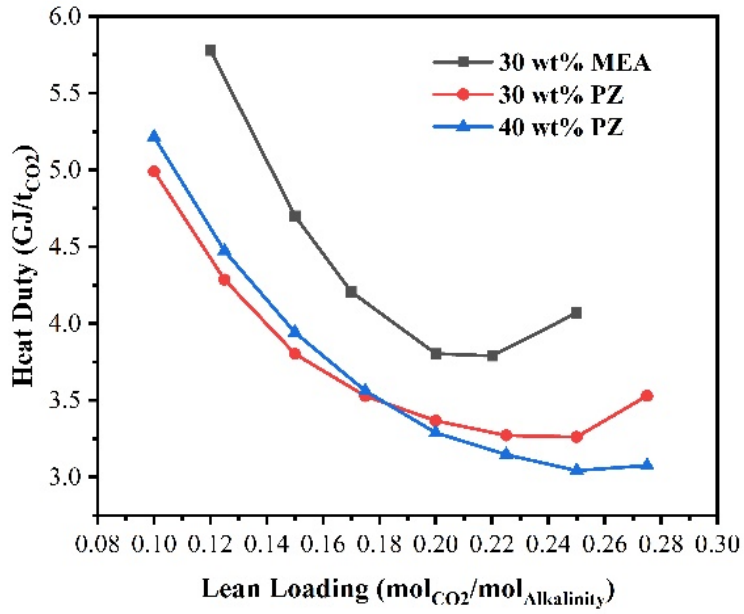

Figure 4.1 Heat duty varying lean loadings

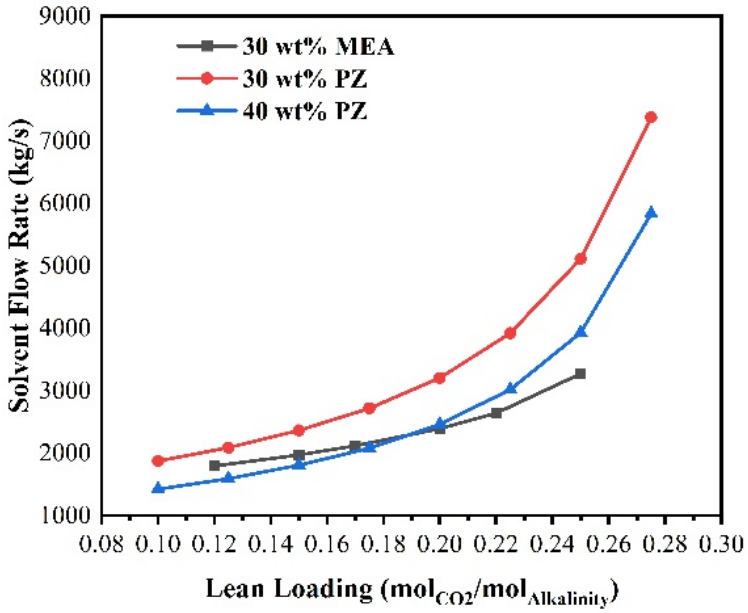

Figure 4.2 Solvent flow rate varying lean loading

Moreover, at low lean loadings, due to the relatively low solvent flow rate, the impacts of sensible and latent heat are minor, and the heat duty is mainly dominated by the desorption reaction heat. The desorption reaction can be expressed as reaction (R 4.1), according to

Zwitterion Mechanism (Vaidya and Kenig, 2007). AmH refers to amine solvent. With higher solvent concentration, based on Le Chatelier's Principle, the reaction equilibrium shifts to the left. Moreover, this is an endothermic reaction. Therefore, to achieve the constant level of carbon capture, more heat is needed. This is the reason that at low lean loading, 40wt% PZ cases showed higher heat duty than 30wt% PZ cases.

$$\mathrm{AmH^{+}COO^{-}} \leftrightarrow \mathrm{CO_2} + \mathrm{AmH} \qquad \text{(R 4.1)}$$

At high lean loadings, the solvent flow rate is high, which increases the sensible and latent heat. When the lean loading is higher than 0.175 $mol_{CO2}/mol_{Alkalinity}$, the sensible and latent heat dominate the total regeneration heat duty. With higher solvent concentration, the solvent flow rate is lower. Thus, after the lean loading beyond than 0.175 $mol_{CO2}/mol_{Alkalinity}$, the heat duty of 40wt% PZ cases showed lower heat duty than 30wt% PZ cases.

Figure 4.2 presented the relationship between the lean loading and solvent flow rate. The solvent flow rate is determined based on the solvent concentration and the flow rate of CO_2 to be captured. For the regeneration process in the stripper, a lower lean loading corresponds to a higher CO_2 absorption capacity of the solvent, meaning that each unit of solvent can absorb more CO_2. Moreover, in this study, both the flue gas flow rate and the CO_2 capture level are fixed, so the CO_2 flow rate remains constant. Therefore, for a given solvent concentration, a lower lean loading results in a reduced solvent flow rate. In addition, increasing the solvent concentration can also reduce the solvent flow rate.

For 30wt% MEA, the lowest regeneration energy of 3.8 GJ/t_{CO2} was observed at a lean loading of 0.22 $mol_{CO2/}mol_{MEA}$, which was identified as the optimal condition for this solvent. For 30 and 40wt% PZ, the minimum energy consumption was 3.26 and 3.0 GJ/t_{CO2}, respectively, both achieved at a lean loading of 0.25 $mol_{CO2}/mol_{Alkalinity}$. These results indicate a 14%-21% reduction in regeneration energy when using PZ compared with the benchmark case. Nevertheless, based on Figure 4.2, at lean loadings exceeding 0.175 $mol_{CO2}/mol_{Alkalinity}$, the solvent flow rate increased significantly with higher lean solvent loading. Therefore, a lean loading of 0.35 mol_{CO2}/mol_{PZ} was selected for the PZ cases (30wt% and 40wt%).

Furthermore, as a diamine, PZ contains 2 moles of alkalinity per mole of amine. For instance, as shown in Figure 4.2, a lean loading of 0.10 $mol_{CO2}/mol_{Alkalinity}$ corresponds to 0.20

mol_{CO2}/mol_{amine} for PZ. At this lean loading, the solvent flow rates for 30wt% MEA and PZ were 2389.93 kg/s and 1870.45 kg/s, respectively. The findings in Figure 4.2 also confirm that PZ shows a higher CO_2 capacity than MEA, requiring less solvent under the same CO_2 loading.

4.2.2 The effect of the absorber packing height on the regeneration heat duty of PCC

The impact of absorber packing height on the heat duty for solvent regeneration was analysed using the standard PCC model. The design parameters presented in Table 3.12 were applied in this section, with two absorbers, each having a diameter of 10 m. Packing heights ranging from 7 m to 19 m were tested for each absorber. In this analysis, the CO_2 capture level was consistently maintained at 90%.

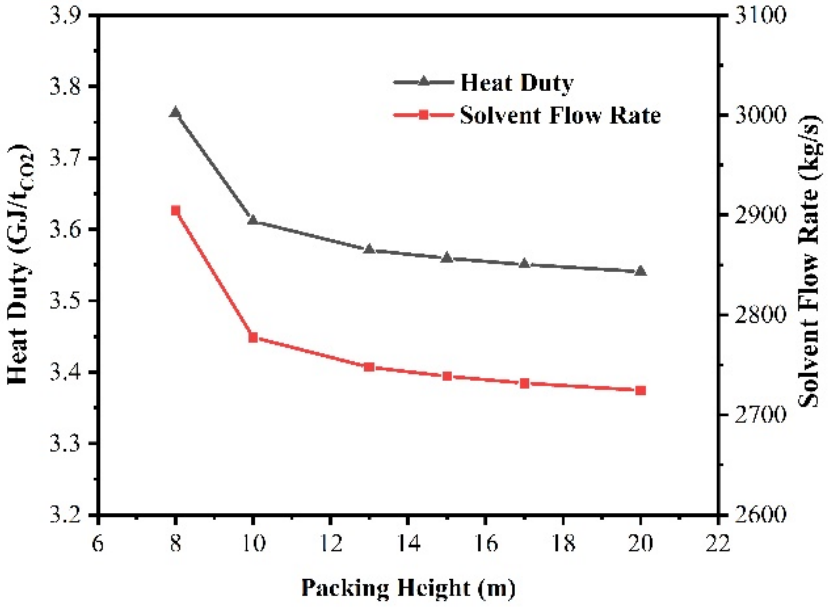

Figure 4.3 Heat duty and solvent flow rate varying absorber packing heights (30wt% PZ)

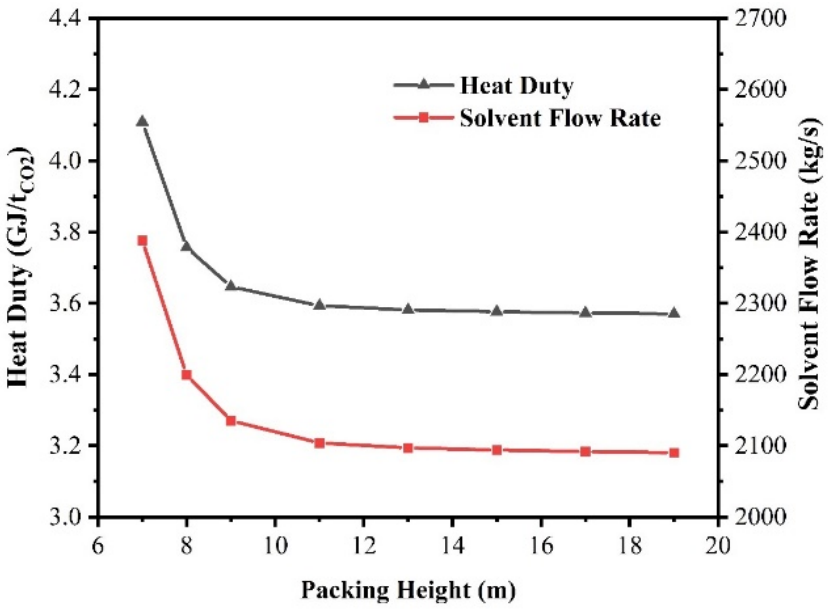

Figure 4.4 Heat duty and solvent flow rate varying absorber packing heights (40wt% PZ)

The results indicated that increasing the packing height reduces the solvent flow rate, and thus lowers the heat required for regeneration. A decrease in required regeneration heat also helps lower operating costs. However, larger equipment sizes due to increased packing height result in higher capital costs for the column. As illustrated in Figure 4.3, when using 30wt% PZ, a significant reduction in energy consumption was observed as the packing height increased from 8 m to 13 m, and further increases in packing height had minimal impact on energy savings. Consequently, a packing height of 13 m was chosen for 30wt% PZ cases. A similar trend was observed in Figure 4.4 for 40wt% PZ and an 11 m packing height was chosen for 40wt% PZ cases.

4.2.3 The effect of split ratio on the regeneration heat duty of PCC

The impact of the split ratio on the heat duty of the PCC process was investigated using the PCC model with AIC-AFS. To efficiently use the waste heat from the hot outlet streams of the stripper, the impact of the split ratios of the cold-rich and warm-rich bypasses on the heat duty was evaluated.

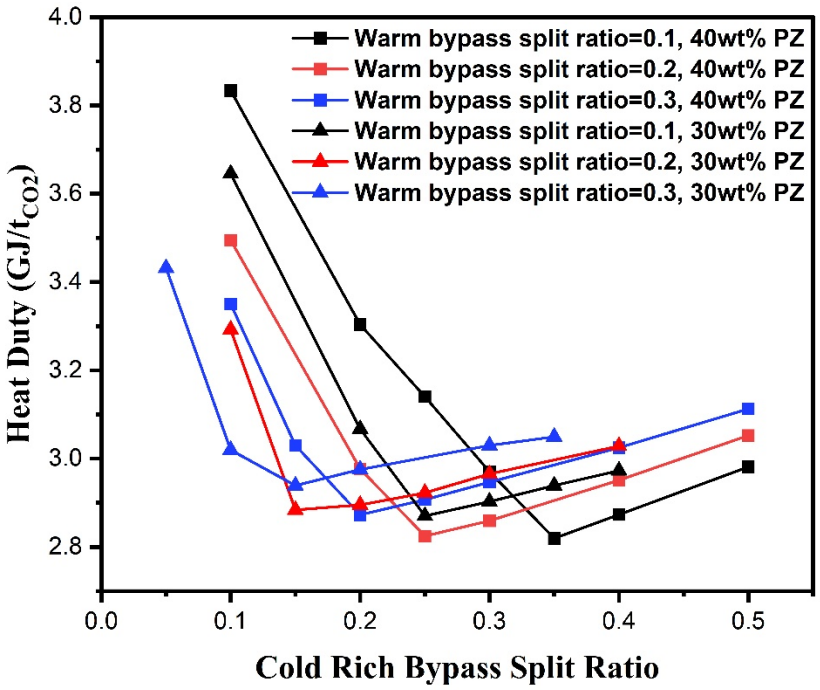

Figure 4.5 Heat duty varying different split ratios (30wt% PZ and 40wt% PZ)

Increasing the cold-rich bypass split ratio enhances heat recovery from the hot stripper overhead gas outlet via the cold-rich exchanger. At the same time, it reduces the flow rate of the cold-rich bypass and limits the heat recovery in the cold cross exchanger. The warm-rich bypass is adjusted to manage the stripper inlet temperature, which should remain between 95°C and 120°C (Adu et al., 2020). A higher warm-rich bypass split ratio allows greater heat recovery in the cold-rich exchanger but decreases heat recovery from the hot lean solvent exiting the stripper. The turning point in the curve is due to the heat recovery mechanism in the AFS configuration. Before the turning point, increasing the cold rich bypass split ratio results in more heat being recovered from the CO_2-rich hot gas at the top of the stripper via the cold rich exchanger, which lowers the reboiler duty. However, beyond the turning point, the available heat in the CO_2-rich hot gas becomes limited. Further increasing the split ratio diverts more cold rich solvent away from the hot lean solvent at the bottom of the stripper, reducing heat recovery from that stream and causing the reboiler duty to rise. Considering different factors, Figure 4.5 show that the optimal cold-rich bypass split ratios are 0.25 for the 30wt% case and 0.35 for the 40wt% case, with an optimal warm-rich bypass split ratio of 0.1 for both. The corresponding minimum heat duties are 2.87 GJ/t_{CO2} for 30wt% PZ and 2.82 GJ/t_{CO2} for 40wt% PZ.

4.2.4 The effect of the sCO_2 turbine pressure ratio on the energy demand of CO_2 compression process

For the model of using HP-sCO_2 for CO_2 compression units, the impact of the sCO_2 turbine pressure ratio on the energy consumption of the CO_2 compression process was analysed. The net power output of the sCO_2 cycle was examined for turbine pressure ratios ranging from 0.3 to 0.7. The pressure of the inlet sCO_2 flow to the sCO_2 turbine was maintained at 200 bar, while the output pressure of the entire compression unit was fixed at 150 bar. A higher pressure ratio of the sCO_2 turbine leads to a higher output pressure, which corresponds to a higher input pressure for the sCO_2 compressor. Thus, with identical inlet and outlet pressures for the sCO_2 cycle, increasing the turbine's pressure ratio decreases the compressor's pressure ratio. For the sCO_2 turbine, power output decreases as the pressure ratio increases, whereas for the sCO_2 compressor, power requirements increase as the pressure ratio increases.

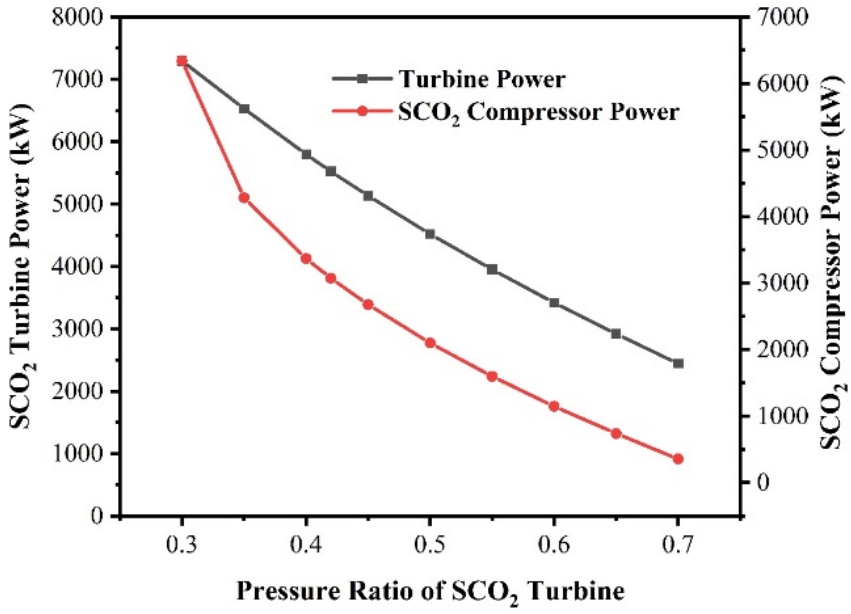

Figure 4.6 SCO_2 turbine power and compressor power varying sCO_2 turbine pressure ratio

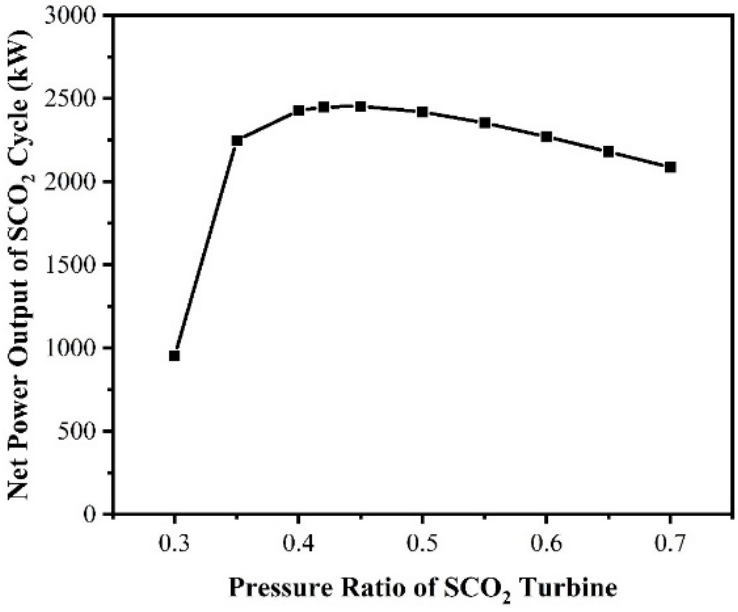

Figure 4.7 The net power output of the sCO_2 cycle varying sCO_2 turbine pressure ratio

Figure 4.6 illustrates the sCO_2 turbine and compressor power variations with different turbine pressure ratios. A significant drop in compressor power occurs between pressure ratios of 0.3 and 0.35, due to approaching the critical point where CO_2 density changes significantly.

Figure 4.7 illustrates the impact of the turbine pressure ratio on the sCO_2 cycle's net power output. In this figure, the net power output of the sCO_2 cycle is calculated as the difference between the sCO_2 turbine power and the sCO_2 compressor power, both of which are shown in Figure 4.6. Therefore, based on the results of Figure 4.6, the net power output of the sCO_2 cycle initially increases and then declines after the turning point. The results indicate that the optimal turbine pressure ratio is 0.45, producing a net power output of 2454.3 kW.

4.3 Energy analysis of PCC processes for a supercritical BFPP

According to the results of the sensitivity analysis from Section 4.2, the recommended operating conditions of different configurations are summarised in Table 4.1. These configurations included standard PCC integrated with a conventional CO_2 compression train, AIC-AFS integrated with a conventional CO_2 compression train, AIC-AFS-SSE integrated with a conventional CO_2 compression train, and AIC-AFS-SSE integrated with an HP-sCO_2 compression unit. For comparison, the benchmark case featured the standard carbon capture and compression process using 30wt% MEA.

Table 4.1 Recommended operating conditions based on sensitivity analysis for different PCC process configurations

Configuration	Solvent concentration	Lean loading (mol_{CO2}/mol_{amine})	Optimal split fraction		Heat duty (GJ/t_{CO2})
			Cold rich bypass	Warm rich bypass	
Standard	30wt% MEA	0.22	-	-	3.79
	30wt% PZ	0.35	-	-	3.58
	40wt% PZ	0.35	-	-	3.58
IC-AFS	30wt% PZ	0.35	0.25	0.1	2.87
	40wt% PZ	0.35	0.35	0.1	2.82
IC-AFS-SSE	30wt% PZ	0.35	0.25	0.1	2.81
	40wt% PZ	0.35	0.35	0.1	2.78

Heat duty is regarded as the most sensitive criterion for determining the energy performance of the PCC process. The heat duty for different PCC processes is presented in Table 4.1. The results indicate that utilizing 40wt% PZ reduces the heat duty by 0.2 GJ/t_{CO2} compared to the 30wt% MEA. The standard PCC process using 30 and 40wt% PZ have the same regeneration energy of 3.58 GJ/t_{CO2}, as a lean loading of 0.35 mol_{CO2}/mol_{PZ} was chosen for both cases, as indicated in Figure 4.1. Additionally, applying the AIC-AFS configuration reduces the heat duty by 18.4% and 21.2% for 30 and 40wt% PZ, respectively, compared to the MEA case. Additionally, applying SSE to PZ-based AIC-AFS configuration further reduces the heat duty by approximately 0.05 GJ/t_{CO2}.

To assess the energy penalty related to the integration of PCC to the BFPP, the total equivalent work (W_{eq}) was calculated for various configurations as follows:

$$W_{eq} = W_{heat} + W_{pump} + W_{comp} \quad (4.1)$$

Where W_{heat} is the equivalent work of heat duty of steam extraction from BFPP, which is calculated based on Eq. (4.2):

$$W_{heat} = \eta_{Turb}\left(\frac{T_{steam} - T_{sink}}{T_{steam}}\right) Q_{reb} \quad (4.2)$$

where η_{Turb} represents the turbine efficiency, assumed to be 90% (Lin and Rochelle, 2014). T_{sink} is the sink temperature, assumed to be 313.15 K. T_{steam} is the steam temperature calculated as the reboiler temperature added a steam-side temperature approach of 10 K. Q_{reb} represents the reboiler duty.

In Eq. (4.1), W_{pump} represents the total pumping work involved in the carbon capture process. This includes the power required to pressurize the rich solvent from the absorber and transfer it to the stripper. Additionally, for CO_2 compression units with HP-sCO_2 cycle, the power needed to pressurize the liquefied CO_2 is also included. It is assumed that the pumping power is supplied by electricity generated from BFPP.

W_{comp} represents the total CO_2 compression work. In the standard CO_2 compression train, this work is the sum of the duties across all compressors. For CO_2 compression units with HP-sCO_2 cycle, W_{comp} is calculated as follows:

$$W_{comp} = W_{comp,CO_2} + W_{comp,HP} - W_{net,cycle} \quad (4.3)$$

where W_{comp,CO_2} represents the sum of the compression work of the compression train before HP. $W_{comp,HP}$ represents the work of the HP compressor. $W_{net,cycle}$ represents the work output of the sCO_2 cycle, calculated as the power output of the sCO_2 turbine minus the energy consumption of the final-stage compressor.

The results of W_{eq} are illustrated in Figure 4.8. The results indicate that the regeneration process used the largest proportion of the total energy consumption of the PCC process. By using PZ solvent, with standard configuration, it can reduce the W_{eq} of approximately 1 kJ/mol_{CO2} for the 30wt% PZ cases compared to 30wt% MEA. From Figure 4.8, the standard 40wt% PZ cases have higher W_{heat} compared MEA case, but the standard PZ cases demonstrate lower heat duty (indicated in Table 4.1) than the MEA case. This is because the PZ cases operate at a higher stripper pressure (4.14 bar) than the MEA case (1.9 bar), leading to a higher reboiler temperature. So, according to Eq. (4.2), the calculated W_{heat} of PZ cases is higher than MEA cases. Additionally, the higher stripper pressure, which increases the inlet pressure of the CO_2 compression unit, results in lower compression duties for the PZ cases.

Applying AIC-AFS configuration also contributes to the reduction of W_{heat}. Compared with the case without using AIC-AFS, the energy savings of 18.9% and 21.1% were achieved using 30wt% and 40wt% PZ, respectively. Additionally, the CO_2 compressor is the second-largest energy consumer in the PCC process. By using HP-sCO_2 for compression, a saving of 2.2 kJ/molCO2, corresponding to a 21.1% reduction was achieved. The case utilizing AIC-AFS-SSE configuration, along with HP-sCO_2 for the CO_2 compression units and 40wt% PZ as the solvent, achieved the minimum W_{eq}. This configuration resulted in a reduction of 9.5 kJ/mol$_{CO2}$, representing a 20% saving compared to the standard 40wt% PZ case.

The cooling duty is also improved with the implementation of the modified configuration. By using the AFS configuration, the condenser is replaced with a cold-rich bypass to cool the stripper overhead vapour. As illustrated in Figure 4.9, this modification significantly reduces the cooling duty by 1.5 GJ/t$_{CO2}$, a 71% decrease. Despite adding AIC increases the cooling duty, the overall cooling duty of the AIC-AFS process still achieves a decrease of 6.6% (for 30wt% PZ) and 17.6% (for 40wt% PZ). Furthermore, compared to the standard CO_2 compression, using HP-sCO_2 for compression further reduces the cooling duty by 16.2% (as shown in Figure 4.9), due to the recovery of the compressor intercooling heat.

The impact of each component of the PCC process on the BFPP's energy penalty was evaluated. Steam extracted from BFPP supplies the power for the reboiler, while electricity supplies power for the other blocks listed in Table 4.2. The power penalty caused by steam extraction was determined using the heat of the extracted steam (Q_{steam}) and a power loss factor (σ), shown as follows (Linnenberg et al., 2011):

$$P_{loss,steam} = Q_{steam} \cdot \sigma \tag{4.4}$$

Where Q_{steam} is the heat duty required for solvent regeneration, σ is calculated using the following:

$$\sigma = a \cdot \frac{(T_{reb} - b)}{Q_{steam}} + c \tag{4.5}$$

Where a,b and c are power loss coefficients obtained from Linnenberg et al. (2011), T_{reb} is the reboiler temperature.

The calculated σ is 0.23 for the MEA case and 0.25 for the PZ cases. The cooling water pumping power (ΔP_{cw}) was determined using Eq. (4.6) from Linnenberg et al. (2011).

$$\Delta P_{cw} = \frac{Q_{cool} \times \varphi_{cw}}{c_{p,cw} \times \Delta T_{cw}} \quad (4.6)$$

Where Q_{cool} represents the total cooling duty determined from the model. φ_{cw} represents the specific auxiliary power duty obtained from Linnenberg et al. (2011). $c_{p,cw}$ represents the heat capacity of the cooling water. ΔT_{cw} is the temperature rise of the cooling water and is assumed to be 5°C.

The impact of applying the PCC unit on the energy performance of BFPP was assessed using energy and efficiency penalties as evaluation criteria. The energy penalty was determined as the percentage of energy required by PCC relative to the plant's net power output. The efficiency penalty represents the reduction in plant efficiency caused by the implementation of carbon capture. The efficiency calculation utilised a fuel rate of 313.4 t/h and an LHV of 18464 kJ/kg (NETL, 2012).

As summarised in Table 4.2, applying the amine-based PCC process to the BFPP results in an energy penalty ranging from 22% to 31% and an efficiency penalty of 7% to 11%. Among the configurations analysed, the process with AIC-AFS-SSE and HP-sCO_2 (40wt% PZ) achieved the lowest energy consumption, at 121.68 MWe. This corresponds to the lowest energy penalty (22.12%) and efficiency penalty (7.83%). Moreover, for both of the standard PCC cases using 30 wt% and 40 wt% PZ, the optimal lean loading of 0.175 $mol_{CO2}/mol_{Alkalinity}$ is used. According to the results shown in Figure 4.1, at this lean loading, the heat duties of the 30 wt% and 40 wt% PZ cases are nearly identical. Therefore, the overall reboiler heat duty for these two cases is close.

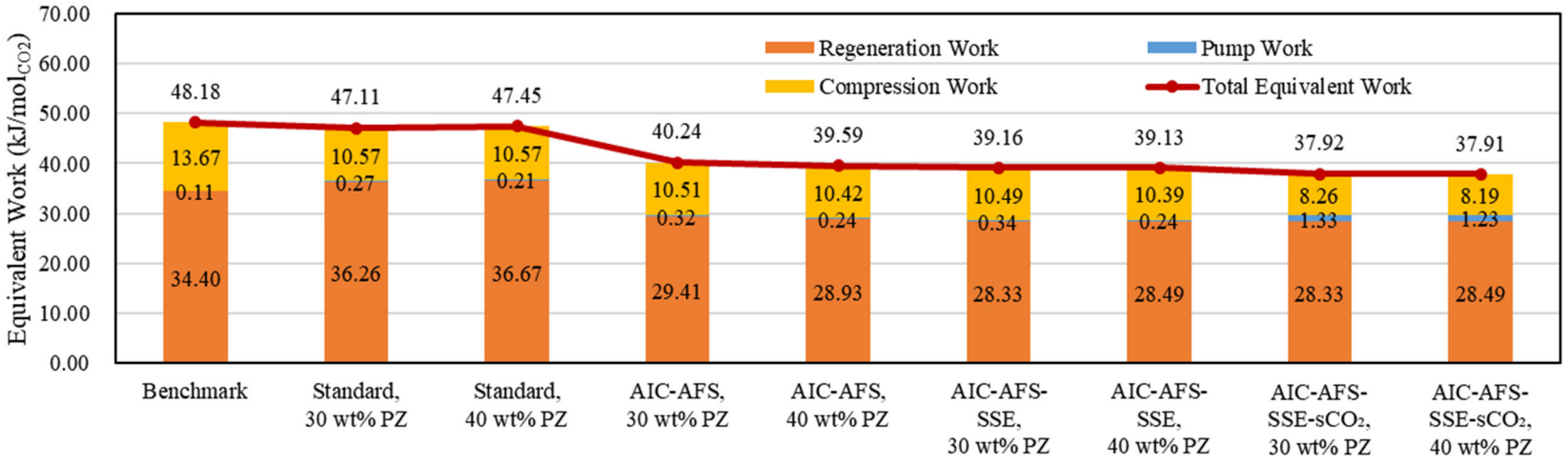

Figure 4.8 Results summary of W_{eq} for different PCC processes

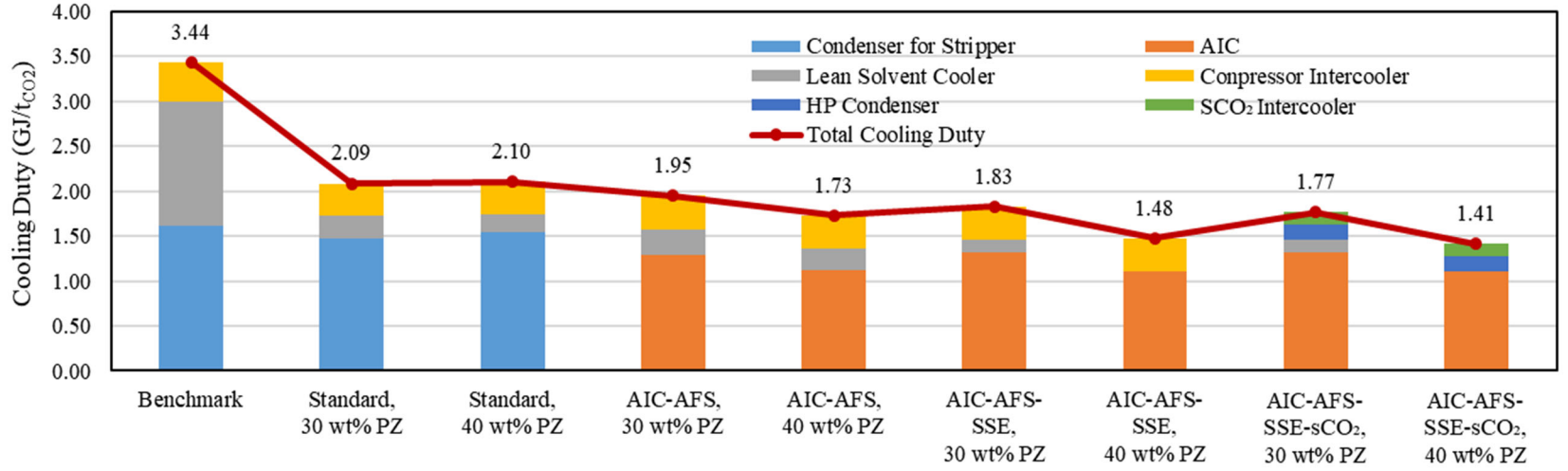

Figure 4.9 Results summary of cooling duty for different PCC processes

Table 4.2 Energy consumption of different PCC components on the BFPP

	BFPP	With standard capture			AIC- AFS		AIC-AFS- SSE		AIC-AFS- SSE -sCO_2	
		30wt%MEA	30wt% PZ	40wt% PZ	30wt%PZ	40wt%PZ	30wt% PZ	40wt% PZ	30wt% PZ	40wt% PZ
Net plant power (MW)	550.0	380.43	390.14	390.19	414.55	417.43	417.06	419.29	426.15	428.32
Net plant efficiency (%)	35.80	24.84	25.47	25.48	27.07	27.26	27.23	27.38	27.83	27.97
CO_2 capture unit										
Rich pump (MW)		0.30	0.82	0.61	0.97	0.72	1.03	0.75	1.03	0.75
Lean pump (MW)		0.030	0.030	0.023	0.011	0.008	0.011	0.008	0.011	0.008
Reboiler (MW)		118.53	121.23	121.34	97.22	95.41	95.03	94.24	95.03	94.25
CO_2 compression unit										
Compressors (MW)		42.09	32.56	32.57	32.36	32.11	32.30	32.01	25.43	25.21
SCO_2 pump (MW)		-	-	-	-	-	-	-	3.05	3.03
SCO_2 turbine (MW)		-	-	-	-	-	-	-	5.13	5.09
Auxiliary										
Cooling water pump (MW)		8.61	5.22	5.27	4.89	4.33	4.57	3.70	4.42	3.53
Total power consumption (MW)		169.57	159.86	159.81	135.45	132.57	132.94	130.71	123.85	121.68
Efficiency penalty (%)		10.96	10.33	10.32	8.73	8.54	8.57	8.42	7.97	7.83
Energy penalty (%)		30.83	29.07	29.06	24.63	24.10	24.17	23.76	22.52	22.12

4.4 Economic analysis

The economic evaluation of PCC processes was conducted using APEA, a reliable tool for detailed cost analysis through a bottom-up estimation approach. APEA utilises Aspen Icarus technology to carry out economic evaluation by estimating equipment costs based on the model design. The overall cost assessment involves CAPEX and OPEX.

The direct cost and total direct cost (TDC) were obtained from the APEA results. The details of the direct cost of each block are presented in Table 4.5. As illustrated in

Figure 4.10, these blocks were classified into the following main components based on their function: absorber, stripper, CO_2 compressors, heat exchangers, cooler or condenser, reboiler or steam heater, pump, and others. From

Figure 4.10, the absorber accounts for the largest percentage of the TDC at 38–45%. The compressor is the second-expensive component of 16–26% of TDC. When comparing using 30wt% PZ solvent with 40wt% PZ under the same configuration, the latter significantly minifies the column size due to its higher capacity, which reduces the solvent flow rate. Additionally, the pump-around AIC increased the absorber's cost by 5–8% as it required additional equipment, including a pump and heat exchanger. After using AFS, the equipment cost was reduced by 0.2 million dollars for the 30wt% PZ case and 0.4 million dollars for the 40wt% PZ case. This is the replacement of the condenser and reboiler in AFS.

For the cases using a standard compression train, the cost of the MEA-based case is higher than PZ because of the difference in stripper pressures between the MEA (1.9 bar) and PZ-based (4.1 bar) PCC. This is attributed to PZ's superior resistance to thermal degradation, enabling it to operate under higher temperatures and pressures. Moreover, using HP-sCO_2 configuration increases the equipment costs by 13 million dollars for the 30wt% PZ process and 16 million dollars for the 40wt% PZ process. This cost increase is primarily driven by higher investments in heat exchangers, as illustrated in

Figure 4.10. In the sCO_2 cycle, additional heat exchangers are used to recover intercooling heat between compressors. However, the economic impact of implementing the sCO_2 cycle should be evaluated alongside its influence on the O&M costs of the entire process.

CAPEX is comprised of direct and indirect costs. Direct costs cover equipment purchase and installation expenses, while indirect costs include construction, engineering and contractor fees, legal expenses, and contingencies (Chauvy et al., 2021). The total CAPEX was estimated following the breakdown method from Li et al. (2016). The equations for calculating the total CAPEX are presented in Table 4.3.

Table 4.3 Equations for calculating the CAPEX (Li et al., 2016)

CAPEX breakdown	Equations
Total indirect cost (TIC)	$\mathrm{TIC} = 20\% * \mathrm{TDC}$
Bare erected cost (BEC)	$\mathrm{BEC} = \mathrm{TDC} + \mathrm{TIC}$
Engineering and contractor (EC)	$\mathrm{EC} = 27\% * \mathrm{BEC}$
Engineering Procurement and construction (EPC)	$\mathrm{EPC} = 127\% * \mathrm{BBC}$
Process contingency (PC)	$\mathrm{PC} = 25\% * \mathrm{BEC}$
Project contingency (PJC)	$\mathrm{PJC} = 20\% * \mathrm{EPC} + 5\% * \mathrm{BEC}$
Total plant cost (TPC)	$\mathrm{TPC} = 120\% * \mathrm{EPC} + 30\% * \mathrm{BEC}$
Owner's cost (OC)	$\mathrm{OC} = 15\% * \mathrm{TPC}$
CAPEX	$\mathrm{CAPEX} = 115\% * \mathrm{TPC}$

The calculated CAPEX is presented in Table 4.6. Then, the total CAPEX is used to calculate the annualized capital cost (ACC), shown as follows (Otitoju et al., 2021):

$$\mathrm{ACC} = \mathrm{CAPEX} \times \frac{\mathrm{i} \times (1+\mathrm{i})^t}{(1+\mathrm{i})^t - 1} \qquad (4.7)$$

Where i represents the interest rate, assumed to be 10%. t is the project's lifetime, which is assumed to be 20 years.

Table 4.4 Utility price for economic analysis published in June 2023[abcde]

Utility type	Energy price
Electricity ($US/kWh)[a]	0.168
Cooling water ($US/m^3)[b]	0.0521
Make-up water ($US/m^3)[c]	1.52

MEA solvent ($US/ton)[d]	1500
PZ solvent ($US/ton)[e]	8000

[a] price obtained from BLS (2023)

[b] prices obtained from Intratec (2023a)

[c] prices obtained from Intratec (2023b)

[d] prices obtained from Alibaba (2023a)

[e] prices obtained from Alibaba (2023b)

OPEX is categorised into fixed and variable O&M costs. Fixed O&M is assumed to be 3% of the total capital costs, while variable O&M represents the total utility costs (Otitoju et al., 2021). The O&M costs are calculated based on utility consumption from the model and the utility price from Table 4.4.

In this analysis, the CO_2 capture cost (CCC) per tonne of CO_2 is the primary index to determine economic performance. CCC is calculated using the following equation:

$$\mathrm{CCC} = \frac{\mathrm{TAC}}{\mathrm{F_{CO_2,OUT}}} \tag{4.8}$$

Where $F_{CO_2,OUT}$ is the total CO_2 production rate. The total annual cost (TAC) is calculated as:

$$\mathrm{TAC} = \mathrm{ACC} + \text{fixed and variable O\&M} \tag{4.9}$$

The economic performance of various configurations is summarised in Table 4.7, with Figure 4.11 providing a detailed breakdown of the CO_2 capture cost. The results indicate that a more complex process leads to increased equipment costs and a higher ACC. Additionally, the largest expenditure is O&M costs, particularly variable O&M costs, which make up more than 80% of TAC. Among these, electricity costs are the most significant, followed by cooling water costs. The economic analysis reveals that implementing AIC- AFS reduces the CCC by 12.6% and 15.1% for the 30wt% and 40wt% PZ cases, respectively. As illustrated in Figure 4.11, this cost reduction is primarily driven by a decrease in variable O&M costs, especially electricity expenses, without substantially increasing CAPEX. Additionally, the SSE configuration achieved a modest reduction in CCC. Due to a lower energy penalty and electricity consumption, using HP-sCO_2 for CO_2 compression can contribute to approximately 3% cost savings despite a 15% rise in CAPEX.

Table 4.5 Direct equipment cost of the large-scale PCC process for 550 MWe BFPP

Unit (M$)	With standard capture			With AIC and AFS		With AIC, AFS and SSE		With AIC, AFS, SSE and sCO_2	
	30wt%MEA	30wt%PZ	40wt%PZ	30wt%PZ	40wt%PZ	30wt%PZ	40wt%PZ	30wt%PZ	40wt%PZ
Absorber	41.40	37.31	33.79	39.16	36.57	39.16	36.17	39.16	36.17
Lean pump	1.49	1.50	0.93	1.48	0.92	1.50	0.92	1.50	0.92
Compressor	26.64	17.06	17.10	17.00	17.04	17.00	17.04	16.40	16.33
Compression intercooler	1.27	1.24	1.24	1.24	1.24	1.24	1.24	0.99	0.99
Rich pump	1.71	1.78	1.13	1.83	1.19	1.93	1.27	1.93	1.27
Flash separator	0.46	0.42	0.42	-	-	-	-	-	-
Condenser	1.82	0.65	0.66	-	-	-	-	-	-
Stripper reboiler	2.52	3.03	3.10	-	-	-	-	-	-
Reflux pump	0.10	0.10	0.10	-	-	-	-	-	-
Stripper	18.74	14.95	14.30	17.26	14.32	17.03	14.12	17.03	14.12
Lean cooler	1.58	0.45	0.28	0.45	0.32	0.37	0.20	0.37	0.20
Main heat exchanger	4.16	5.30	3.58	-	-	-	-	-	-
Absorber intercooler	-	-	-	1.67	1.53	1.68	1.51	1.68	1.51
Cold-cross exchanger	-	-	-	0.82	0.61	0.22	0.25	0.22	0.25

Hot-cross exchanger	-	-	-	4.87	2.72	5.48	3.64	5.48	3.64
Cold-rich exchanger	-	-	-	0.98	0.81	1.04	0.94	1.04	0.94
SSE heat exchanger	-	-	-	-	-	0.46	0.35	0.46	0.35
Steam heater	-	-	-	2.58	2.58	2.48	2.47	2.48	2.47
Flash tank	-	-	-	0.43	0.44	0.43	0.44	0.43	0.44
SCO_2 heat exchangers	-	-	-	-	-	-	-	5.91	8.47
HP evaporator	-	-	-	-	-	-	-	2.83	2.79
HP condenser	-	-	-	-	-	-	-	0.74	0.77
HP compressor	-	-	-	-	-	-	-	1.88	1.88
SCO_2 pump	-	-	-	-	-	-	-	1.42	1.39
SCO_2 turbine	-	-	-	-	-	-	-	1.28	1.27
Total direct cost (M$)	101.87	83.78	76.61	89.78	80.30	90.00	80.57	103.20	96.16

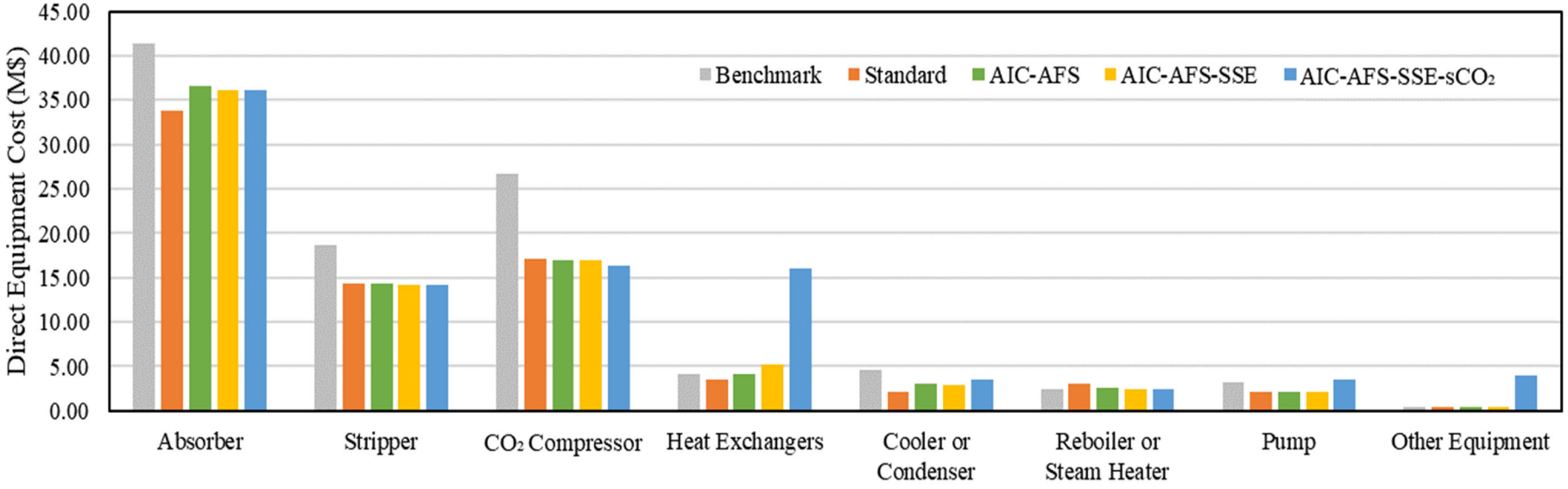

Figure 4.10 Summary of main components' direct cost (40wt% PZ)

Table 4.6 The results of the CAPEX of the large-scale PCC-CCU process for a 550 MWe BFPP

		With standard capture		With IC and AFS		With IC, AFS and SSE		With IC, AFS, SSE and sCO_2	
	30wt%MEA	30wt%PZ	40wt%PZ	30wt%PZ	40wt%PZ	30wt%PZ	40wt%PZ	30wt%PZ	40wt%PZ
TDC (M$)	101.87	83.78	76.61	89.78	80.30	90.00	80.57	103.20	96.16
TIC (M$)	20.37	16.76	15.32	17.96	16.06	18.00	16.11	20.64	19.23
BEC (M$)	122.24	100.53	91.93	107.73	96.36	108.00	96.68	123.84	115.39
EC (M$)	33.01	27.14	24.82	29.09	26.02	29.16	26.10	33.44	31.16
EPC (M$)	155.25	127.68	116.75	136.82	122.37	137.16	122.79	157.28	146.55
PC (M$)	30.56	25.13	22.98	26.93	24.09	27.00	24.17	30.96	28.85
PJC (M$)	37.16	30.56	27.95	32.75	29.29	32.83	29.39	37.65	35.08
TPC (M$)	222.97	183.37	167.69	196.51	175.75	197.00	176.35	225.88	210.47
OC (M$)	33.45	27.51	25.15	29.48	26.36	29.55	26.45	33.88	31.57
CAPEX(M$)	256.41	210.88	192.84	225.98	202.12	226.55	202.80	259.76	242.04

Table 4.7 Summary of the economic performance of different PCC processes

	With standard capture			With IC and AFS		With IC, AFS and SSE		With IC, AFS, SSE for PCC and sCO_2 for CO_2 compression	
	30wt%MEA	30wt%PZ	40wt%PZ	30wt%PZ	40wt%PZ	30wt%PZ	40wt%PZ	30wt%PZ	40wt%PZ
ACC (M$/yr)	30.1	24.8	22.7	26.5	23.7	26.6	23.8	30.5	28.4
Fixed operating (M$/yr)	7.7	6.3	5.8	6.8	6.1	6.8	6.1	7.8	7.3
Variable operating (M$/yr):									
Electricity	227.9	214.9	214.9	182.0	178.2	178.7	175.7	166.5	163.5
Cooling water	33.5	21.6	21.0	19.9	17.1	19.3	15.3	18.6	14.6
H_2O make-up	1.5	2.9	3.1	5.0	4.8	5.1	5.6	5.0	5.4
MEA/PZ make-up	0.6	1.3	2.7	2.5	4.6	2.7	5.1	2.7	5.1
TAC (M$/yr)	301.2	271.8	270.1	242.7	234.5	239.2	231.6	231.2	224.4
CCC ($/$t_{CO2}$)	77.2	69.7	69.2	62.2	60.1	61.3	59.4	59.3	57.5

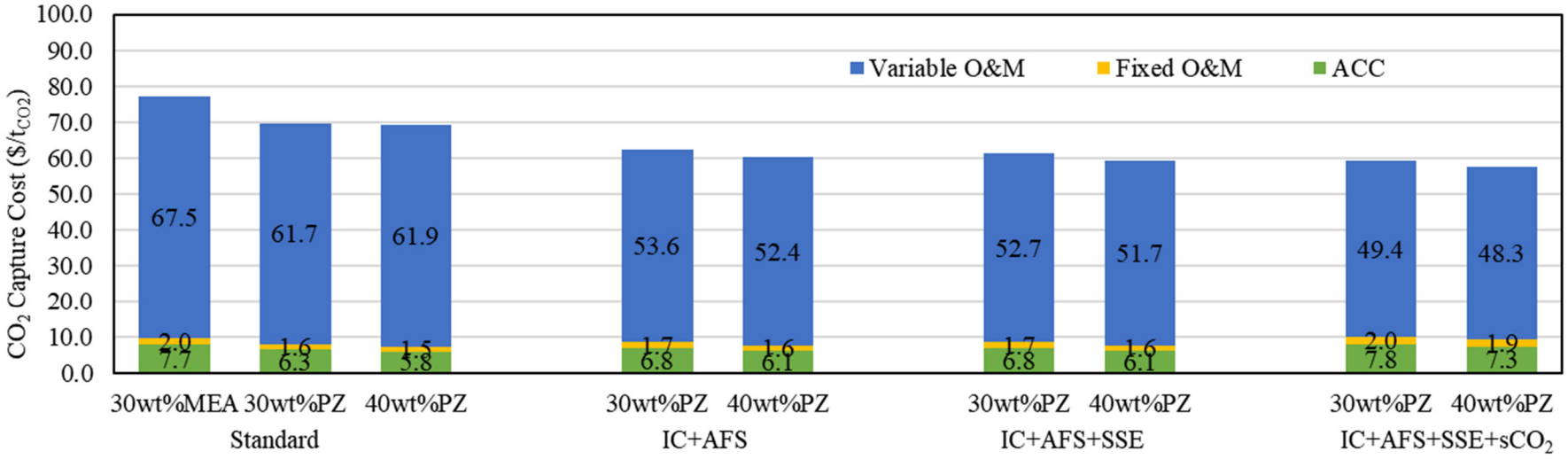

Figure 4.11 Breakdown of CCC for different PCC processes

4.5 Optimisation of PZ-based PCC process

4.5.1 Optimisation of PZ concentration for the PZ-based PCC process

Solvent concentration plays a vital role in influencing CO_2 solubility and the energy required for solvent regeneration (Luo, 2016). Process optimisation was conducted using the built-in sequential quadratic programming (SQP) algorithm in Aspen Plus® V11 to identify the optimal PZ concentration with the minimum CCC.

The objective function of the optimisation is to minimise CCC. The constraints for the optimisation included maintaining a CO_2 capture rate of 90% and varying the PZ concentration between 30 and 40wt%. The decision variables considered were the solvent regeneration heat duty and the solvent flow rate.

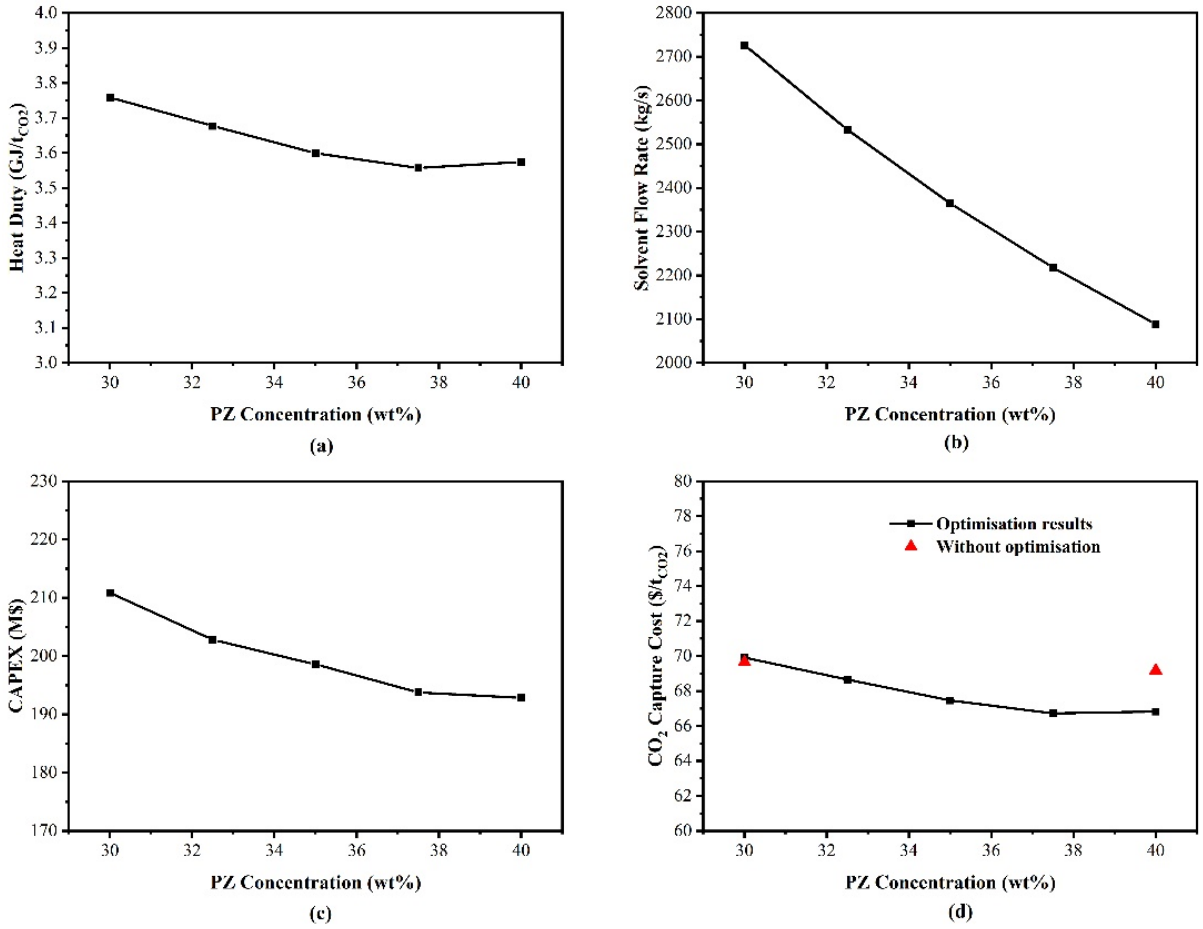

Figure 4.12 Optimisation of CCC varying PZ concentrations (standard PCC)

The optimisation results for the PCC process with the standard design are illustrated in Figure 4.12. As shown in Figure 4.12(b), a higher concentration of PZ solvent enhances CO_2 solubility

and decreases the solvent flow rate. With a constant flue gas inlet flow rate, a lower solvent flow rate leads to a lower L/G ratio and thus reduces the column size. This results in a lower CAPEX, as illustrated in Figure 4.12(c). Additionally, increasing the PZ concentration from 30wt% to 40wt% showed a diminishing return in reducing the reboiler duty, as indicated in Figure 4.12(a). In the PCC process, reboiler duty is the largest source of energy consumption and is a key contributor to overall O&M costs. The optimisation results of CCC were compared to the non-optimized cases, as presented in Figure 4.12(d). Considering both O&M and CAPEX costs, the CCC progressively decreases as the PZ concentration increases from 30wt% to 37.5wt% but shows minimal change when the concentration ranges from 37.5wt% to 40wt%. Therefore, 37.5wt% PZ is considered the optimal concentration for the standard PCC. In addition, the optimisation achieved a cost reduction of 2.3 $/$t_{CO2}$ for the 40wt% PZ case, but no significant cost savings were observed for the 30wt% PZ case.

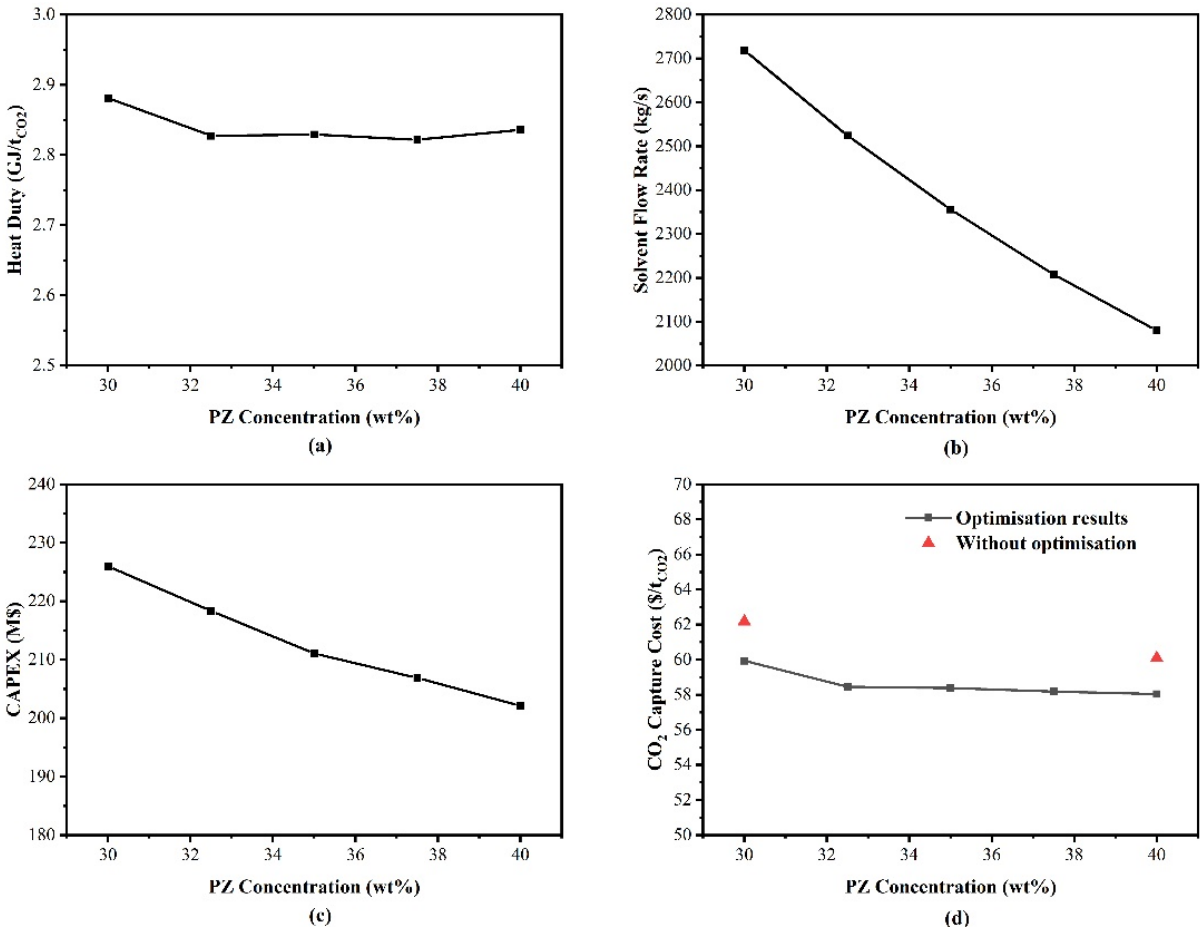

Figure 4.13 Optimisation of CCC varying PZ concentrations (AIC-AFS configuration)

The optimisation results for the AIC-AFS configuration are illustrated in Figure 4.13, showing

trends similar to the standard configuration. Figure 4.13(d) indicated that increasing the PZ concentration from 30wt% to 32.5wt% resulted in a reduction of CCC by 1.5$/$t_{CO2}$. When the PZ concentration exceeded 32.5wt%, no massive change in CCC was shown. Consequently, 32.5wt% PZ is recommended for the AIC-AFS configuration. Additionally, this optimisation obtained a cost reduction of 2.2$/$t_{CO2}$ and 2.0$/$t_{CO2}$ for the 30wt% and 40wt% PZ cases with the AIC-AFS design, respectively.

4.5.2 Optimisation of stripper pressure for the PZ-based PCC process with AIC-AFS configuration

PZ has greater resistance to thermal degradation compared to MEA, allowing it to function at higher stripper pressures and temperatures. In a pilot plant test conducted at NCCC, stripper pressures ranging from 5.5 to 7.35 bar were used with the AFS configuration and PZ solvent (Gao et al., 2019)This optimisation study evaluates the economic performance of the PZ-based AIC-AFS configuration under high stripper pressure. The PZ concentration of 32.5wt% was selected based on the findings from Section 4.5.1.

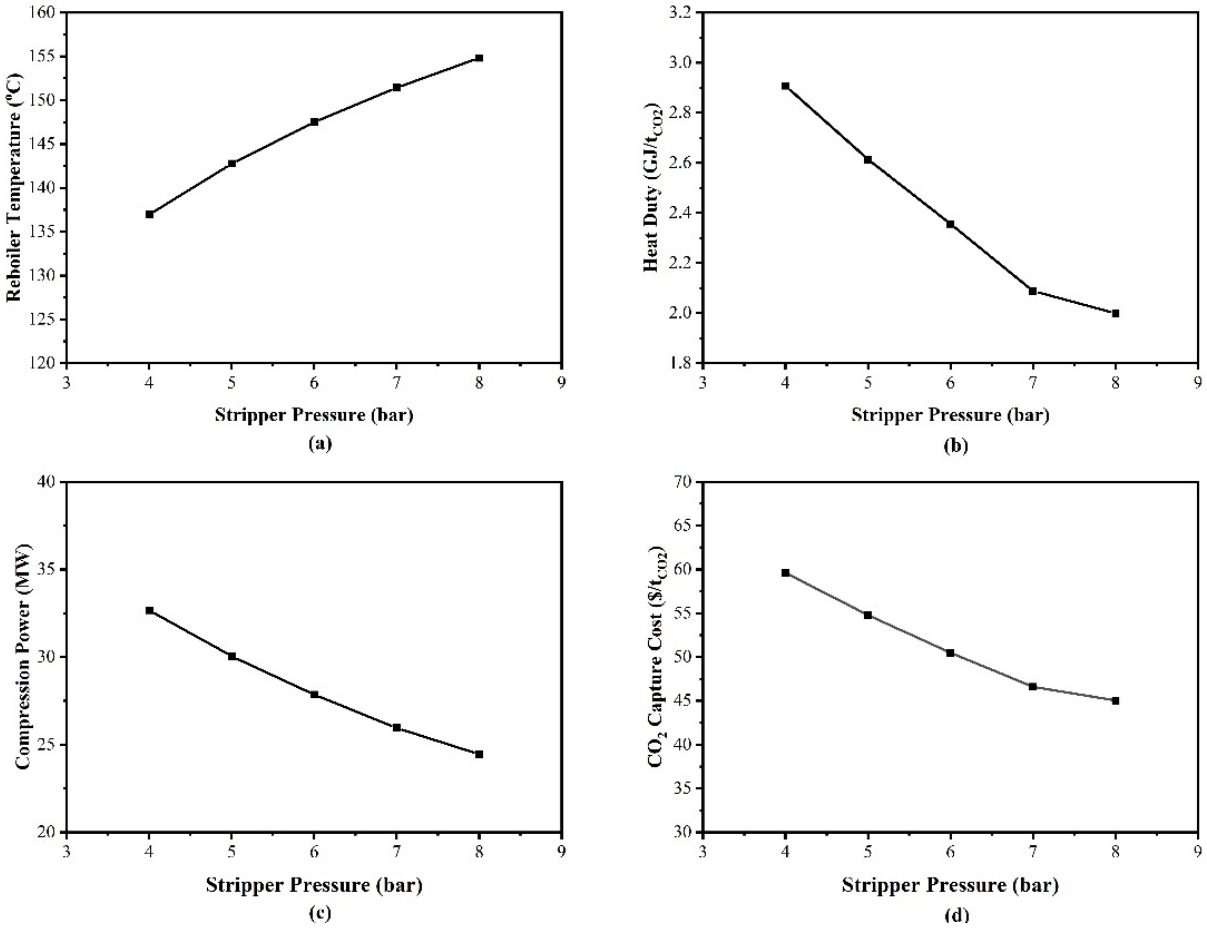

Figure 4.14 Optimisation results of CCC varying stripper pressures (AIC-AFS configuration)

As illustrated in Figure 4.14(a), increasing the stripper pressure from 4 bar to 8 bar caused the stripper sump temperature to increase by 18 °C. This also led to a heat duty decrease of 31% (Figure 4.14(b)). A higher stripper pressure reduces heat duty by inhibiting the vaporisation of water, thereby cutting down the latent heat penalty. Additionally, as presented in Figure 4.14(c), increasing stripper pressure can lower the energy demand during the CO_2 compression stage. However, achieving higher stripper pressures requires more pumping power. The combined impact of increasing stripper pressure on CCC is presented in Figure 4.14(d). It indicated that raising the stripper pressure from 4 to 8 bar can lower CCC by \$14.6/t_{CO2}. As suggested by Rochelle et al. (2019), steam temperatures exceeding 150 °C would need a thicker column wall. Therefore, a stripper pressure of 7 bar is recommended in this work.

4.6 Conclusion

In this chapter, the sensitivity analysis was conducted to evaluate the impact of key parameters on the energy performance for the different configurations described in Section 3.4. Energy consumption and cost are the two key metrics used to determine the performance of the PCC process. The energy analysis was carried out to investigate the energy and efficiency penalty associated with integrating the PCC process with the BFPP. Subsequently, the economic analysis for the nine cases was carried out using APEA®. Additionally, the optimisation of solvent concentration and stripper pressure was performed to identify the most cost-effective operating conditions. The conclusions of this chapter are as follows:

- The sensitivity analysis determined the best operating conditions for each configuration for PZ concentrations of 30wt% and 40wt%, including the lean loading, absorber packing height, split ratio (for PCC process using AFS configuration) and the sCO_2 turbine pressure ratio (for CO_2 compression with HP-sCO_2 configuration).
- An energy analysis showed that using 40wt% PZ reduced the reboiler duty by 0.21 GJ/t_{CO2} for the standard PCC process compared to the benchmark. Moreover, the configuration AIC-AFS-SSE, combined with 40wt% PZ solvent, showed the minimum heat duty of 2.78 GJ/t_{CO2} among the nine cases. Applying a compressor with HP-sCO_2 resulted in the lowest equivalent work of 37.91 kJ/mol_{CO2}, corresponding to the lowest

energy penalty (22.1%) and efficiency penalty (7.8%).

- The results of the economic analysis indicated that the configuration with AIC-AFS-SSE-sCO_2 using 40wt% PZ had the lowest CCC, calculated at $57.5 for capturing per tonne of CO_2. This represents a 17% reduction compared to the standard case using 40wt% PZ, which had a capture cost of $69.2 per tonne of CO_2.
- From the results of Section 4.5, in the optimisation of PZ concentrations, it is indicated that the ideal PZ concentrations are 37.5wt% for the standard configuration and 32.5wt% for the AIC-AFS configuration. In the optimisation of stripper pressure using the optimal PZ concentration with AIC-AFS, the results showed that 7 bar was recommended, considering the capture cost and the material tolerance. At this pressure, a heat duty of 2.09 GJ/t_{CO2} and a CO_2 capture cost of 46.6$/$t_{CO2}$ were achieved. These results represent a 41.6% reduction in energy requirement and a 32.4% decrease in cost compared to the standard 40wt% PZ case.

Chapter 5 Energy and exergy analysis of supercritical BFPP integrated with solvent-based PCC

5.1 Overview

This chapter discussed the energy and exergy performance of BFPP integrated with PCC with different configurations carried out in Aspen Plus®. In Section 5.2, the optimised PCC process with AIC-AFS configuration using 32.5wt% PZ as the solvent proposed in Chapter 4 was linked to the 550 MWe supercritical BFPP. The thermodynamic performance of this process was compared with the BFPP integrated standard PCC process using 30wt% MEA and 40wt% PZ. Section 5.2 describes these integrated designs. Section 5.3 and Section 5.4 compared the energy and exergy performance of various integrated processes. The key findings of the thermodynamic analysis are provided in Section 5.5.

5.2 Integration of the 550 MWe supercritical BFPP and the large-scale solvent-based PCC

Error! Reference source not found. illustrates the integration design of BFPP with various large-scale PCC processes. Figure 5.2 presents the subsystems within each hierarchy. When integrating PCC with the BFPP, the flue gas after the pollutant control system is sent to PCC, which is cooled down to 40^{o}C by a direct contact cooler (Gao and Rochelle, 2020). For standard MEA-based PCC, the steam extracted from the IP–LP crossover (at 9.3 bar, 379 ^{o}C) is cooled down to 131 °C (Linnenberg et al., 2011). The corresponding reboiler temperature is 123 °C, consistent with pilot plant data reported by Notz et al. (2012), Case 9. For the PZ-based PCC cases, the steam is cooled down to 178 ^{o}C, as reported by Rochelle et al. (2019). For standard PZ-based PCC systems, the reboiler temperature is 139 °C. In the AFS configuration using PZ solvent, the reboiler temperature reaches 151 °C. This is to prevent the solvent's thermal degradation. Then, this steam is used to provide heat for solvent regeneration.

The following three cases are studied:

- Case 1: 550 MWe supercritical BFPP integrated with the large-scale standard PCC process using 30wt% MEA.
- Case 2: 550 MWe supercritical BFPP integrated with the large-scale standard PCC process

using 40wt% PZ.

- Case 3: 550 MWe supercritical BFPP integrated with the large-scale PCC with AIC-AFS configuration using 32.5wt% PZ.

For Cases 1 and 2, the operating conditions of the standard PCC process using 30wt% MEA and 40wt% PZ presented in Table 4.1 are applied. For Case 3, the optimised PCC with AIC-AFS configuration using 32.5wt% PZ indicated in Section 4.5.2 is used.

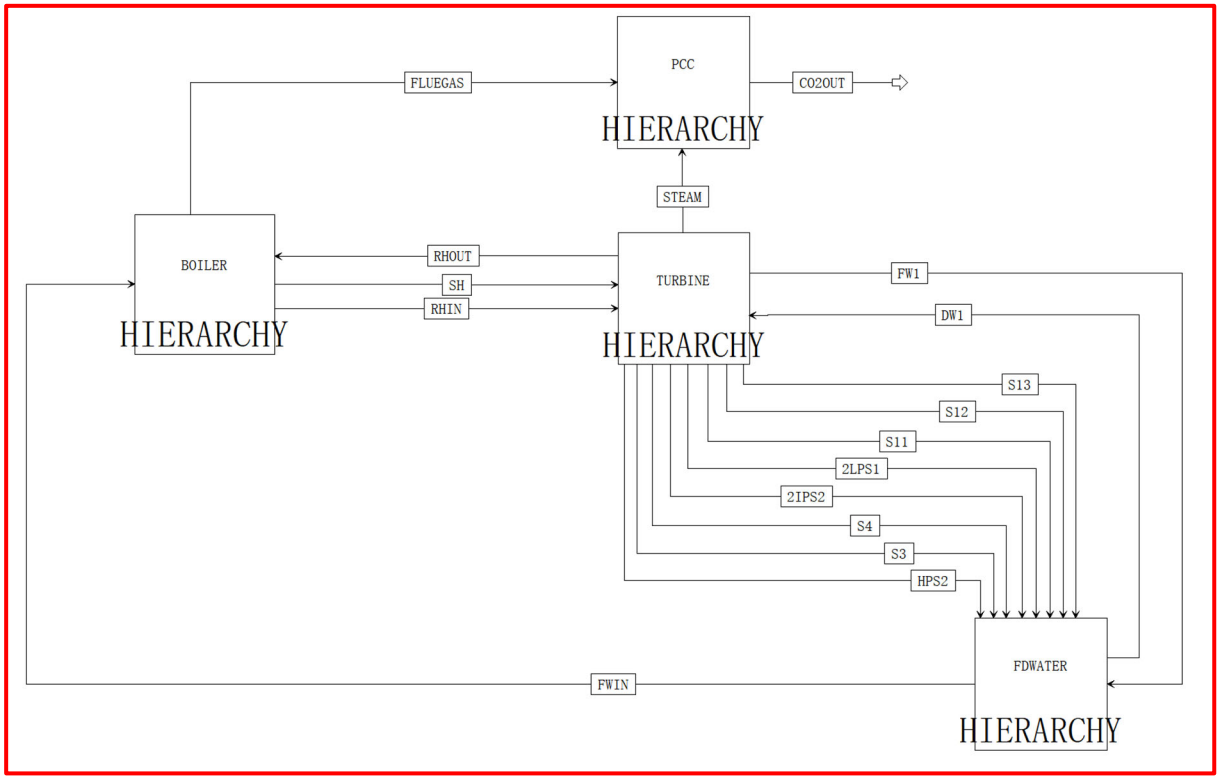

Figure 5.1 Integration of BFPP with PCC

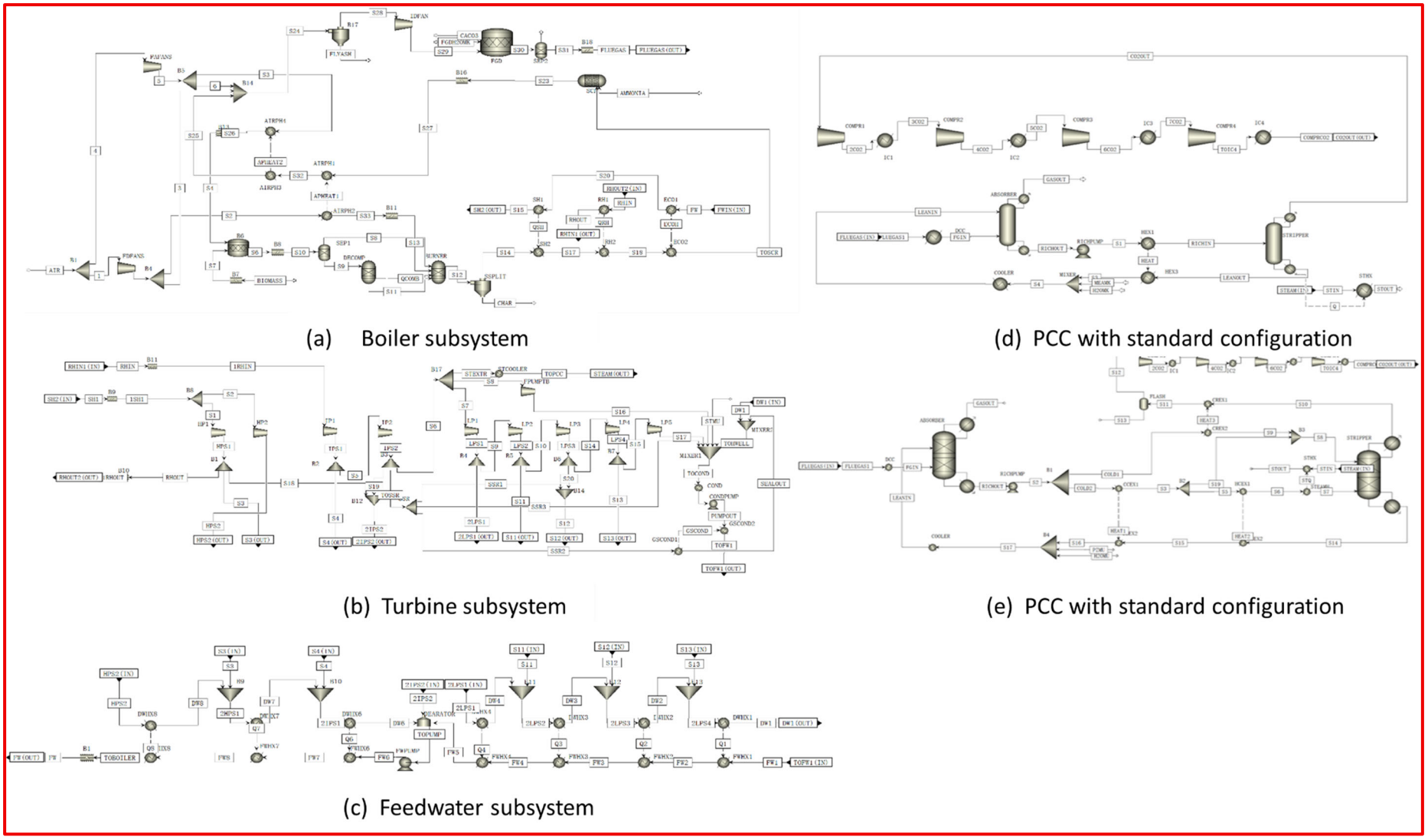

Figure 5.2 Subsystems contained within each hierarchy of the integrated BFPP–PCC system

5.3 Energy analysis of different integration designs

The energy performance of BFPP with/without PCC integration was compared in Table 5.1. The turbine power output refers to the total power output from the HP, IP, and LP turbines for different integration processes. The net power output is the turbine power output minus the PCC pumping power and CO_2 compression power. The total energy penalty caused by adding PCC includes the power consumption from steam extraction, pumping power and CO_2 compression power. From the results, steam extraction for solvent regeneration ($P_{loss,steam}$) is the largest source of power consumption caused by PCC. The $P_{loss,steam}$ is calculated as the turbine power penalty compared with BFPP without PCC. Because the steam is extracted from the IP–LP crossover, this turbine power penalty is only found in the LP turbine.

In Section 4.3, PCC is not integrated into BFPP and this $P_{loss,steam}$ is estimated using a power loss factor. Compared with the results of Section 4.3, the calculated $P_{loss,steam}$ after integration with the PCC process using 30wt% MEA and 40wt% PZ are 32.3 MW and 28.3 MW higher, respectively. This difference is caused by the steam cooling before sending it to the PCC subsystem.

In addition, the CO_2 compression unit is the second largest energy-consuming component in PCC. The stripper pressures for Cases 1, 2 and 3 are 1.9 bar, 4.1 bar, and 7 bar, respectively. This stripper pressure is limited by the thermal stability of the solvent. The high stripper pressure leads to the high inlet pressure of the CO_2 compression train, which would reduce the compression duty. Therefore, the compression power for the three cases is 42.1 MW, 32.6 MW and 25.7 MW.

Among the three cases, Case 3 showed the lowest energy penalty of 22.4% and efficiency penalty of 7.8%. It showed energy and efficiency savings of 13.0% and 4.5 % compared to the case of the standard PCC process using 40wt% PZ.

Table 5.1 Energy consumption of BFPP integrated with different PCC processes

	BFPP	Standard PCC		AIC-AFS
		30wt%MEA	40wt%PZ	32.5wt%PZ
Turbine power output (MW)	550.8	400.0	401.1	463.4

HP turbine (MW)	172.7	172.7	172.7	172.7
IP turbine (MW)	168.0	168.0	168.0	168.0
LP turbine (MW)	210.1	59.3	60.5	122.7
PCC Pumping power (MW)	N/A	8.9	5.9	3.4
CO_2 compression power (MW)	N/A	42.1	32.6	25.7
Steam extraction (MW)	N/A	150.8	149.6	87.4
Net plant power output (MW)	550.8	349.0	362.7	434.3
Net plant efficiency (%)	34.9%	22.1%	23.0%	27.5%
Total power consumption (MW)	N/A	201.8	188.1	116.5
Energy penalty (%)	N/A	36.6%	34.2%	21.2%
Efficiency penalty (%)	N/A	12.8%	11.9%	7.4%

5.4 Exergy analysis of different integration designs

Exergy analysis is a crucial part of thermodynamic analysis for power plants as well as carbon capture systems, as it quantifies the work potential and penalty of the system in energy conversion processes. The exergy analysis for different BFPP integrated with PCC designs is carried out based on the model described in Section 5.2 through Aspen Plus® V11. Aspen Plus® has three property sets for exergy calculation, which include EXERGYMS, EXERGYML and EXERGYFL for calculating exergy on mass, molar and flow basis, respectively (Gray, 2019). These property sets are used to estimate the exergy of material or energy flows based on a defined reference state (Olaleye, 2015). The reference state is defined by the atmospheric or equilibrium conditions of pressure and temperature (Gray, 2019). In this work, the exergy of each flow is predicted using the EXERGYFL property set, with the default reference state at 25°C (298 K) and 1 atm (101.325 kPa). As exergy of flow is defined relative to the chosen reference environment, using a different reference state would change the calculated values of the exergy of individual flows. However, the exergy destruction within a system depends on the difference between inlet and outlet exergies. Therefore, the overall exergy destruction and exergy efficiency calculations remain unaffected by the choice of reference state, provided it is applied consistently throughout the system. The exergy balance for each component is described using the following equation (Jana and De, 2015):

$$\sum \dot{E}x_{in,n} + \dot{E}x_{Q,n} = \sum \dot{E}x_{out,n} + \dot{E}x_{W,n} + \dot{E}x_{D,n} \quad (5.1)$$

Where $\dot{E}x_{in,n}$ is the exergy rate of the inlet flow for component n, $\dot{E}x_{Q,n}$ is the exergy rate for heating or cooling, $\dot{E}x_{out,n}$ is the exergy rate of the outlet flow for component n, $\dot{E}x_{W,n}$ is the exergy rate for work, $\dot{E}x_{D,n}$ is the exergy destruction for component n.

The overall exergy consists of the chemical ($\dot{E}x_{Chem}$) and physical exergies ($\dot{E}x_{Phy}$), which is calculated as:

$$\dot{E}x = \dot{E}x_{Chem} + \dot{E}x_{Phy} \quad (5.2)$$

For a multi-component stream, the exergy flow rate of species i ($\dot{E}x_i$) is determined by:

$$\dot{E}x_i = m_i ex_i \quad (5.3)$$

Where m_i is the flow rate of species i, ex_i is the specific exergy of species i.

The specific chemical (ex_{Chem}) and physical (ex_{Phy}) exergies are obtained using the following equations (Lak Kamari et al., 2023):

$$ex_{Chem} = \sum_{i=1}^{n} x_i ex_{Chem,i} + RT_0 \sum_{i=1}^{n} x_i \ln x_i \quad (5.4)$$

$$ex_{Phy} = (h - h_0) - T_0(s - s_0) \quad (5.5)$$

Where T_0 is the temperature at the default reference state, x_i is the mass fraction of component i, h_0 and s_0 are enthalpy and entropy at the reference state and can be obtained from simulation.

And the $\dot{E}x_Q$ and $\dot{E}x_W$ are obtained by the following equations (Jana and De, 2015):

$$\dot{E}x_{Q,n} = \left(1 - \frac{T_0}{T_{h,n}}\right) Q_{h,n} \quad (5.6)$$

$$\dot{E}x_{W,n} = W_n \quad (5.7)$$

The chemical exergy of the biomass fuel ($\dot{E}x_{Q,Fuel}$) is calculated as (Lak Kamari et al., 2023):

$$\dot{E}x_{Q,Fuel} = \beta m_{Bio} LHV_{Bio} \quad (5.8)$$

Where β is a factor representing the ratio of the LHV to the chemical exergy of the fuel's organic content. It is calculated using the following correlation presented in Szargut et al. (1987)

$$\beta = \frac{1.0414 + 0.0177\frac{H}{C} - 0.3328\frac{O}{C}(1 + 0.0537\frac{H}{C})}{1 - 0.4021\frac{O}{C}} \quad (5.9)$$

Where C, H, O represent the mass fractions of these elements in biomass.

The general exergy efficiency $\dot{\varepsilon}$ is calculated using the following equation (Lak Kamari et al., 2023):

$$\dot{\varepsilon} = \frac{\sum \text{useful output exergy}}{\sum \text{input exergy}} \quad (5.10)$$

The detailed equations used for calculating exergy destruction and efficiency of each component are summarised in Table 5.2.

Table 5.2 Summary of equations for calculating exergy destruction and efficiency (Jana and De, 2015; Lak Kamari et al., 2023; Olaleye, 2015)

Components	Equations
Fan (PA, FD and ID fans)	$\dot{E}x_{D,Fan} = \dot{E}x_{in,Fan} - \dot{E}x_{out,Fan} + \dot{E}x_{W,Fan}$
	$\varepsilon_{Fan} = \frac{\dot{E}x_{out,Fan} - \dot{E}x_{in,Fan}}{\dot{E}x_{W,Fan}}$
Heat exchanger (heaters and coolers)	$\dot{E}x_{D,HX} = \sum \dot{E}x_{in,HX} - \sum \dot{E}x_{out,HX}$
	$\varepsilon_{HX} = \frac{(\dot{E}x_{out,HX} - \dot{E}x_{in,HX})_{cold}}{(\dot{E}x_{in,HX} - \dot{E}x_{out,HX})_{hot}}$
Burner	$\dot{E}x_{D,Burner} = \sum \dot{E}x_{in,Burner} - \dot{E}x_{out,Burner} + \dot{E}x_{Q,Fuel}$

	$\varepsilon_{\text{Burner}} = \frac{\dot{\text{Ex}}_{\text{out,Burner}} - \sum \dot{\text{Ex}}_{\text{in,Burner}}}{\dot{\text{Ex}}_{\text{Q,Fuel}}}$
Pump	$\dot{\text{Ex}}_{\text{D,Pump}} = \dot{\text{Ex}}_{\text{in,Pump}} - \dot{\text{Ex}}_{\text{out,Pump}} + \dot{\text{Ex}}_{\text{W,Pump}}$
	$\varepsilon_{\text{Pump}} = \frac{\dot{\text{Ex}}_{\text{out,Pump}} - \dot{\text{Ex}}_{\text{in,Pump}}}{\dot{\text{Ex}}_{\text{W,Pump}}}$
Turbine (HP, IP, LP turbines and FPUMPTB)	$\dot{\text{Ex}}_{\text{D,Turb}} = \dot{\text{Ex}}_{\text{in,Turb}} - \dot{\text{Ex}}_{\text{out,Turb}} - \dot{\text{Ex}}_{\text{W,Turb}}$
	$\varepsilon_{\text{Turb}} = \frac{\dot{\text{Ex}}_{\text{W,Turb}}}{\dot{\text{Ex}}_{\text{in,Turb}} - \dot{\text{Ex}}_{\text{out,Turb}}}$
Absorber	$\dot{\text{Ex}}_{\text{D,Abs}} = \sum \dot{\text{Ex}}_{\text{in,Abs}} - \sum \dot{\text{Ex}}_{\text{out,Abs}} - \dot{\text{Ex}}_{\text{Q,Abs}}$
	$\varepsilon_{\text{Abs}} = 1 - \frac{\dot{\text{Ex}}_{\text{D,Abs}}}{\sum \dot{\text{Ex}}_{\text{in,Abs}}}$
Stripper	$\dot{\text{Ex}}_{\text{D,Stp}} = \sum \dot{\text{Ex}}_{\text{in,Stp}} - \sum \dot{\text{Ex}}_{\text{out,Stp}}$
	$\varepsilon_{\text{Stp}} = \frac{(\dot{\text{Ex}}_{\text{out,Stp}} - \dot{\text{Ex}}_{\text{in,Stp}})_{\text{cold}}}{(\dot{\text{Ex}}_{\text{in,Stp}} - \dot{\text{Ex}}_{\text{out,Stp}})_{\text{hot}}}$
Compressors	$\dot{\text{Ex}}_{\text{D,Comp}} = \dot{\text{Ex}}_{\text{in,Comp}} - \dot{\text{Ex}}_{\text{out,Comp}} + \dot{\text{Ex}}_{\text{W,Comp}}$
	$\varepsilon_{\text{Comp}} = \frac{\dot{\text{Ex}}_{\text{out,Comp}} - \dot{\text{Ex}}_{\text{in,Comp}}}{\dot{\text{Ex}}_{\text{W,Comp}}}$

Figure 5.3 illustrates the distribution of exergy destruction in each subsystem. The detailed exergy destructions and efficiencies for each component are provided in Table 5.3, Table 5.4, Table 5.5 and Table 5.6 for BFPP only, Cases 1, 2 and 3, respectively.

As indicated in Figure 5.3(a), the boiler is the largest source of exergy destruction in the power plant, accounting for 88% of the total exergy destruction. This exergy destruction is mainly from the burner (shown in Table 5.3), where combustion occurs, resulting in the highest irreversibility in the boiler subsystem. The turbine subsystem accounts for the second largest share of exergy destruction, which mainly comes from the HP turbine, IP turbine and

FPUMPTB. These turbines operate at high pressures and temperatures, also with high-pressure drop, and thus, irreversibility due to expansion processes is more significant.

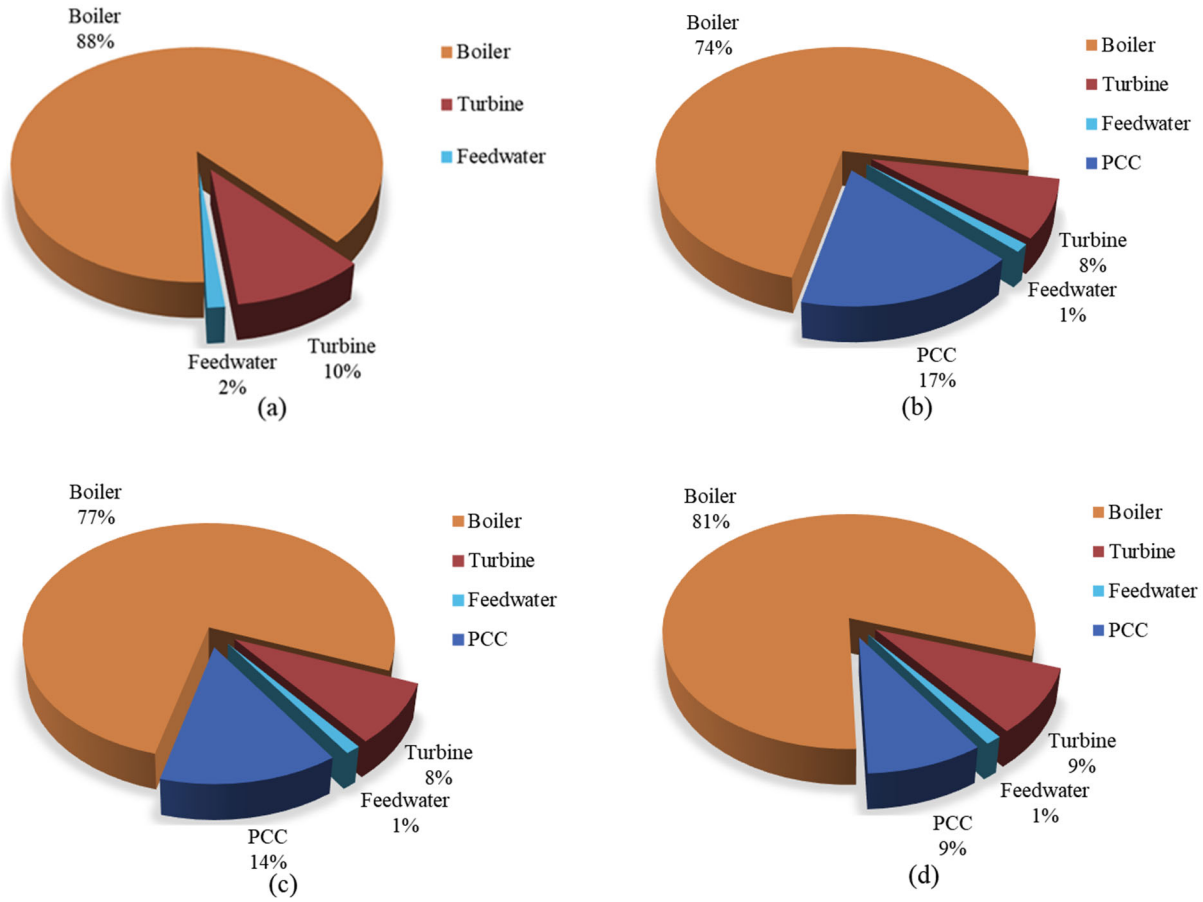

Figure 5.3 Exergy destruction distribution of each subsystem for (a) BFPP, (b) Case 1: BFPP integrated with standard PCC process using 30wt% MEA, (c) Case 2: BFPP integrated with standard PCC process using 40wt% PZ and (d) Case 3: BFPP integrated with PCC with AIC using 32.5wt% PZ

Figure 5.3(b) illustrates the exergy destruction distribution after combining standard PCC process using MEA. From the results, PCC becomes the second largest source of exergy destruction (17%), followed by the turbine subsystem (8%) and feedwater subsystem (1%). The majority of the exergy destruction comes from the reboiler of the stripper due to the solvent regeneration process.

Compared with PCC process using 30wt% MEA in Case 1, using 40wt% PZ can reduce the exergy destruction of the PCC subsystem by 22.3% (54.5 MW), as illustrated in Table 5.5 and

Figure 5.3(c). This is attributed to the lower solvent flow rate demand for using PZ than MEA because of PZ's higher absorption capacity.

Figure 5.3(d) illustrates the exergy destruction of Case 3 with AIC-AFS using 32.5wt% PZ. In this AFS configuration, the regeneration heat is not provided by the reboiler. Instead, a partially vaporised steam heated by a steam heater is used to provide the heat required for solvent regeneration. Compared with Case 2 using standard PCC, Case 3 effectively decreased the exergy of the PCC subsystem by 37.8%, corresponding to 71.8 MW of exergy savings. Through using this optimised PCC process, the percentage of the PCC subsystem was reduced to 9% of the integration system.

Table 5.3 Exergy destruction and efficiency of each component for BFPP

Components	$\dot{E}x_{D,n}$ (MW)	ε (%)	Components	$\dot{E}x_{D,n}$ (MW)	ε (%)	Components	$\dot{E}x_{D,n}$ (MW)	ε (%)
Boiler			LP2	6.55	92.7%	FWHX7	2.58	94.2%
FDFAN	1.10	72.0%	LP3	3.60	91.5%	FWHX8	1.63	95.2%
PAFAN	0.62	72.0%	LP4	6.92	81.9%			
BURNER	752.86	58.0%	LP5	4.55	90.4%			
SH	246.26	68.4%	COND	0.70	97.7%			
RH	16.03	89.8%	CONDPUMP	0.02	96.6%			
ECO	15.33	72.5%	GSCOND	0.16	21.0%			
SCR	3.48	96.5%	STCOOLER	11.11	75.2%			
AIRPRE1	18.33	71.4%	FPUMPTB	46.55	90.8%			
AIRPRE2	4.63	49.8%	***Feedwater***					
IDFAN	0.58	80.7%	FWHX1	1.19	68.2%			
Turbine			FWHX2	0.97	81.5%			
HP1	22.49	87.8%	FWHX3	0.98	86.6%			
HP2	1.14	89.9%	FWHX4	3.71	82.5%			
IP1	18.47	83.1%	DEAERATOR	2.18	96.6%			
IP2	8.97	89.6%	FWPUMP	1.74	90.3%			
LP1	3.32	94.5%	FWHX6	1.38	95.0%			

Table 5.4 Exergy destruction and efficiency of each component for Case 1

Components	$\dot{E}x_{D,n}$ (MW)	ε (%)	Components	$\dot{E}x_{D,n}$ (MW)	ε (%)	Components	$\dot{E}x_{D,n}$ (MW)	ε (%)
Boiler			LP2	1.85	92.7%	FWHX7	2.58	94.2%
FDFAN	1.10	72.0%	LP3	0.90	91.5%	FWHX8	1.63	95.2%
PAFAN	0.62	72.0%	LP4	1.53	81.9%	***PCC***		
BURNER	752.86	58.0%	LP5	0.85	90.4%	DCC	13.86	39.3%
SH	246.26	68.4%	COND	1.62	95.0%	ABSORBER	23.90	33.6%
RH	16.03	89.8%	CONDPUMP	0.10	86.5%	RICHPUMP	6.74	4.7%
ECO	15.33	72.5%	GSCOND	0.19	21.0%	HX	26.88	82.5%
SCR	3.48	96.5%	STCOOLER	11.11	75.2%	STRIPPER	149.34	53.1%
AIRPRE1	18.33	71.4%	FPUMPTB	46.55	90.8%	COOLER	7.10	52.8%
AIRPRE2	4.63	49.8%	***Feedwater***			COMPR1	1.75	85.1%
IDFAN	0.58	80.7%	FWHX1	1.19	68.2%	IC1	1.51	12.3%
Turbine			FWHX2	0.97	81.5%	COMPR2	1.72	85.0%
HP1	22.49	87.8%	FWHX3	0.98	86.6%	IC2	1.51	12.7%
HP2	1.14	89.9%	FWHX4	3.71	82.5%	COMPR3	1.59	85.0%
IP1	18.47	83.1%	DEAERATOR	2.18	96.6%	IC3	1.79	12.7%
IP2	8.97	89.6%	FWPUMP	1.74	90.3%	COMPR4	1.19	85.4%
LP1	1.12	94.5%	FWHX6	1.38	95.0%	IC4	5.16	5.1%

Table 5.5 Exergy destruction and efficiency of each component for Case 2

Components	$\dot{E}x_{D,n}$ (MW)	ε (%)	Components	$\dot{E}x_{D,n}$ (MW)	ε (%)	Components	$\dot{E}x_{D,n}$ (MW)	ε (%)
Boiler			LP2	1.88	92.7%	FWHX7	2.58	94.2%
FDFAN	1.10	72.0%	LP3	0.92	91.5%	FWHX8	1.63	95.2%
PAFAN	0.62	72.0%	LP4	1.58	81.9%	***PCC***		
BURNER	752.86	58.0%	LP5	0.88	90.4%	DCC	13.86	39.3%
SH	246.26	68.4%	COND	1.62	95.0%	ABSORBER	0.61	89.4%
RH	16.03	89.8%	CONDPUMP	0.10	86.5%	RICHPUMP	12.63	13.1%
ECO	15.33	72.5%	GSCOND	0.19	21.0%	HX	14.77	83.5%
SCR	3.48	96.5%	STCOOLER	11.03	75.2%	STRIPPER	127.88	21.9%
AIRPRE1	18.33	71.4%	FPUMPTB	46.55	90.8%	COOLER	2.92	55.5%
AIRPRE2	4.63	49.8%	***Feedwater***			COMPR1	1.49	84.6%
IDFAN	0.58	80.7%	FWHX1	1.19	68.2%	IC1	1.57	12.2%
Turbine			FWHX2	0.97	81.5%	COMPR2	1.39	83.9%
HP1	22.49	87.8%	FWHX3	0.98	86.6%	IC2	1.21	14.4%
HP2	1.14	89.9%	FWHX4	3.71	82.5%	COMPR3	1.13	84.2%
IP1	18.47	83.1%	DEAERATOR	2.18	96.6%	IC3	3.27	7.8%
IP2	8.97	89.6%	FWPUMP	1.74	90.3%	COMPR4	1.08	84.5%
LP1	1.14	94.5%	FWHX6	1.38	95.0%	IC4	5.76	2.2%

Table 5.6 Exergy destruction and efficiency of each component for Case 3

Components	$\dot{E}x_{D,n}$ (MW)	ε (%)	Components	$\dot{E}x_{D,n}$ (MW)	ε (%)	Components	$\dot{E}x_{D,n}$ (MW)	ε (%)
Boiler			LP3	2.07	91.5%	***PCC***		
FDFAN	1.10	72.0%	LP4	3.87	81.9%	DCC	13.86	39.3%
PAFAN	0.62	72.0%	LP5	2.46	90.4%	ABSORBER	0.57	93.0%
BURNER	752.86	58.0%	COND	1.58	95.0%	RICHPUMP	13.44	19.8%
SH	246.26	68.4%	CONDPUMP	0.10	86.5%	CCEX	0.42	83.3%
RH	16.03	89.8%	GSCOND	0.19	21.0%	HCEX	4.91	96.9%
ECO	15.33	72.5%	STCOOLER	6.29	75.2%	STEAMH	20.78	71.0%
SCR	3.48	96.5%	FPUMPTB	46.55	90.8%	STRIPPER	44.95	82.1%
AIRPRE1	18.33	71.4%	***Feedwater***			CREX	7.83	26.7%
AIRPRE2	4.63	49.8%	FWHX1	1.19	68.2%	COOLER	0.52	67.0%
IDFAN	0.58	80.7%	FWHX2	0.97	81.5%	COMPR1	1.27	84.2%
Turbine			FWHX3	0.98	86.6%	IC1	1.17	13.7%
HP1	22.49	87.8%	FWHX4	3.71	82.5%	COMPR2	1.20	83.4%
HP2	1.14	89.9%	DEAERATOR	2.18	96.6%	IC2	0.81	16.5%
IP1	18.47	83.1%	FWPUMP	1.74	90.3%	COMPR3	1.06	83.5%
IP2	8.97	89.6%	FWHX6	1.38	95.0%	IC3	1.18	17.7%
LP1	1.14	94.5%	FWHX7	2.58	94.2%	COMPR4	0.66	83.4%
LP2	3.89	92.7%	FWHX8	1.63	95.2%	IC4	3.15	3.3%

5.5 Conclusion

This chapter evaluates the energy and exergy performance of a BFPP integrated with PCC process using different configurations modelled in Aspen Plus®. The optimised PCC process with the AIC-AFS configuration and 32.5wt% PZ, developed in Chapter 4, was linked to a 550 MWe supercritical BFPP and compared to standard PCC processes using 30wt% MEA and 40wt% PZ. It analyses and compares the thermodynamic performance, focusing on plant efficiency, energy consumption and exergy destruction to identify key differences and inefficiencies across the integrated system. The key findings of this thermodynamic analysis are as follows:

- In the energy analysis, Case 3 demonstrated the minimum energy penalty at 22.4% and the minimum efficiency penalty at 7.8% among the three cases. It showed a reduction of 13.0% in energy penalty and 4.5% in net plant efficiency penalty when compared to the standard PCC with 40wt% PZ.
- The boiler subsystem accounts for the largest proportion of exergy destruction, which is mainly from the burner. This highlights the need to optimize burner design and improve energy efficiency to minimize the system's irreversibility.
- The standard PCC process using 30wt% MEA contributes significantly to exergy destruction, accounting for 17% of the total system, due to high energy demand in the reboiler for solvent regeneration. Replacing MEA with 40wt% PZ reduces exergy destruction by 22.3% (54.5 MW) due to its higher absorption capacity, which lowers solvent flow requirements.
- The AIC-AFS configuration with 32.5wt% PZ decreases exergy destruction in the PCC subsystem by 37.8% (71.8 MW) compared to the standard PCC process using 40wt% PZ. This reduces the PCC subsystem's contribution to 9% of the total system, significantly improving overall thermodynamic performance.

Chapter 6 Life cycle assessment of supercritical BFPP integrated with PZ-based PCC through simulation

6.1 Overview

In this chapter, the LCA of the BFPP integrated with PCC processes was carried out to assess the environmental impacts of BFPP with/without PCC processes. In Section 6.2, the goal and scope are defined, and the system boundary of this LCA is given. In addition, a life cycle inventory is developed. The impact assessment evaluates key environmental indicators, such as CO_2 sequestration by biomass, CO_2 emissions of each stage of the supply chains, the net CO_2 emissions of the system, and the fuel required. The key findings of this LCA are presented in Section 6.3.

6.2 Life cycle assessment

6.2.1 Goal and scope definition

The LCA of the three cases indicated in Chapter 5 was carried out and compared with BFPP without carbon capture. This analysis aims to evaluate the greenhouse gas removal potential of three different BFPP–PCC processes. The attributional approach was applied in this study to evaluate the cradle-to-grave lifecycle. This LCA followed ISO 14040 (Klüppel, 2005) and 14044 (ISO, 2006) guidelines, using SimaPro® v9.0 with the Ecoinvent 3.4 database to create the life cycle inventory (LCI) and perform the life cycle impact assessment (LCIA). This method can evaluate various impact categories, but this LCA focused on assessing each process's negative emissions.

The system boundary for this LCA of BFPP without carbon capture and the three integration cases are presented in

Figure 6.1 and Figure 6.2. The system boundary of BFPP consists of biomass production, harvesting, processing, transportation, biomass for power generation, the emission during the whole supply chain and fuel/electricity used for each stage. The downstream use of the generated electricity is not considered in this study. For the cases with carbon capture, the flue gas from BFPP is sent to the CCS system, including CO_2 capture using amine-based solvents, compression of the concentrated CO_2 and CO_2 geologic sequestration. Other CO_2

utilisation approaches are not discussed in this LCA.

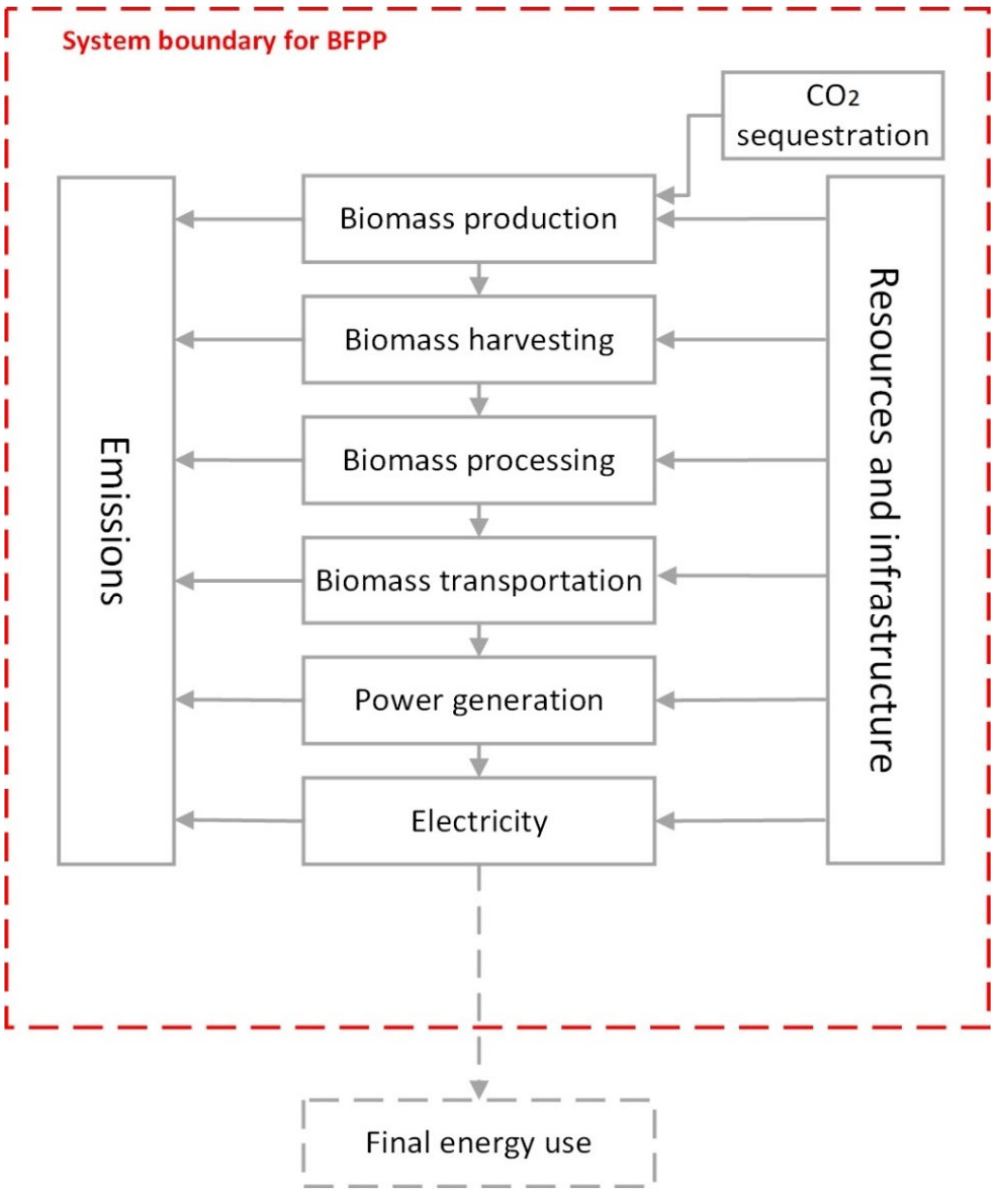

Figure 6.1 System boundary for BFPP

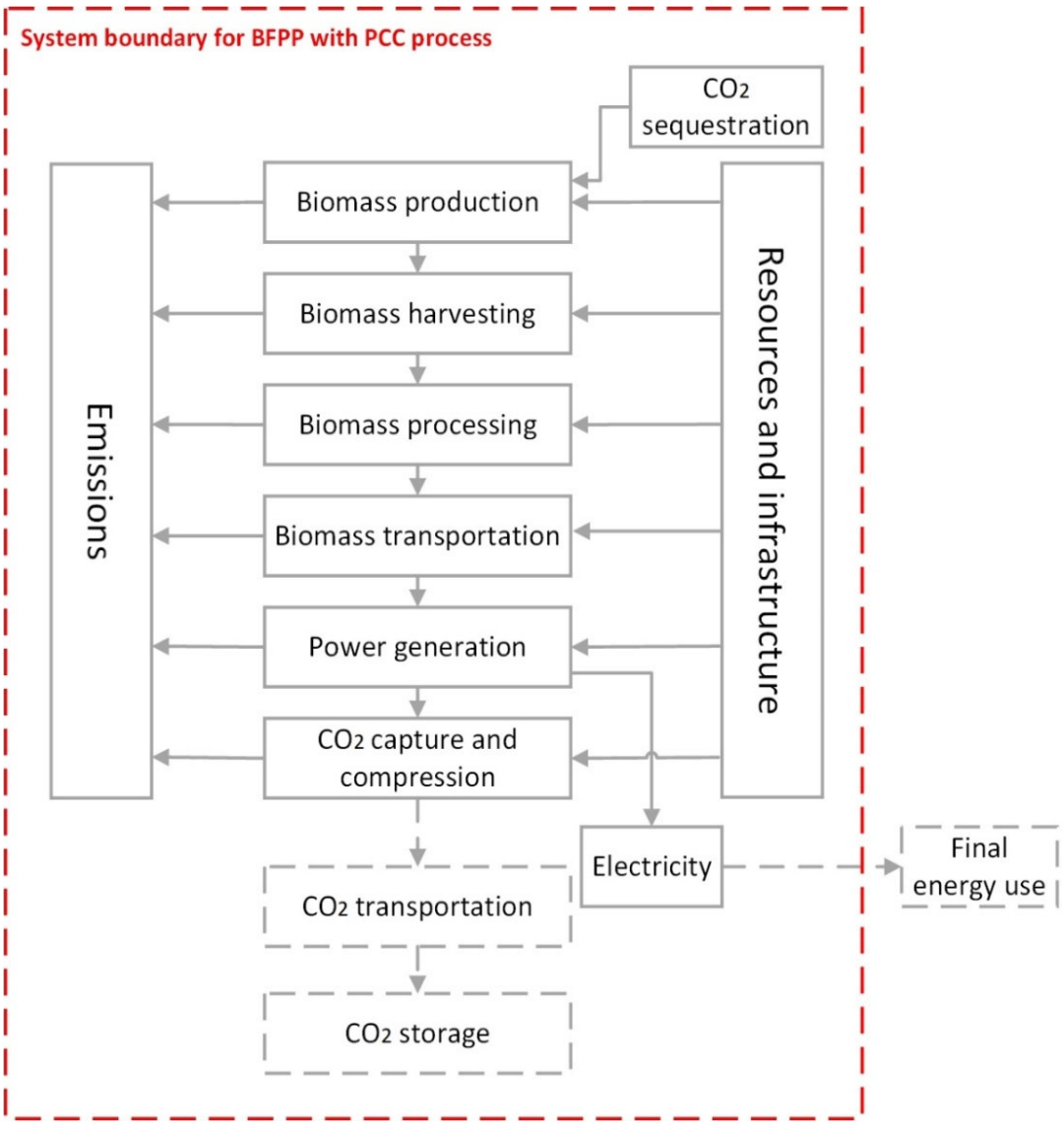

Figure 6.2 System boundary for BFPP with PCC process

6.2.2 Inventory analysis

Table 6.1 shows the LCI for BFPP with and without different CCS processes. In this study, the functional unit used is 1 MWh of net electricity produced from BFPP with/without PCC processes. Biomass cultivation uses fertilizers, herbicides, and pesticides to support healthy growth. Subsequently, the biomass is harvested using machinery powered by diesel and electricity. Afterwards, it's processed into pellets to reduce its moisture content. The biomass pellets are then delivered to the BFPP by trucks, where they're burned for electricity generation. The energy and fuel consumed in these stages are obtained from the NETL (2012) report. For cases where CCS is applied, the flue gases from the BFPP will go through CO_2 capture and compression processes. The energy and material flow in the cases with carbon

capture are obtained from simulation results presented in Chapters 4 and 5. The concentrated CO_2 is then transported through pipelines to storage in saline aquifers. In this study, it is assumed that the BECCS plant is located near the biomass source. As indicated in NETL (2012) report, biomass availability is often local or regional, and long-distance transportation can significantly affect both economic feasibility and lifecycle GHG emissions.

Table 6.1 LCI for BFPP with/without PCC processes

Inputs for the supply chains	Units	BFPP	Case 1	Case 2	Case 3
Biomass production					
N-Fertilizer[a]	g/t	781.5	781.5	781.5	781.5
P_2O_5 Fertilizer[a]	g/t	208.3	208.3	208.3	208.3
K_2O Fertilizer[a]	g/t	364.9	364.9	364.9	364.9
Herbicides[a]	g/t	26.5	26.5	26.5	26.5
Pesticides[a]	g/t	2.2	2.2	2.2	2.2
Biomass harvesting					
Harvesting, diesel[a]	kWh/t	0.67	0.67	0.67	0.67
Harvesting, electricity[a]	kWh/t	0.04	0.04	0.04	0.04
Biomass processing					
Pelleting, electricity[a]	kWh/t	145.4	145.4	145.4	145.4
Biomass transportation					
Average transport distance[a]	km	82.8	82.8	82.8	82.8
Truck fuel use, diesel[a]	km/L	2.08	2.08	2.08	2.08
Truck capacity[a]	t	21.8	21.8	21.8	21.8
CCS infrastructure					
CO_2 production[b]	t_{CO2}/t	-	0.04	0.04	0.04
CO_2 compression electricity[b]	kWh/t	-	134.3	104.0	82.0
CO_2 pumping electricity[b]	kWh/t	-	28.4	18.8	10.8
CO_2 solvent regeneration[b]	kWh/t	-	481.2	477.4	278.9
CO_2 transport to storage, pipeline[a]	km	-	80.5	80.5	80.5
CO_2 storage capacity[a]	t/d	-	9360	9360	9360
CO_2 injection electricity[c]	kWh/kg_{CO2}	-	0.03	0.03	0.03

[a] data is obtained from NETL (2012).

[b] data is obtained from Aspen Plus® simulation results.

[c] data is obtained from García-Freites et al. (2021).

6.2.3 Impact assessment

The LCA was carried out using SimaPro® based on the LCI presented in Table 6.1. The CO_2 sequestration was calculated using the carbon content and biomass feed rate provided in Section 3.2.1.1. The CO_2 emissions from each stage of the supply chains are obtained from SimaPro® using the IPCC 2013 GWP 100a method (IPCC, 2013). This method is specially used for evaluating the climate change impacts of GHGs. The Global Warming Potential (GWP) is a metric used to quantify the climate impact of various GHGs relative to CO_2 over a specific time horizon. The GWP100 method refers to the evaluation of GWP over a 100-year period. This approach converts all relevant GHG emissions into a single unit of CO_2-equivalent (kg CO_2-eq). The total GHG emissions were calculated as the sum of individual GHGs (e.g., CO_2, CH_4, N_2O) multiplied by their corresponding GWP factors, as reported in the IPCC (2013).

Table 6.2 CO_2 sequestration and emission of BFPP with/without PCC processes per unit of net power generated

	BFPP	Case 1	Case 2	Case 3
CO_2 sequestration (kg/MWh)	-1092	-1724	-1659	-1385
Total GHG emissions from biomass production and transport (kg CO_2-eq /MWh)	135	213	205	171
Total GHG emissions from energy conversion and CO_2 capture (kg CO_2-eq /MWh)	984	181	173	137
Total GHG emissions from CCS Infrastructure (kg CO_2-eq /MWh)	-	28	27	22
Total net CO_2 emissions (kg/MWh)	26	-1330	-1281	-1077

The CO_2 sequestrations and emissions of BFPP and the three integration cases proposed in Chapter 5 were evaluated based on 1 MWh of net power generated, as shown in Table 6.2. The CO_2 sequestration refers to the amount of biogenic CO_2 removed from the atmosphere

during the growth of biomass feedstock (García-Freites et al., 2021). The total CO_2 sequestration is calculated based on the carbon content and yield of the biomass feedstock, using data from NETL (2012) report. In Table 6.2, CO_2 sequestration (kg/MWh) refers to CO_2 sequestration per unit of net power generated, which is the total amount of CO_2 sequestration divided by the net electricity output.

Table 6.2 showed that BFPP is a near-zero carbon emission technology. The biomass absorbs CO_2 from the atmosphere during growth and releases CO_2 through the combustion in the power generation process. However, it is not an absolute zero-carbon process because of the CO_2 emissions during the biomass production and harvesting processes. Case 1 achieves the highest CO_2 sequestration of -1724 kg_{CO2}/MWh and the largest net-negative emissions of -1330 kg_{CO2}/MWh despite having the highest energy consumption for carbon capture among the three cases. This outcome is primarily because the MEA-based configuration has the lowest net power output, which increases the CO_2 sequestration per unit of electricity produced.

Table 6.3 CO_2 sequestration and emission of BFPP with/without PCC processes per tonne biomass feedstock

	BFPP	Case 1	Case 2	Case 3
Biomass requirement (t/MWh)	0.57	0.90	0.86	0.72
CO_2 sequestration (kg/t)	-1920	-1920	-1920	-1920
Total GHG emissions from the supply chain (kg CO_2-eq /t)	1966	470	468	458
Total net CO_2 emissions (kg/t)	47	-1481	-1483	-1493

As illustrated in Table 6.3, the biomass feedstock required to generate 1 MWh of net electricity was evaluated. In addition, the CO_2 sequestrations and net emissions of consuming 1 tonne of biomass on a dry basis were compared. The CO_2 sequestration (kg/t) is determined by dividing the total sequestered CO_2 by the biomass feedstock flow rate. As a result, Case 3 achieved the highest net negative emissions of -1493 kg_{CO2}/t with the lowest biomass requirement of 0.72 t/MWh and supply chain emissions of 458 kg_{CO2}/t in the three integration designs. It demonstrates the advantages of these optimised PCC configurations in reducing CO_2 emissions and improving the sustainability of the system.

6.3 Conclusion

This chapter conducted a cradle-to-grave LCA using SimaPro®, aiming at evaluating the environmental impacts of BFPP integrated with PCC processes in terms of the GHG removal potential. The system boundary contains the biomass production, processing, transportation, energy conversion and the CCS infrastructure. A life cycle inventory is developed, including key inputs such as fertilizers, herbicides, energy consumption for harvesting and processing, transportation, and emissions from BFPP and CCS. The impact assessment was carried out to assess the net negative emissions of the systems. The key findings of the LCA are as follows:

- The BFPP achieves near-zero carbon emissions by balancing CO_2 absorption during biomass growth with CO_2 release during combustion, though emissions from biomass production and harvesting make it not entirely carbon-neutral.
- When evaluated on a 1 MWh electricity generated basis, Case 1 achieves the highest CO_2 sequestration of -1724 kg_{CO2}/MWh and the largest net-negative emissions of -1330 kg_{CO2}/MWh. This is due to its lower net power output, which increases the CO_2 sequestration per unit of electricity produced, despite the highest energy consumption for carbon capture.
- Case 3 with the optimised PCC demonstrates the best performance per tonne of biomass, achieving the highest net-negative emissions of -1493 kg_{CO2}/t, the lowest biomass requirement of 0.72 t/MWh, and the lowest supply chain emissions of 458 kg_{CO2}/t, highlighting the advantages of this optimized PCC configuration in increasing the system sustainability.

Chapter 7 Conclusions and recommendations for future research

7.1 Conclusions

7.1.1 Model development and validation of BFPP and solvent-based PCC at large scale

In Chapter 3, the steady-state simulation of a 550 MWe supercritical BFPP and two PCC processes using MEA and PZ were carried out in Aspen Plus®. The BFPP model, divided into boiler, turbine, and feedwater subsystems, was validated against reference data from NETL (2012). The model comparison results showed small deviations in gross power output (0.06%), net plant power output (0.14%), and efficiency (2.42%), with stream data closely approaching the reference data. The PCC models for MEA and PZ were validated at a pilot scale with relative errors within the ±10% range, confirming their reliability in predicting CO_2 absorption performance. The scale-up of the PCC for the 550 MWe BFPP showed that it required two absorbers with diameters of 10.6 m (MEA-based case) and 10 m (PZ-based cases) and a single stripper with diameters of 9 m (MEA-based case) and 8 m (PZ-based cases) in the full-scale PCC plant.

7.1.2 Techno-economic analysis and optimisation of PZ-based PCC process for supercritical BFPP through simulation

The steady-state model of the PCC process using various process configurations was developed in Aspen Plus®. The sensitivity analysis was carried out to evaluate the impact of key indicators on energy performance. Energy demand and cost were the primary metrics used to assess the performance of the PCC process. The energy analysis investigated the penalties in energy consumption and efficiency caused by implementing PCC. The results showed that using 40wt% PZ reduced the reboiler duty by 0.21 GJ/t_{CO2} compared to using 30wt% MEA for standard PCC. While the AIC-AFS-SSE- sCO_2 configuration using 40wt% PZ had the least heat duty of 2.78 GJ/t_{CO2} with the lowest energy and efficiency penalties.

Additionally, the economic analysis for the nine cases was performed using APEA® to identify the most cost-effective configuration. The results showed that AIC-AFS-SSE-sCO_2 with 40wt%

PZ had the least CCC of \$57.5/t_{CO2}, a 17% reduction compared to the standard 40wt% PZ case.

Optimization determined the ideal PZ concentrations to be 37.5wt% for the standard configuration and 32.5wt% for AIC-AFS, with a stripper pressure of 7 bar for AIC-AFS achieving a heat duty of 2.09 GJ/t_{CO2} and a capture cost of \$46.6/t_{CO2}, representing reductions of 41.6% in energy use and 32.4% in cost compared to the standard 40wt% PZ case.

7.1.3 Energy and exergy analysis of supercritical BFPP integrated with solvent-based PCC through simulation

The thermodynamic performance of BFPP integrated with different PCC configurations was analysed through energy and exergy analysis. Three cases including BFPP integrated with standard PCC process using 30wt% MEA (Case 1), BFPP integrated with standard PCC using 40wt% PZ (Case 2) and BFPP with PCC process AIC-AFS configuration using 32.5wt% PZ (Case 3) were simulated in Aspen Plus®. In the energy analysis, Case 3 with optimized AIC-AFS configuration demonstrated the lowest energy penalty (22.4%) and efficiency penalty (7.8%). This corresponds to a reduction of 13.0% in energy penalty and 4.5% in efficiency penalty compared to the standard PCC process using 40wt% PZ. The boiler subsystem was identified as the largest contributor accounting for 88% of overall exergy destruction. It is mainly from the irreversibility of combustion in the burner. For the cases using standard PCC, using 40wt% PZ can reduce the exergy destruction by 22.3% compared to using 30wt% MEA. Using AIC-AFS with the optimised operating conditions showed the minimum exergy destruction, which decreased the exergy destruction in the PCC subsystem by 37.8% (71.8 MW). This demonstrated the superior thermodynamic performance of this optimised PCC process.

7.1.4 Life cycle assessment of supercritical BFPP integrated with PZ-based PCC through simulation

The LCA of BFPP integrated with different PCC processes was carried out to evaluate their net-negative CO_2 emissions and sustainability. The analysis demonstrates that BFPP is a near-zero carbon emission technology, considering the emissions from biomass production harvesting and transportation. Case 1 achieves the highest CO_2 sequestration of -1724 kg_{CO2}/MWh and the largest net-negative emissions of -1330 kg_{CO2}/MWh when evaluated based on 1 MWh net electricity generated, despite its highest energy consumption for carbon capture. This is primarily due to its lower net power output, which increases CO_2 sequestration per unit of

electricity produced. Meanwhile, Case 3, with the optimized operating conditions and AIC-AFS configuration, performs best when assessed on a per tonne biomass basis, achieving net-negative emissions of -1493 kg_{CO2}/t, the lowest biomass requirement of 0.72 t/MWh, and the lowest supply chain emissions of 458 kg_{CO2}/t. This indicates that the optimized design had a good performance in sustainability.

7.2 Recommendations for future research

7.2.1 Study on improving the efficiency of BFPP for the integration process

Compared to supercritical CFPP at around 40%, the efficiency of BFPP is lower because of the lower calorific value of biomass compared to coal. Therefore, approaches to improve the quality of the biomass feedstock can be investigated, for example, using different types of biomass feedstock or applying some effective pretreatment approaches. Additionally, when integrated with the PCC process, the steam extracted from the BFPP should be cooled down because the temperature is higher than solvent regeneration requirements. Therefore, configurations of BFPP can be improved to utilize this amount of energy (about 30 MW).

7.2.2 Study on improving the efficiency of PCC for the integration process

This study guides the comprehensive analyses of BFPP integrated with PCC. Other effective PCC approaches can also be considered such as using a rotating packed bed (RPB) absorber and stripper to intensify the mass transfer and thus reduce the size of the columns. Additionally, some novel solvents with different configurations are possible to reduce the energy consumption of the PCC subsystem. However, it is important to evaluate the PCC technology from different aspects including thermodynamic, economic and environmental performance.

7.2.3 Dynamic modelling of large-scale BFPP integrated with PCC process

In this study, the steady state modelling was carried out to evaluate the long-term techno-economic performance of BFPP integrated with PCC process. However, steady-state models cannot capture transient behaviours such as start-up, shutdown, and load changes (Lawal et al., 2012). Dynamic modelling enables the evaluation of start-up, shutdown, and load-following scenarios, and helps identify potential control

challenges arising from the interaction between the BFPP and the PCC unit. This approach supports the development of more robust and responsive control strategies, improves operational flexibility, and reduces the cost and risk associated with physical testing.

7.2.4 Comprehensive LCA on large-scale BFPP integrated with PCC process

This study focuses on the study of GHG removal performance of BFPP–PCC processes. While other environmental impact categories such as Eutrophication Potential, Acidification Potential, Land Use, and Water Use were not evaluated. Therefore, to provide a more comprehensive assessment of the environmental impact of BFPP–PCC processes, additional indicators beyond GWP should be evaluated.

Moreover, it is assumed that the BECCS plant is located near the biomass source in this study, as biomass is generally considered a local or regional resource. However, in some cases, biomass feedstock relies on imports from other countries. For example, the Drax power station in the UK sources a significant share of its biomass, particularly wood pellets, from North America, involving long-distance marine and rail transportation (EEA, 2018). This results in additional GHG emissions due to long-distance transport. Thus, it is recommended to include the discussion of long-distance transport scenarios for future research.

References

Abu-Zahra, M.R.M., Schneiders, L.H.J., Niederer, J.P.M., Feron, P.H.M. and Versteeg, G.F. (2007) 'CO_2 capture from power plants. Part I. A parametric study of the technical performance based on monoethanolamine', *International Journal of Greenhouse Gas Control*, 1, 37–46.

Adu, E., Zhang, Y.D., Liu, D. and Tontiwachwuthikul, P. (2020) 'Parametric process design and economic analysis of post-combustion CO_2 capture and compression for coal-and natural gas-fired power plants', *Energies*, 13, 1–27.

Aghel, B., Sahraie, S. and Heidaryan, E. (2020) 'Comparison of aqueous and non-aqueous alkanolamines solutions for carbon dioxide desorption in a microreactor', *Energy*, 201, 117618.

Akrami, E., Ameri, M. and Rocco, M. V. (2020) 'Developing an Innovative biomass-based Power Plant for low-carbon Power production: Exergy and Exergoeconomic analyses', *Thermal Science and Engineering Progress*, 19, 100662.

Alabdulkarem, A., Hwang, Y. and Radermacher, R. (2012) 'Development of CO_2 liquefaction cycles for CO_2 sequestration', *Applied Thermal Engineering*, 33–34, 144–156.

Alholmens (2001) *The world´s largest biofuel CHP plant: Alholmens Kraft, Pietarsaari*.

Ali, U., Font-Palma, C., Akram, M., Agbonghae, E.O., Ingham, D.B. and Pourkashanian, M. (2017) 'Comparative potential of natural gas, coal and biomass-fired power plant with post-combustion CO_2 capture and compression', *International Journal of Greenhouse Gas Control*, 63, 184–193.

Alibaba (2023a) *High quality monoethanolamine/monoethanolamine 99%*. Available at: https://www.alibaba.com/product-detail/High-Quality-Monoethanolamine-Mono-Ethanol-Amine_1600999425836.html?spm=a2700.galleryofferlist.normal_offer.d_image.e9fb13a07o3bkL (Accessed: 12 June 2023).

Alibaba (2023b) *Piperazine CAS 110-85-0*. Available at: https://www.alibaba.com/product-detail/Piperazine-CAS-110-85-

0_1601239612928.html?spm=a2700.galleryofferlist.normal_offer.d_image.217a13a0bj7HKh (Accessed: 12 June 2023).

Amrollahi, Z., Ystad, P.A.M., Ertesvåg, I.S. and Bolland, O. (2012) 'Optimized process configurations of post-combustion CO_2 capture for natural-gas-fired power plant - Power plant efficiency analysis', *International Journal of Greenhouse Gas Control*, 8, 1–11.

Artanto, Y., Jansen, J., Pearson, P., Do, T., Cottrell, A., Meuleman, E. and Feron, P. (2012) 'Performance of MEA and amine-blends in the CSIRO PCC pilot plant at Loy Yang Power in Australia', *Fuel*, 101, 264–275.

Artanto, Y., Jansen, J., Pearson, P., Puxty, G., Cottrell, A., Meuleman, E. and Feron, P. (2014) 'Pilot-scale evaluation of AMP/PZ to capture CO_2 from flue gas of an Australian brown coal-fired power station', *International Journal of Greenhouse Gas Control*, 20, 189–195.

Aspentech (2024a) *Aspen Plus Leading Process Simulation Software in the Chemical Industry*. Available at: https://www.aspentech.com/en/products/engineering/aspen-plus (Accessed: 9 July 2024).

Aspentech (2024b) *Aspen Process Economic Analyze-Maximize project profitability by comparing cash flow and operating cost of multiple design options during conceptual design.* Available at: https://www.aspentech.com/en/products/engineering/aspen-process-economic-analyzer (Accessed: 9 July 2024).

Aspentech (2010a) *Rate-Based model of the CO_2 capture process by MEA using Aspen Plus 11*.

Aspentech (2010b) *Rate-Based model of the CO_2 capture process by mixed PZ and MEA using Aspen Plus 11*.

Austgen, D.M., Rochelle, G.T., Peng, X. and Chen, C.C. (1989) 'Model of vapour-liquid equilibria for aqueous acid gas-alkanolamine systems using the electrolyte-NRTL equation', *Industrial and Engineering Chemistry Research*, 28, 1060–1073.

BFL (2013) *Hybrid Poplar*. Available at: https://bioenergylibrary.inl.gov (Accessed: 5 December 2023).

Bird, R.B., Stewart, W.E. and Lightfoot, E.N. (2001) *Transport Phenomena 2nd Ed.*John Wiley & Sons, INC,New York.

Bishnoi, S. and Rochelle, G.T. (2000) 'Absorption of carbon dioxide into aqueous piperazine: Reaction kinetics, mass transfer and solubility', *Chemical Engineering Science*, 55, 5531–5543.

Bishnoi, S. and Rochelle, G.T. (2002) 'Absorption of carbon dioxide in aqueous piperazine/methyldiethanolamine', *AIChE Journal*, 48, 2788–2799.

BLS (2023) *Average energy prices for the United States, regions, census divisions, and selected metropolitan areas: Midwest Information Office: U.S. Bureau of Labor Statistics*. Available at: https://www.bls.gov/cpi/notices/2024/publication-changes.htm (Accessed: 12 June 2023).

Borhani, N.T., Babamohammadi, S., Khallaghi, N. and Zhang, Z. (2022) 'Mixture of piperazine and potassium carbonate to absorb CO_2 in the packed column: Modelling study', *Fuel*, 308, 122033.

Bougie, F. and Iliuta, M.C. (2012) 'Sterically hindered amine-based absorbents for the removal of CO_2 from gas streams', *Journal of Chemical and Engineering Data*, 57, 635–669.

Bougie, F., Pokras, D. and Fan, X. (2019) 'Novel non-aqueous MEA solutions for CO_2 capture', *International Journal of Greenhouse Gas Control*, 86, 34–42.

Bravo, J.L., Patwardhan, A.A. and Edgar, T.F. (1992) 'Influence of effective interfacial areas in the operation and control of packed distillation columns', *Industrial and Engineering Chemistry Research*, 31, 604–608.

Bravo, J.L., Rocha, J.A. and Fair, J.R. (1985) 'Mass transfer in gauze packings', *Hydrocarbon Processing*, 64, 91–95.

Canepa, R. and Wang, M. (2015) 'Techno-economic analysis of a CO_2 capture plant integrated with a commercial scale combined cycle gas turbine (CCGT) power plant', *Applied Thermal Engineering*, 74, 10–19.

Canepa, R., Wang, M., Biliyok, C. and Satta, A. (2013) 'Thermodynamic analysis of combined

cycle gas turbine power plant with post-combustion CO_2 capture and exhaust gas recirculation', *Proceedings of the Institution of Mechanical Engineers, Part E: Journal of Process Mechanical Engineering*, 227, 89–105.

Cebrucean, D., Cebrucean, V. and Ionel, I. (2020) 'Modeling and performance analysis of subcritical and supercritical coal-fired power plants with biomass co-firing and CO_2 capture', *Clean Technologies and Environmental Policy*, 22, 153–169.

Chang, L., Wu, Z. and Ghadimi, N. (2023) 'A new biomass-based hybrid energy system integrated with a flue gas condensation process and energy storage option: An effort to mitigate environmental hazards', *Process Safety and Environmental Protection*, 177, 959–975.

Chauvy, R., Verdonck, D., Dubois, L., Thomas, D. and De Weireld, G. (2021) 'Techno-economic feasibility and sustainability of an integrated carbon capture and conversion process to synthetic natural gas', *Journal of CO_2 Utilization*, 47, 101488.

Chen, E. (2007) *Carbon Dioxide Absorption into Piperazine Promoted Potassium Carbonate using Structured Packing*. The University of Texas at Austin.

Chilton, T.H. and Colburn, A.P. (1934) 'Mass transfer (absorption) coefficients: prediction from data on heat transfer and fluid friction', *Industrial and Engineering Chemistry*, 26, 1183–1187.

Closmann, F., Nguyen, T. and Rochelle, G.T. (2009) 'MDEA/Piperazine as a solvent for CO_2 capture', *Energy Procedia*, 1, 1351–1357.

Córdoba, P. (2015) 'Status of Flue Gas Desulphurisation (FGD) systems from coal-fired power plants: Overview of the physic-chemical control processes of wet limestone FGDs', *Fuel*, 144, 274–286.

Cousins, A., Cottrell, A., Lawson, A., Huang, S. and Feron, P.H.M. (2012) 'Model verification and evaluation of the rich-split process modification at an Australian-based post-combustion CO_2 capture pilot plant', *Greenhouse Gases: Science and Technology*, 2, 9–16.

Cousins, A., Huang, S., Cottrell, A., Feron, P.H.M., Chen, E. and Rochelle, G.T. (2015) 'Pilot-

scale parametric evaluation of concentrated piperazine for CO_2 capture at an Australian coal-fired power station', *Greenhouse Gas Sci Technol.*, 5, 7–16.

Cross, S., Welfle, A.J., Thornley, P., Syri, S. and Mikaelsson, M. (2021) 'Bioenergy development in the UK & Nordic countries: A comparison of effectiveness of support policies for sustainable development of the bioenergy sector', *Biomass and Bioenergy*, 144, 105887.

Cutz, L., Berndes, G. and Johnsson, F. (2019) 'A techno-economic assessment of biomass co-firing in Czech Republic, France, Germany and Poland', *Biofuels, Bioproducts and Biorefining*, 13, 1289–1305.

Drax (2023) *Drax ends half a century of coal-fired power generation*. Available at: https://www.drax.com/press_release/drax-ends-half-a-century-of-coal-fired-power-generation/?utm_source=chatgpt.com (Accessed: 5 June 2024).

Dugas, R.E. (2009) *Carbon dioxide absorption, desorption, and diffusion in aqueous piperazine and monoethanolamine*. PhD Thesis. The University of Texas at Austin.

Dugas, R.E. (2006) *Pilot Plant Study of Carbon Dioxide Capture by Aqueous Monoethanolamine*. MSc Thesis. The University of Texas at Austin.

Emenike, O., Michailos, S., Finney, K.N., Hughes, K.J., Ingham, D. and Pourkashanian, M. (2020) 'Initial techno-economic screening of BECCS technologies in power generation for a range of biomass feedstock', *Sustainable Energy Technologies and Assessments*, 40, 100743.

Ermatchkov, V., Pérez-Salado Kamps, Á. and Maurer, G. (2003) 'Chemical equilibrium constants for the formation of carbamates in (carbon dioxide + piperazine + water) from 1H-NMR-spectroscopy', *Journal of Chemical Thermodynamics*, 35, 1277–1289.

Fajardy, M., Morris, J., Gurgel, A., Herzog, H., Mac Dowell, N. and Paltsev, S. (2021) 'The economics of bioenergy with carbon capture and storage (BECCS) deployment in a 1.5 °C or 2 °C world', *Global Environmental Change*, 68, 102262.

Freeman, S.A., Dugas, R., Van Wagener, D., Nguyen, T. and Rochelle, G.T. (2009)

‘Carbon dioxide capture with concentrated, aqueous piperazine’, *Energy Procedia*, 1, 1489–1496.

Freeman, S.A., Dugas, R., Van Wagener, D.H., Nguyen, T. and Rochelle, G.T. (2010) ‘Carbon dioxide capture with concentrated, aqueous piperazine’, *International Journal of Greenhouse Gas Control*, 4, 119–124.

Gao, T. and Rochelle, G.T. (2020) ‘CO_2 absorption from gas turbine flue gas by aqueous piperazine with intercooling’, *Industrial and Engineering Chemistry Research*, 59, 7174–7181.

Gao, T., Selinger, J.L. and Rochelle, G.T. (2019) ‘Demonstration of 99% CO_2 removal from coal flue gas by amine scrubbing’, *International Journal of Greenhouse Gas Control*, 83, 236–244.

García-Freites, S., Gough, C. and Röder, M. (2021) ‘The greenhouse gas removal potential of bioenergy with carbon capture and storage (BECCS) to support the UK’s net-zero emission target’, *Biomass and Bioenergy*, 151

Gaspar, J. and Fosbøl, P.L. (2016) ‘Simulation and multivariable optimization of post-combustion capture using piperazine’, *International Journal of Greenhouse Gas Control*, 49, 227–238.

Gautam, A. and Mondal, M.K. (2023) ‘Review of recent trends and various techniques for CO2 capture: Special emphasis on biphasic amine solvents’, *Fuel*, 334, 126616.

GCCSI (2024) *Global Status of CCS 2024: Collaborating for a Net-zero Future*.

Gray, T. (2019) *An introduction to exergy and its evaluation using Aspen Plus*. MSc Thesis. Kansas State University.

Von Harbou, I., Mangalapally, H.P. and Hasse, H. (2013) ‘Pilot plant experiments for two new amine solvents for post-combustion carbon dioxide capture’, *International Journal of Greenhouse Gas Control*, 18, 305–314.

Harris, Z. (2021) ‘Deployment of bio-CCS: a case study on bioelectricity’, *Contribution of IEA Bioenergy Task 45 to the inter-task project Deployment of bio-CCUS value chains*

Hassiba, R.J. and Linke, P. (2017) ‘On the simultaneous integration of heat and carbon

dioxide in industrial parks', *Applied Thermal Engineering*, 127, 81–94.

He, J., Chen, K. and Xu, J. (2017) 'Urban Air Pollution and Control', in *Encyclopedia of Sustainable Technologies*. , 243–257.

Hetzer, H.B., Bates, R.G. and Robinson, R.A. (1963) 'Dissociation constant of pyrrolidinium ion and related thermodynamic quantities from 0 to 50°', *Journal of Physical Chemistry*, 67, 1124–1127.

Hikita, H., Asai, S., Ishikawa, H. and Honda, M. (1977) 'The kinetics of reactions of carbon dioxide with monoethanolamine, and triethanolamine by a rapid mixing method diethanolamine', *Chemical Engineering Journal*, 13, 7–12.

Horvath, A.L. (1974) 'Redlich-Kwong equation of state: review for chemical engineering calculations', *Chemical Engineering Science*, 29, 1334–1340.

Horvath, A.L. (1985) *Handbook of aqueous electrolyte solutions: Physical properties, estimation and correlation methods.*Ellis HorwoodChichester.

Hosseini-Ardali, S.M., Hazrati-Kalbibaki, M., Fattahi, M. and Lezsovits, F. (2020) 'Multi-objective optimization of post-combustion CO_2 capture using methyldiethanolamine (MDEA) and piperazine (PZ) bi-solvent', *Energy*, 211, 119035.

IEA (2024a) *Coal demand in emerging markets and developing economies was the biggest driver in global emissions growth*. Available at: https://www.iea.org/reports/co2-emissions-in-2023/coal-demand-in-emerging-market-and-developing-economies-was-the-biggest-driver-in-global-emissions-growth (Accessed: 5 September 2024).

IEA (2024b) *Renewables 2024- Global overview*. Available at: https://www.iea.org/reports/renewables-2024/global-overview (Accessed: 6 September 2024).

IEA (2024c) *Carbon Capture, Utilisation and Storage*. Available at: https://www.iea.org/energy-system/carbon-capture-utilisation-and-storage (Accessed: 6 September 2024).

IEAGHG (2014) *Biomass and CCS - Guidance for accounting for negative emissions*.

Intratec (2023a) *Cooling Water Costs | Historical & Forecast | Intratec.us*. Available at: https://www.intratec.us/products/water-utility-costs/commodity/cooling-water-cost (Accessed: 12 June 2023).

Intratec (2023b) *Cost of Process Water | United States*. Available at: https://www.intratec.us/solutions/industry-economics-worldwide/utility/process-water-cost-united-states (Accessed: 23 June 2023).

IPCC (2013) *CLIMATE CHANGE 2013:The Physical Science Basis*.

ISO (2006) *Environmental management-Life cycle assessment–Requirements and guidelines*.

Jana, K. and De, S. (2015) 'Sustainable polygeneration design and assessment through combined thermodynamic, economic and environmental analysis', *Energy*, 91, 540–555.

JRCEC (2012) *Life cycle indicators for resources, products and waste*.

Kemper, J. (2015) 'Biomass and carbon dioxide capture and storage: A review', *International Journal of Greenhouse Gas Control*, 40, 401–430.

Kenig, E.Y., Schneider, R. and Górak, A. (2001) 'Reactive absorption: Optimal process design via optimal modelling', *Chemical Engineering Science*, 56, 343–350.

Kister, H.Z., Mathias, P.M., Steinmeyer, D.E., Penney, W.R., Monical, V.S. and Fair., J.R. (2019) *Perry's Chemical Engineers' Handbook. 9th ed.*McGraw-Hill EducationNew York.

Klüppel, H.-J. (2005) 'The Revision of ISO Standards 14040-3 - ISO 14040: Environmental management – Life cycle assessment – Principles and framework - ISO 14044: Environmental management – Life cycle assessment – Requirements and guidelines', *Int J Life Cycle Assessment*, 10, 165.

Lak Kamari, M., Maleki, A., Daneshpour, R., Rosen, M.A., Pourfayaz, F. and Alhuyi Nazari, M. (2023) 'Exergy, energy and environmental evaluation of a biomass-assisted

integrated plant for multigeneration fed by various biomass sources', *Energy*, 263, 125649.

Lam, M.K., Loy, A.C.M., Yusup, S. and Lee, K.T. (2019) *Biohydrogen.*Elsevier.2nd Ed.

Lawal, A., Wang, M., Stephenson, P. and Obi, O. (2012) 'Demonstrating full-scale post-combustion CO_2 capture for coal-fired power plants through dynamic modelling and simulation', *Fuel*, 101, 115–128.

Lawal, A., Wang, M., Stephenson, P. and Yeung, H. (2009) 'Dynamic modelling of CO2 absorption for post combustion capture in coal-fired power plants', *Fuel*, 88, 2455–2462.

Lempp, P. (2013) *Biomass co-firing in coal power plants*.

Li, H. and Yan, J. (2009) 'Evaluating cubic equations of state for calculation of vapor – liquid equilibrium of CO_2 and CO_2 -mixtures for CO_2 capture and storage processes', *Applied Energy*, 86, 826–836.

Li, J., Zhang, X., Pawlak-Kruczek, H., Yang, W., Kruczek, P. and Blasiak, W. (2014) 'Process simulation of co-firing torrefied biomass in a 220 MWe coal-fired power plant', *Energy Conversion and Management*, 84, 503–511.

Li, K., Leigh, W., Feron, P., Yu, H. and Tade, M. (2016) 'Systematic study of aqueous monoethanolamine (MEA)-based CO_2 capture process: Techno-economic assessment of the MEA process and its improvements', *Applied Energy*, 165, 648–659.

Lin, Y.J. (2016) *Modeling advanced flash stripper for carbon dioxide capture using aqueous amines. PhD Thesis*. University of Texas at Austin.

Lin, Y.J. and Rochelle, G.T. (2014) 'Optimization of an advanced flash stripper for CO_2 capture using piperazine', *Energy Procedia*, 63, 1504–1513.

Linnenberg, S., Liebenthal, U., Oexmann, J. and Kather, A. (2011) 'Derivation of power loss factors to evaluate the impact of post-combustion CO_2 capture processes on steam power plant performance', *Energy Procedia*, 4, 1385–1394.

Liu, X., Chen, J., Luo, X., Wang, M. and Meng, H. (2015) 'Study on heat integration of

supercritical coal-fired power plant with post-combustion CO_2 capture process through process simulation', *Fuel*, 158, 625–633.

Livingston, W., Middlekamp, J., Willeboer, W., Tosney, S., Sander, B., Hansen, M. and Madrali, S. (2016) *The status of large scale biomass firing*.

Loachamin, D., Casierra, J., Calva, V., Palma-Cando, A., Ávila, E.E. and Ricaurte, M. (2024) 'Amine-Based Solvents and Additives to Improve the CO_2 Capture Processes: A Review', *ChemEngineering*, 8

Luo, X. (2016) *Process modelling, simulation and optimisation of natural gas combined cycle power plant integrated with carbon capture, compression and transport. PhD Thesis*University of HullUK.

Luo, X. and Wang, M. (2016) 'Optimal operation of MEA-based post-combustion carbon capture for natural gas combined cycle power plants under different market conditions', *International Journal of Greenhouse Gas Control*, 48, 312–320.

Ma, J., Dong, Z., Otitoju, O., Wang, M., Du, W. and Qian, F. (2024) 'Heat integration, process design and techno-economic assessment of post-combustion carbon capture using piperazine for large-scale ethylene plant', *Chemical Engineering Science*, 284, 119531.

Mangalapally, H.P. and Hasse, H. (2011a) 'Pilot plant study of post-combustion carbon dioxide capture by reactive absorption: Methodology, comparison of different structured packings, and comprehensive results for monoethanolamine', *Chemical Engineering Research and Design*, 89, 1216–1228.

Mangalapally, H.P. and Hasse, H. (2011b) 'Pilot plant study of two new solvents for post-combustion carbon dioxide capture by reactive absorption and comparison to monoethanolamine', *Chemical Engineering Science*, 66, 5512–5522.

Mangalapally, H.P., Notz, R., Asprion, N., Sieder, G., Garcia, H. and Hasse, H. (2012) 'Pilot plant study of four new solvents for post-combustion carbon dioxide capture by reactive absorption and comparison to MEA', *International Journal of Greenhouse Gas Control*, 8, 205–216.

MHI (2024) *Pulverized Biomass Fired Boiler Technology*. Available at: https://power.mhi.com/products/boilers/technology/pulverized-biomass-fired (Accessed: 11 September 2024).

Le Moullec, Y. and Kanniche, M. (2011) 'Optimization of MEA based post-combustion CO_2 capture process: Flowsheeting and energetic integration', *Energy Procedia*, 4, 1303–1309.

Le Moullec, Y., Neveux, T., Al Azki, A., Chikukwa, A. and Hoff, K.A. (2014) 'Process modifications for solvent-based post-combustion CO_2 capture', *International Journal of Greenhouse Gas Control*, 31, 96–112.

Muhammad, H.A., Sultan, H., Lee, B., Imran, M., Baek, I.H., Baik, Y.J. and Nam, S.C. (2020) 'Energy minimization of carbon capture and storage by means of a novel process configuration', *Energy Conversion and Management*, 215, 112871.

Nawaz, Z. and Ali, U. (2020) 'Techno-economic evaluation of different operating scenarios for indigenous and imported coal blends and biomass co-firing on supercritical coal-fired power plant performance', *Energy*, 212, 118721.

NETL (2012) *Greenhouse Gas Reductions in the Power Industry Using Domestic Coal and Biomass Volume 2: Pulverized Coal Plants*.

NETL (2015) *Cost and Performance Baseline for Fossil Energy Plants Volume 1a: Bituminous Coal (PC) and Natural Gas to Electricity Revision 3*.

NETL (2010) *Cost and Performance Baseline for Fossil Energy Plants Volume 1: Bituminous Coal and Natural Gas to Electricity*.

Nielsen, P.T., Li, L. and Rochelle, G.T. (2013) 'Piperazine degradation in pilot plants', *Energy Procedia*, 37, 1912–1923.

Notz, R., Mangalapally, H.P. and Hasse, H. (2012) 'Post-combustion CO_2 capture by reactive absorption: Pilot plant description and results of systematic studies with MEA', *International Journal of Greenhouse Gas Control*, 6, 84–112.

Olaleye, A.K. (2015) *Modelling and Operational Analysis of Coal-Fired Supercritical Power Plant Integrated With Post-Combustion Carbon Capture Based on Chemical*

Absorption Under Uk Grid Requirement. PhD Thesis. University of Hull.

Olaleye, A.K. and Wang, M. (2017) 'Conventional and advanced exergy analysis of post-combustion CO_2 capture based on chemical absorption integrated with supercritical coal-fired power plant', *International Journal of Greenhouse Gas Control*, 64, 246–256.

Olaleye, A.K., Wang, M. and Kelsall, G. (2015) 'Steady-state simulation and exergy analysis of supercritical coal-fired power plant with CO2 capture', *Fuel*, 151, 57–72.

Orsted (2024) *Ørsted Avedøre Power Station-Green Power and Heat*. Available at: https://orsted.com/-/media/www/docs/corp/com/our-business/bioenergy-and-thermal-power/plants-brochures/avedrevrket_brochure_eng_web.ashx (Accessed: 26 September 2024).

Otitoju, O., Oko, E. and Wang, M. (2021) 'Technical and economic performance assessment of post-combustion carbon capture using piperazine for large scale natural gas combined cycle power plants through process simulation', *Applied Energy*, 292, 116893.

Parvez, M. and Khan, O. (2020) 'Parametric simulation of biomass integrated gasification combined cycle (BIGCC) power plant using three different biomass materials', *Biomass Conversion and Biorefinery*, 10, 803–812.

Pérez-Calvo, J.F. and Mazzotti, M. (2022) 'Techno-economic assessment of post-combustion CO_2 capture using aqueous piperazine at different flue gas compositions and flowrates via a general optimization methodology', *International Journal of Greenhouse Gas Control*, 114, 103587.

Peu, S.D., Das, A., Hossain, M.S., Akanda, M.A.M., Akanda, M.M.H., Rahman, M., Miah, M.N., Das, B.K., Islam, A.R.M.T. and Salah, M.M. (2023) 'A Comprehensive Review on Recent Advancements in Absorption-Based Post Combustion Carbon Capture Technologies to Obtain a Sustainable Energy Sector with Clean Environment', *Sustainability (Switzerland)*, 15

Pinsent, B.R.W., Pearson, L. and Roughton, F.J.W. (1956) 'The kinetics of combination of carbon dioxide with hydroxide ions', *Trans. Faraday Soc.*, , 1512–1520.

Plaza, J.M. (2011) *Modeling of carbon dioxide absorption using aqueous monoethanolamine, piperazine and promoted potassium carbonate.* PhD Thesis.The University of Texas at Austin.

Plaza, J.M. and Rochelle, G.T. (2011) 'Modeling pilot plant results for CO_2 capture by aqueous piperazine', *Energy Procedia*, 4, 1593–1600.

Poling, B.E., Prausnitz, J.M. and O'Connell, J.P. (2001) *The properties of gases and liquids 5th Ed.*McGraw-Hill.

Posey, M.L. and Rochelle, G.T. (1997) 'A thermodynamic model of methyldiethanolamine-CO_2-H_2S-water', *Industrial and Engineering Chemistry Research*, 36, 3944–3953.

PowerTech (2014) *Polaniec Biomass Power Plant*. Available at: https://www.power-technology.com/projects/polaniec-biomass-power-plant-poland/ (Accessed: 17 September 2024).

Rabensteiner, M., Kinger, G., Koller, M., Gronald, G. and Hochenauer, C. (2015a) 'Investigation of carbon dioxide capture with aqueous piperazine on a post-combustion pilot plant-Part I: Energetic review of the process', *International Journal of Greenhouse Gas Control*, 39, 79–90.

Rabensteiner, M., Kinger, G., Koller, M., Gronald, G. and Hochenauer, C. (2014a) 'Pilot plant study of ethylenediamine as a solvent for post-combustion carbon dioxide capture and comparison to monoethanolamine', *International Journal of Greenhouse Gas Control*, 27, 1–14.

Rabensteiner, M., Kinger, G., Koller, M., Gronald, G. and Hochenauer, C. (2015b) 'Investigation of carbon dioxide capture with aqueous piperazine on a post-combustion pilot plant-Part II: Parameter study and emission measurement', *International Journal of Greenhouse Gas Control*, 37, 471–480.

Rabensteiner, M., Kinger, G., Koller, M. and Hochenauer, C. (2014b) 'Three years of working experience with different solvents at a realistic post-combustion capture pilot plant', *Energy Procedia*, 63, 1578–1584.

Rabensteiner, M., Kinger, G., Koller, M. and Hochenauer, C. (2016) 'Pilot plant study of aqueous solution of piperazine activated 2-amino-2-methyl-1-propanol for post-combustion carbon dioxide capture', *International Journal of Greenhouse Gas Control*, 51, 106–117.

Rackett, H.G. (1970) 'Equation of state for saturated liquids', *Journal of Chemical and Engineering Data*, 15, 514–517.

Raynal, L., Bouillon, P.A., Gomez, A. and Broutin, P. (2011) 'From MEA to demixing solvents and future steps, a roadmap for lowering the cost of post-combustion carbon capture', *Chemical Engineering Journal*, 171, 742–752.

Rochelle, G.T., Chen, E., Akinpelumi, K., Fischer, K.B., Gao, T., Liu, C.-T., Selinger, J.L. and Wu, Y. (2018) 'Pilot plant demonstration of piperazine with the advanced flash stripper', *14th International Conference on Greenhouse Gas Control Technologies, GHGT-14*, 84, 72–81.

Rochelle, G.T., Wu, Y., Chen, E., Akinpelumi, K., Fischer, K.B., Gao, T., Liu, C.T. and Selinger, J.L. (2019) 'Pilot plant demonstration of piperazine with the advanced flash stripper', *International Journal of Greenhouse Gas Control*, 84, 72–81.

Roni, M.S., Chowdhury, S., Mamun, S., Marufuzzaman, M., Lein, W. and Johnson, S. (2017) 'Biomass co-firing technology with policies, challenges, and opportunities: A global review', *Renewable and Sustainable Energy Reviews*, 78, 1089–1101.

SCCS (2024) *Global CCS Map*. Available at: https://www.sccs.org.uk/resources/global-ccs-map (Accessed: 10 October 2024).

Schakel, W., Meerman, H., Talaei, A., Ramírez, A. and Faaij, A. (2014) 'Comparative life cycle assessment of biomass co-firing plants with carbon capture and storage', *Applied Energy*, 131, 441–467.

SimaPro (2024) *Life cycle assessment with SimaPro Craft*. Available at: https://simapro.com/life-cycle-assessment/ (Accessed: 5 June 2024).

Sinnott, R.K. (2005) *Chemical engineering design. 4th Ed.*Elsevier Butterworth-

HeinemannOxford.

Smith, P., Davis, S.J., Creutzig, F., Fuss, S., Minx, J., Gabrielle, B., Kato, E., Jackson, R.B., Cowie, A., Kriegler, E., Van Vuuren, D.P., Rogelj, J., Ciais, P., Milne, J., Canadell, J.G., McCollum, D., Peters, G., Andrew, R., Krey, V., Shrestha, G., Friedlingstein, P., Gasser, T., Grübler, A., Heidug, W.K., Jonas, M., Jones, C.D., Kraxner, F., Littleton, E., Lowe, J., Moreira, J.R., Nakicenovic, N., Obersteiner, M., Patwardhan, A., Rogner, M., Rubin, E., Sharifi, A., Torvanger, A., Yamagata, Y., Edmonds, J. and Yongsung, C. (2016) 'Biophysical and economic limits to negative CO_2 emissions', *Nature Climate Change*, 6, 42–50.

Soave, G. (1972) 'Equilibrium constants from a modified Redlich-Kwong equation of state', *Chemical Engineering Science*, 27, 1197–1203.

SOG (2024) *Denmark's Largest Power Station Replaces Coal with Wood Pellets*., *State of Green* Available at: https://stateofgreen.com/en/news/denmarks-largest-power-station-replaces-coal-with-wood-pellets/ (Accessed: 26 September 2024).

Stringle, R.F. (1987) *Packed Tower Design and Apllication*Gulf Publishing.2nd ed.

Szargut, J., Morris, D. and Steward, F. (1987) *Exergy analysis of thermal, chemical, and metallurgical processes*.

Terlouw, T., Bauer, C., Rosa, L. and Mazzotti, M. (2021) 'Life cycle assessment of carbon dioxide removal technologies: A critical review', *Energy and Environmental Science*, 14, 1701–1721.

UNFCCC (2015) *The Paris Agreement*. Available at: https://unfccc.int/process-and-meetings/the-paris-agreement (Accessed: 5 September 2024).

Vaidya, P.D. and Kenig, E.Y. (2007) 'CO2-alkanolamine reaction kinetics: A review of recent studies', *Chemical Engineering and Technology*, 30, 1467–1474.

Van Wagener, D.H. (2011) *Stripper Modeling for CO_2 Removal Using Monoethanolamine and Piperazine Solvents. PhD Thesis*University of Texas at AustinUSA.

Wang, M., Lawal, A., Stephenson, P., Sidders, J. and Ramshaw, C. (2011) 'Post-combustion CO_2 capture with chemical absorption: A state-of-the-art review', *Chemical Engineering*

Research and Design, 89, 1609–1624.

Wang, R., Jiang, L., Li, Q., Gao, G., Zhang, S. and Wang, L. (2020) 'Energy-saving CO_2 capture using sulfolane-regulated biphasic solvent', *Energy*, 211, 118667.

Wilke, C.R. and Chang, P. (1955) 'Correlation of diffusion coefficients in dilute solutions', *AIChE Journal*, 1, 264–270.

Wu, X., Wang, M., Liao, P., Shen, J. and Li, Y. (2020) 'Solvent-based post-combustion CO_2 capture for power plants: A critical review and perspective on dynamic modelling, system identification, process control and flexible operation', *Applied Energy*, 257, 113941.

Yan, L., Wang, L., Wang, Z., Cao, Y. and He, B. (2021) 'Comparison of three biomass-based carbon-negative power generation systems', *Journal of Cleaner Production*, 285, 125424.

Yang, Z., Shen, Y., Yang, H., Yi, H., Guo, H. and Zhang, X. (2023) 'A review of CO_2 catalytic regeneration research based on MEA solution', *Frontiers in Energy Research*, 11, 1–16.

Yin, C. (2013) 'Biomass co-firing', *Biomass Combustion Science, Technology and Engineering*, 5, 84–105.

YorkPress (2014) *Drax Power Station running on two converted biomass units*. Available at: https://www.yorkpress.co.uk/business/news/11583728.drax-power-station-running-on-two-converted-biomass-units/ (Accessed: 17 September 2024).

Zang, G., Tejasvi, S., Ratner, A. and Lora, E.S. (2018) 'A comparative study of biomass integrated gasification combined cycle power systems: Performance analysis', *Bioresource Technology*, 255, 246–256.

Zhang, S., Shen, Y., Zheng, C., Xu, Q., Sun, Y., Huang, M., Li, L., Yang, X., Zhou, H., Ma, H., Li, Z., Zhang, Y., Liu, W. and Gao, X. (2024) 'Recent advances, challenges, and perspectives on carbon capture', *Frontiers of Environmental Science and Engineering*, 18, 1–30.

Zhang, W., Chen, J., Luo, X. and Wang, M. (2017) 'Modelling and process analysis of post-combustion carbon capture with the blend of 2-amino-2-methyl-1-propanol and

piperazine', *International Journal of Greenhouse Gas Control*, 63, 37–46.

Ziebik, A., Szegda, D., Qvale, B. and Elmegaard, B. (2010) 'Thermodynamic simulation analysis of a multifuel CHP plant basing on the technological diagram of Avedøre unit 2', *archives of thermodynamics*, 31, 79–93.